iDEG:Integrated Data and Energy Gathering for Wireless Systems

By

Neha Jain

Under supervision of **Dr. Vivek Ashok Bohara** and **Prof. Anubha Gupta**

Department of Electronics and Communication Engineering

Indraprastha Institute of Information Technology Delhi

New Delhi– 110020

January, 2021

iDEG:Integrated Data and Energy Gathering for Wireless Systems

By

Neha Jain

A Thesis

submitted in partial fulfillment of the requirements for the degree of

Doctor of Philosophy

Department of Electronics and Communication Engineering

Indraprastha Institute of Information Technology Delhi

New Delhi– 110020

January, 2021

Certificate

This is to certify that the thesis titled "***iDEG:Integrated Data and Energy Gathering for Wireless Systems***" being submitted by ***Neha Jain*** to the Indraprastha Institute of Information Technology Delhi, for the award of the degree of Doctor of Philosophy, is an original research work carried out by her under my supervision. In my opinion, the thesis has reached the standard fulfilling the requirements of the regulations relating to the degree.

The results contained in this thesis have not been submitted in part or full to any other university or institute for the award of any degree or diploma.

January, 2021

Dr. Vivek Ashok Bohara

Prof. Anubha Gupta

Deptt. of Electronics and Communication Engineering,

Indraprastha Institute of Information Technology Delhi-110020, India.

Declaration

This is certified that the thesis entitled "***iDEG:Integrated Data and Energy Gathering for Wireless Systems***" being submitted by me to the Indraprastha Institute of Information Technology Delhi, for the award of degree of **Doctor of Philosophy**, is a bonafide work carried out by me. This research work has been carried out under the supervision of **Dr. Vivek Ashok Bohara** and **Prof. Anubha Gupta**. The study pertaining to this thesis has not been submitted in part or in full, to any other University or Institution for the award of any other degree.

January, 2021

Neha Jain

PhD Student,

Deptt. of Electronics and Communication Engineering,

Indraprastha Institute of Information Technology Delhi-110020, India.

Abstract

Keywords-**Wireless sensor network, Compressive sensing, Energy harvesting, Data reconstruction, Missing data recovery, Channel state information, Millimeter wave communication, Sampling process, Analog-to-digital converters, Wide sense stationary process, Correlated Signals**

The next generation wireless communication system has the goal of reducing the power consumption, increasing the network capacity and global connectivity. Most of the signals generated, transmitted or received in wireless systems are generally analog in nature. An analog signal contains both information and energy. However, using the information carrying signal for energy harvesting may lead to loss of information and hence, may affect a system's performance. Therefore, the objective of this thesis, "iDEG:integrated data and energy gathering for wireless systems" is to harvest the energy as well as information from the same signal without effecting the system performance for energy constrained applications. This implies, the designed system should recover the entire information from the partial signal, and hence the remaining signal can be used for the energy harvesting. In order to recover entire signal from partial information, we have examined different properties of the signal such as sparsity, low-rank and correlation in the data and for different applications such as wireless sensor network (WSN), millimeter wave (mmWave) communication and for wide sense stationary (WSS) signals.

To accomplish the objective of efficient data gathering, We have first proposed a partial canonical identity (PCI) based compressive sensing (CS) framework, which randomly samples the observed signal at sub-Nyquist rate and improves the data recovery performance, under the sparsity condition in particular domains such as discrete cosine transform (DCT) and discrete Fourier transform (DFT). This PCI-CS framework reduces the computation cost, implementation complexity, energy losses and can also recover the missing data values. The performance of PCI-CS has been improved in noisy environment by proposing a

robust two-stage algorithm, named as *PCI-MF*, which also utilizes the low-rank nature of the observed signal. The first stage of this algorithm utilizes PCI-CS to recover the sparsest solution and the rank of the data from the partial available information, which are jointly utilized in the second stage to de-noise the data in a matrix factorization framework. This algorithm has been compared with various conventional and state-of-the-art CS and matrix completion framework in context of WSN and mmWave communication. This is due to the fact that a) WSN data is highly coherent in spatial and temporal domain, which results in double sparsity in the DCT domain and also reduction in rank of the data. Simulations are performed on two real datasets of Intel Lab and Data Sensing Lab. b) PCI-MF has also been proposed to estimate entire channel state information (CSI) from a few randomly varying noisy channel coefficients in mmWave massive multiple-input-multiple-output (MIMO) channel, where estimation of all channel coefficients is not practically feasible. The mmWave channel matrix is a low-rank matrix, which can be modeled as a two dimensional DFT form of a sparse matrix due to the directional beamforming. Simulations have been performed on two different datasets, where one dataset is generated in a real-world setting in the New York City.

The next step of this thesis, also aligned with the title, is to develop an integrated data and energy gathering (iDEG) solution. The iDEG has been proposed for WSN, Analog-to-digital-converters (ADCs) and for correlated wide-sense-stationary signals. We have proposed an iDEG framework for practical WSN. The sensor nodes deployed in WSNs generate an analog signal corresponding to the sensed parameters, which is sampled and digitized for further processing and transmission to the fusion center. The iDEG for WSN utilizes PCI based CS framework, which selects only a set of sensor nodes at every time point to transmit the data to the FC for recovering the entire data, while the rest of the nodes, which are not participating in data transmission are utilized to harvest the energy from the received analog signal. The performance of iDEG has been tested on a real WSN dataset from Intel Lab. Comparative results of iDEG with the conventional approaches highlight its efficacy. This work motivates us to rethink the sampling process of the ADC. A common ADC architecture is based on sample-and hold (S/H) circuits, where the analog signal is being tracked only for a fraction of the sampling period, and hence allow us to harvest energy in the remaining duration, developing an iDEG solution for ADCs. Therefore, we have proposed *e*Sampling ADCs, which extends the structure of S/H ADCs without altering its data conversion procedure, while harvesting energy from

the analog signal during the time periods where the signal is not being tracked. The amount of energy harvested can be increased by reducing the sampling rate, and hence we have also analyzed the tradeoff between the accuracy and the harvested energy. Our theoretical results also shows that *e*Sampling 8-bit ADC acquiring bandlimited signal at Nyquist rate can harvest over 15 dB more energy than it consumes in the conversion procedure. To verify the feasibility of *e*Sampling ADCs, we present a circuit-level design using standard complementary metal oxide semiconductor (CMOS) 65 nm technology. An *e*Sampling 8-bit ADC which samples at 40 MHZ is designed on a Cadence Virtuoso platform. Our experimental study involving Nyquist rate sampling of bandlimited signals demonstrates that such ADCs are indeed capable of harvesting more energy than that spent during analog to- digital conversion, without effecting the accuracy. Finally, to validate *e*Sampling in real-world scenario, a hardware setup has also been designed to harvest energy along with sampling at sensor node deployed for environment and health monitoring WSN application.

The final objective for this thesis is to propose a joint sub-Nyquist *e*Sampling and reconstruction based iDEG framework for multiple correlated stochastic signals by exploiting the general correlation without inheriting an inbuilt structure. This work exploits the correlation of multiple stochastic signals to improve the reconstruction accuracy at lower sampling rate, and hence increases the amount of harvested energy from the analog signals by exploiting *e*Sampling method. We derive the achievable reconstruction error, maximum amount of energy harvested and the corresponding *e*sampling system for arbitrary sampling rates and spectral structures by designing an optimal analog combining and reconstruction filter. The proposed system minimizes the error and maximizes the energy, when sampling below the Nyquist rate by preserving only the most dominant spatial eigenmodes aliased to each frequency. Our numerical results illustrate that joint *e*sampling can achieve negligible reconstruction error at low sampling rates, and also allows the system to operate at zero power with up to 16-bits of quantization resolution.

Acknowledgements

I would like to take this opportunity to express my sincere gratitude and appreciation to a number of incredible people in my life. I could not have been what I am today, without their tremendous guidance, mentoring, help, care, and love,

First and foremost, I would like to thank my advisors, **Dr. Vivek Ashok Bohara** and **Prof. Anubha Gupta** for their consistent support, guidance, motivation, and encouragement over these years. They helped me a lot in nurturing my research capabilities and technical writing skills. Dr. Vivek is one of the helpful, kind, attentive and punctual person, I ever met in my life. Prof. Gupta's achievements, enthusiasm, and work ethics have been a great source of inspiration throughout my PhD journey. I would also like to thank them for boosting my confidence in achieving new heights. I would also like to thank **Prof. Yonina Eldar** from Weizmann Institute of Science, Israel for selecting me as an intern and guiding me in my PhD projects. She is one of the most humble, helpful, enthusiastic, passionate and organized person, I ever came across in my life till date.

I would also like to thank my supervisory committee members: **Dr. Sanjit Kaul**, and **Dr. Sumit Darak** for their valuable advice, support and constructive feedback through these years. I always benefited from their knowledge and wisdom. My gratitude also extends to the Admin Staff of IIIT-D, especially **Priti Patel** for being extremely helpful in the fast resolution of all admin related matters. I would like to take this opportunity to thank **Dr. Pydi Ganga Bahubalindruni** and her student **Bhawana Tiwari**, for helping me in demonstrating the hardware simulation of my work that has made an invaluable contribution towards my PhD.

I would also like to give a special thanks to **Nir Schelzinger**, for working meticulously with me during my internship period at the Weizmann Institute of Science, Israel. The brainstorming sessions with him have been very beneficial

and insightful. The work done with him have a notable contribution to my thesis. I would also like to thank my other mates of SAMPL lab for making my internship period memorable.

I have had the pleasure to work with my Wirocomm and SBILab mates. Sharing lab with them have been full of fun and excitement. They have not only been my collaborators but have helped me broaden my horizons. I must also express gratitude to all of my friends for making my journey memorable. I have never felt time passing by when I am talking with them. I owe a special thanks to my best friends **Vandana Mittal** and **Rekha Tokas**. I called them in every difficult situation, and their excellent tips and tricks always helped me to tackle difficult situations. They are always available for me in every up and down of my life. No words can describe our friendship.

I would like to express my gratitude to my parents, who have always been a source of encouragement throughout my academic career. I can not thank them enough for their tremendous support, unconditional love, sacrifices and inspiration along the way, that made me the person who I am today. I would like to take this opportunity to thank my brother, **Mohit** for his continuous encouragement and making me feel relaxed in every critical situation. The love and pampering of my family is life's greatest blessing given to me by God. Now, I would like to thank my soulmate, my dearest husband and my best friend, **Rishabh**. Because of his understanding, love, care and support, I could easily face every challenge of my life. I always find him beside me in every toughest or happy moment of my life. No words could ever express my appreciation for him. I thank God for enlightening my life with his presence. He is the best thing that has ever happened to me. I owe a special thanks to my father-in-law and my mother-in-law for their continuous support and blessings.

Finally, I would like to thank the Indraprastha Institute of Information Technology, Delhi (IIIT-D) for providing excellent infrastructure and research environment. Also, I am grateful to Visvesvaraya PhD scheme, Department of Electronics and Information Tech., Ministry of Comm. and IT, Govt. of India for providing me with the financial support for this work and also extremely thankful to Department of Science and Technology (DST), India to support my travel to one of the prestigious conference in signal processing, i.e., ICASSP, 2019. I would also like to sincerely thank the editors and anonymous reviewers for their constructive comments, which improve the quality of our paper to the next level.

Contents

List of Figures

List of Tables

List of Abbreviations

iDEG Integrated data and energy gathering

CS Compressive sensing

PCI Partial canonical identity

FT Fourier transform

DCT Discrete Cosine transform

DFT Discrete Fourier transform

DTFT Discrete-time Fourier transform

WSN Wireless sensor network

EH Energy harvesting

MDR Missing data recovery

MC Matrix completion

MF Matrix factorization

FC Fusion center

RF Radio frequency

CS Compressive sensing

WT Wavelet transform

KNN K nearest neighbour

SVT Singular value thresholding

CSI Channel state information

MIMO Multi-input-multi-output

ADC Analog-to-digital converter

CMOS Complementary metal oxide semiconductor

SNR Signal-to-noise-ratio

SNDR Signal-to-noise-distortion-ratio

RIP Restricted isometric property

mmWave Millimeter wave

NMSE Normalized mean square error

TNMSE Time average normalized mean square error

CT Continuous time

DT Discrete time

PDF probability density function

RV random variable

LTI linear time-invariant

WSS wide-sense stationary

PSD power spectral density

TEM Time encoding machine

Chapter 1

Introduction

The fifth generation (5G) wireless systems have the goal of reducing the power consumption by ten-fold, increasing the network capacity by thousand-fold, seamless user experience and global connectivity [4]. Most of the signals generated, transmitted or received in wireless systems are analog in nature. An analog signal contains both information and energy. Therefore, efficient systems should be designed that can extract the information as well as harvest the energy from the analog signal, which will help in meeting the goals of 5G wireless systems. However, using the informative signal for harvesting the energy will result in loss of information, and hence affects the system performance. Therefore, the objective of this thesis, "iDEG:integrated data and energy gathering for wireless systems" is to harvest the energy as well as information from the same signal without affecting the system performance for energy constrained applications. Here, the term *data gathering* implies recovering the complete data accurately from partial signal by sampling at a sub-Nyquist rate so that the remaining signal can be used for energy harvesting (EH). Furthermore, the term

energy gathering is used to denote the combined effect of energy saving and EH. This gathered energy will definitely reduce the energy consumption of the wireless systems and may also help in developing a self-sustainable device for critical applications of wireless systems.

The proposed method for data gathering has been discussed in Section 1.1. Followed by integrated data and energy gathering (iDEG) methods for various applications such as wireless sensor network (WSN), Sampling process and for correlated stochastic signals in Section 1.2, Section 1.3 and Section 1.4, respectively.

1.1 Data Gathering

As mentioned above, the term data gathering used in this thesis implies recovering the complete data from the partial signal by sampling at the sub-Nyquist rate. One of the growing field for sub-Nyquist sampling is compressive sensing (CS) [5, 6], which exploits the underlying structure of continuous-time (CT) signal to allow reconstruction from its low rate sampled version [7–11]. The effect of sub-Nyquist sampling has been studied in various applications, such as data recovery [12, 13], de-noising of data [14], channel capacity [15–17], source coding [18, 19] and channel estimation [20, 21]. The lower sampled version of the original signal is the compressive measurements of the signal, which can be represented as the multiplication of a matrix (known as sensing matrix) with the Nyquist sampled version of the original signal. CS theory states that the

original signal can be accurately reconstructed from its compressive measurements, if the signal has a sparse representation in the certain transform domain, such that the sparsifying domain is mutually incoherent with the sensing matrix. The conventionally popular sensing matrices are Gaussian and Bernoulli random matrices, which provide the linear combination of the original signal as the compressive measurements and have coherence with any fixed transform basis of the around square root of the length of the original signal sampled at the Nyquist rate [10]. The data acquisition process is demanding in terms of resources such as hardware cost, acquisition time and complexity.

In this thesis, *partial canonical identity (PCI)* sensing matrix is utilized to sense the data compressively. The PCI sensing matrix randomly selects the samples at sub-Nyquist rate instead of obtaining the linear combination of the data, and hence allows to harvest the energy from the un-utilized signal, which will help to meet the iDEG goal of the thesis, discussed in Section 1.2. PCI sensing matrix was proposed in [22] and reported to have inferior performance compared to random matrices such as Gaussian and Bernoulli. Likewise, it was also used with wavelet transform (WT) in [23] for CS based image reconstruction and observed to be inferior to Gaussian and Bernoulli matrices. We have investigated different transform domains such as discrete cosine transform (DCT) and Fourier transform (FT), where PCI sensing matrix is actually performing superior to the conventional Gaussian and Bernoulli matrices. We have computed the coherency of PCI sensing matrix with different transform basis to select an appropriate sparsifying basis that ensures good quality reconstruction

of the data. The computational complexity of PCI has been compared with the Gaussian and Bernoulli matrices. In addition, for further analysis, we have also compared the reconstruction performance of the PCI sensing matrix with various other sparse sensing matrices. The detailed description has been provided in Chapter 2 of this thesis.

Since PCI based CS framework (PCI-CS) can recover the entire data from a few random samples, it resembles the missing data recovery (MDR) framework. Therefore, we have also studied PCI-CS in the context of MDR, while also improving the data recovery problem in the presence of noise. To accomplish this, we have proposed a robust two-stage algorithm, named as *PCI-MF*. The first stage of this algorithm utilizes PCI-CS to recover the sparsest solution and the rank of the data from the partially available information, which are jointly utilized in the second stage to de-noise the data in a matrix factorization (MF) framework. This algorithms has been exploited for WSN application and also for millimeter wave (mmWave) communication. The salient contributions in both applications are elaborated below

1.1.1 WSN

WSN is a technology based on Internet of Things (IoT), built using various types of wireless sensor nodes to provide local and maybe even global connectivity. In recent years, with the advent of smart sensors, the design and deployment of WSNs have become an active area of research. Sensor nodes are typically deployed to measure environmental parameters/conditions such as temperature,

pressure, humidity, and vibration, etc. The measured value is transmitted to the fusion centre (FC) for further processing. In WSN applications, data loss is prevalent and generally arises due to hardware failures, channel fading, synchronization issues, collisions, and environmental blockage [24]. These missing values are required to be estimated accurately. The incorrect estimation of the missed raw data can lead to serious damage or casualty. For example, the underwater temperature measurements are used to determine the nature of ocean currents, helping in generating environmental alerts in case of any adversity. The above discussion clearly establishes the need for designing effective methods for recovering missing data in WSNs.

It is to be noted that WSN data is smoothly varying data, which results in sparsity in the DCT domain and also exhibit low-rank nature. This helps to utilize PCI-MF for WSN application.

We have compared PCI-MF with various well-known missing data recovery/matrix completion techniques such as interpolation, K nearest neighbour (KNN) [25], singular value thresholding (SVT) for nuclear norm minimization [26], matrix decomposition [27], and ESTI-CS methods [28]. The results have been computed on the realistic dataset of WSN [1]. It is to be noted that along with PCI-MF, we have also proposed two more algorithms in this context, which are performing better than the existing algorithms, however performing inferior with the PCI-MF. The detailed description has been provided in Chapter 3 of the thesis.

The robustness of PCI-MF algorithm has been further proved by recovering the complete channel state information (CSI) from partial information for mmWave massive multi-input-multiple-output (MIMO) wireless systems, discussed in the next section.

1.1.2 Mmwave communication

MmWave communication is a promising solution for providing gigabits-per-second data rates in cellular networks [29, 30]. However, transmission at such a high frequency also results in high path loss attenuation, and hence transmit beamforming using massive number of antennas is a common solution. This also requires perfect CSI estimation. The estimation of CSI is not practically feasible in mmWave massive MIMO systems. Therefore, to reduce the overhead, the problem of channel estimation in mmWave massive MIMO systems is formulated as either beam-alignment problem [31–33] or CS problem. However, in beam alignment, the transmitter and receiver search for the best beam pair, which increases the feedback overhead.

The performance of existing CS based methods [20, 21] is still restricted because these methods are not leveraging the known properties of mmWave massive MIMO channel matrix judiciously. In this thesis, PCI-MF has been used to recover the entire mmWave CSI by estimating only a few channel coefficients. Specifically, in this method, the few estimated noisy channel coefficients are represented as a combination of PCI and discrete Fourier transform (DFT) matrix in a CS framework to recover the sparsest solution of the channel matrix

by exploiting the fact that both PCI and DFT matrices are highly incoherent. The sparse matrix determined above has been used to recover the rank of the channel matrix. The knowledge of the rank, along with the sparse coefficients recovered above, have been used jointly in a MF framework to recover the actual channel matrix. PCI-MF has been compared with conventional matrix completion/missing data recovery framework [34] and state-of-the-art methods [20,21] for two different data sets by varying different parameters such as the number of transmitting and receiving antennas, antenna configurations, signal-to-noise ratio (SNR) and measurement ratio. In order to validate the proposed method for realistic applications, one data set is generated from real-world parameters obtained in the New York City [2,3]. The details have been provided in Chapter 4.

Note: After acquiring the data from the partial signal, the next step is to effectively utilize the remaining signal for energy harvesting. Therefore, in the next section, we will be discussing iDEG protocol for one of the most critical energy constrained application of wireless systems, i.e., WSN.

1.2 iDEG for WSN

As discussed in section 1.1.1, the sensor nodes deployed in WSN measure the physical parameters such as temperature, pressure, position, flow, humidity, vibration, force and motion to monitor the real-world applications. The output of a sensor node is generally an electrical signal, which is digitized using analog-to-

digital-converter (ADC) and transmitted to the FC after pre-processing. The FC processes the data received from all the nodes to take a global decision. The performance and lifetime of *practical WSNs* are generally limited by the amount of energy consumed, while sensing and transmitting the sensed data [35]. Moreover, sensors are usually deployed in remote locations where replacement or recharging of energy sources, i.e., batteries not always be possible, for instance, in dense forest, ocean beds, toxic environments, medical body area network (MBAN) and body area network (BAN). As a consequence, researchers are actively searching for methods to prolong the life of sensors by making sensors partially or fully battery independent. In order to achieve this, two avenues are generally followed, a) Power up nodes by harvesting energy either from ambient or human-generated sources [36, 37], prominent among them are, mechanical EH, solar EH, nano-sensor EH, bio-sensor EH, acoustic EH, thermal EH, wind EH, and wireless radio frequency (RF) EH. However, this will always require a dedicated source to charge the sensor nodes, which may not be possible. Moreover, a dedicated circuitry will also be required at the sensor nodes for harvesting this energy. This increases the size and complexity of nodes. b) Reducing the energy consumption of sensor nodes [12, 35, 38–47]. This can be done by allowing only a few selected nodes to participate in sensing and communicating the data to FC [35]. However, prohibiting some of the nodes from sending the sensed data may degrade the reliability of global decision made at FC. Therefore, effective "*data gathering*" at the sensor nodes is required, which can reduce the energy consumption of sensor nodes while maintaining the ac-

curacy at FC. Since WSN data is highly redundant [39], distributive coding and collaborative processing have been used to compress the sensor network data. This reduces the number of transmissions from sensor nodes to FC. However, these techniques rely on prior knowledge of correlation among nodes, sophisticated communication between nodes and FC, and increase in node capabilities which further enhance the complexity and energy consumption. CS has been used in WSN to eliminate the above-mentioned drawbacks [10, 12, 48]. The CS based data aggregation in WSN has been shown to reduce the network traffic. However, collection and transmission of the linear combination of data from all the nodes increase the energy consumption [12]. Therefore, [40–42] provide various energy efficient CS based routing algorithms to effectively collect the data. In addition to the above methods, significant research has also been devoted towards reducing the energy consumption of CS framework by reducing the number of measurements [43, 44] or by using a sparse measurement matrix [45–47]. These methods [40–47] (discussed in detail subsequently in Chapter 5) focused to cater the problem of effective data gathering only however does not consider simultaneous data and energy gathering.

As a consequence, in this thesis, an iDEG protocol has been proposed for WSN, which utilizes the proposed PCI-CS framework for data gathering that does not require the linear combination of original data, unlike the conventional CS based methods. This reduces the sensing time, computation cost, implementation complexity, the number of transmissions, and hence the energy losses, which helps to meet the energy gathering goal of iDEG. Along with energy sav-

ing, a new method has also been proposed to harvest energy at those sensor nodes which are not participating in the data gathering process from the signal received through sensing the physical parameter (discussed in detail in Chapter 5).

The energy harvesting from the un-utilized analog signal at sensor nodes motivated us to re-think the utility of the conventional sampling, specifically in the context of energy harvesting without affecting the data acquisition procedure of the sampling process. Therefore, in this thesis, we will be proposing iDEG framework for the sampling process. Hence, in the subsequent section, we try to answer the following question, can we harvest energy from analog signal during the sampling process?

1.3 *e*Sampling: Energy harvesting during sampling process

In general, real world signals are analog in nature. To capture these signals for further processing, or transmission, signals are converted into digital bits using ADC. In this conversion, a good amount of signal energy is wasted because the signal is captured only for a fraction of sampling duration, while the rest of the signal is discarded. In this context, we revisit the sampling process and proposes to harvest the discarded signal, naming the method as *eSampling*, i.e., sampling with energy harvesting. This harvested energy can be used to supplement the ADC itself, paving the way to the possibility of zero-power consumption and power-saving ADCs. The amount of energy harvested can be increased by re-

ducing the sampling rate. We analyze the tradeoff between the ability to recover the sampled signal and the energy harvested and provide guidelines for setting the sampling rate in the light of accuracy and energy constraints. Our analysis indicates that *e*Sampling ADCs operating with up to 12 bits per sample can acquire bandlimited analog signals such that they can be perfectly recovered (up to the distortion induced in quantization) without requiring power from the external source. Furthermore, our theoretical results reveal that *e*Sampling ADCs can infact save power by harvesting more energy than they consume. We show how these results imply that an *e*Sampling ADC acquiring a bandlimited signal at Nyquist rate with 8 bit ADCs can harvest over 15 dB more energy than it consumes in the conversion procedure. To verify the feasibility of *e*Sampling ADCs, we present a circuit-level design using standard complementary metal-oxide semiconductor (CMOS) 65 nm technology. An *e*Sampling 8-bit ADC which samples at 40 MHZ is designed on a Cadence Virtuoso platform. Our experimental study involving Nyquist rate sampling of bandlimited signals demonstrates that such ADCs are indeed capable of harvesting more energy than that spent during analog-to-digital conversion, without affecting the accuracy.

The *e*Sampling ADCs have a potential advantage in the IoT based applications. This is due to the fact that most of the sensor nodes are energy constrained nodes and generate an analog signal corresponding to the sensed parameter. This analog signal is converted into digital bits by using the sampling and quantization process. Hence, by replacing sampling with *e*Sampling, the discarded energy of the analog signal could be harvested to develop a self-sustainable

sensor node. To experimentally demonstrate that energy harvesting can be combined with sampling, we have provided a real-time validation of *e*Sampling ADC for sensing circuit for environmental and health monitoring application in Chapter 6.

1.4 iDEG using *e*Sampling for correlated stochastic signals

In Section 1.2, we have observed by utilizing the underlying structure of the analog signal, we can sample the signal at low sampling rate by utilizing PCI based compressive sensing, which also allows us to harvest the energy from the un-utilized signal. Further, in Section 1.3, we have observed we can harvest the input signal energy during the sampling process by utilizing *e*Sampling method. We have also observed the amount of energy harvested can be increased by reducing the sampling rate. However, for an unstructured signal, the PCI based CS method can not be utilized to reduce the sampling rate. Therefore, in this thesis, we have also studied iDEG for multiple correlated stochastic signals by exploiting the general correlation between the signals.

In Chapter 7, we have jointly *e*sampled and recovered the multiple correlated stochastic sources by exploiting their correlation at the reduced sampling rate, which also allowed us to harvest the more energy from the input analog signal. We derive the achievable reconstruction error, the maximum amount of energy harvested, and the corresponding sampling system for arbitrary sampling rates and spectral structures by designing an optimal analog combining and recon-

struction filter. Our numerical results illustrate that joint *e*sampling can achieve negligible reconstruction error and also maximizes the amount of harvested energy from the input analog signals.

1.5 Research Objectives

The research objectives of this dissertation are to retrieve the complete information from the partial signal so that the remaining signal can be used for energy harvesting. Hence, two-dimensional objectives of this dissertation are elaborated below:

- To improve the performance of the recovery algorithm that allows full data recovery from a very few samples even under a noisy scenario. This has been done by examining different properties of the signal such as sparsity, low-rank and correlation in the data and for different applications such as WSN, mmWave communication and for wide sense stationary (WSS) signals.
- To harvest the energy from the un-utilized analog signal without affecting the system performance, for instance, harvesting energy during the conventional sampling process of an ADC. In addition, to improve the amount of harvested energy by reducing the sampling rate of ADCs and also by designing the optimal filters.

1.6 List of Publications

The papers that contributed to this dissertation are the following.

1.6.1 Journals

1. **N. Jain**, N. Shlezinger, Y.C. Eldar, B. Tiwari, A. Gupta, V.A. Bohara and P.G. Bahubalindruni, “eSampling: Energy Harvesting ADCs” submitted to *IEEE Transaction on Signal processing*, 2020.

2. **N. Jain**, V. A. Bohara and A. Gupta, "PCI-MF: Partial Canonical Identity and Matrix Factorization Framework for Channel Estimation in mmWave Massive MIMO Systems," in IEEE Open Journal of Signal Processing, vol. 1, pp. 135-145, 2020, doi: 10.1109/OJSP.2020.3020002.

3. **N. Jain**, A. Gupta and V. A. Bohara, "PCI-MDR: Missing Data Recovery in Wireless Sensor Networks Using Partial Canonical Identity Matrix," in IEEE Wireless Communications Letters, vol. 8, no. 3, pp. 673-676, June 2019, doi: 10.1109/LWC.2018.2882403.

4. **N. Jain**, V. A. Bohara and A. Gupta, "iDEG: Integrated Data and Energy Gathering Framework for Practical Wireless Sensor Networks Using Compressive Sensing," in IEEE Sensors Journal, vol. 19, no. 3, pp. 1040-1051, 1 Feb.1, 2019, doi: 10.1109/JSEN.2018.2878788.

1.6.2 Conferences

1. **Neha Jain**, Nir Shlezinger, Yonina C. Eldar, Anubha Gupta and Vivek Ashok Bohara, "Energy Harvesting via Analog-to-digital conversion" *European signal processing conference (EUSIPCO)*, 2020.

2. **Neha Jain**, Navneet Anand Sah, Vivek Ashok Bohara and Anubha Gupta, "Experimental Results for Energy Harvesting by exploiting inherent inadequacies of Sampling process for IoT application" *IEEE International Conference on Communications (ICC), Workshop*, 2020.

3. **Neha Jain**, Anubha Gupta and Vivek Ashok Bohara, “TS-MC: Two stage matrix completion algorithm for wireless sensor network” *International Conference on Acoustics, Speech, and Signal Processing (ICASSP)*, 2019.

4. **Neha Jain**, Vivek Ashok Bohara and Anubha Gupta, “Sparse signal recovery and energy harvesting for potential 5G applications” in *International Conference on Mobile Computing and Networking (MobiCom)*, 2018, (**Second position in Student Research competition (SRC)**)

5. **Neha Jain**, Vivek Ashok Bohara and Anubha Gupta, ”Compressive Cooperative Communication with Decode and Forward Relay” in *International Conference on Communication systems and networks (COMSNETS) Poster session*, 2016. (**Best Poster Award Honourable Mentioned**)

1.6.3 Patents

1. A system and method of energy harvesting during analog signal sampling. Indian patent filled in March, 2018. Application no. 201811008597. [Inventors: **Neha Jain**, Vivek Ashok Bohara, Anubha Gupta].

1.7 Thesis Organisation

This dissertation is organized as follows.

Notation: Matrices and vectors are written in capital bold letters and small bold letters, respectively, whereas scalars are written in italics. Furthermore, $\mathbf{X}'$, $\mathbf{X}^*$ and $\mathbf{X}^H$ denotes the transpose, conjugate and the Hermitian (conjugate transpose) of matrix $\mathbf{X}$, respectively. The element corresponding to i^{th} row and j^{th} column of a matrix $\mathbf{X}$ is represented as $X(i,j)$. The i^{th} element of a vector $\mathbf{x}$ is represented as $x(i)$. The vectorization of matrix $\mathbf{X}$ is denoted as $\mathbf{X}(:)$. $\mathbf{X} \otimes \mathbf{Y}$ and $\mathbf{X} \odot \mathbf{Y}$ represents Kronecker and Hadamard product between matrix $\mathbf{X}$ and $\mathbf{Y}$, respectively. The l_p norm of a matrix or a vector is represented as $||\cdot||_p$. A binary, complex and real matrix of size $a \times b$ is represented by $\mathbb{B}^{a\times b}$, $\mathbb{C}^{a\times b}$ and $\Re^{a\times b}$, respectively.

- Chapter 2 introduces basic concepts of CS followed by proposed partial canonical identity based compressive sensing (PCI-CS) and its properties. PCI-CS has been examined on WSN application. The simulation results have been computed on WSN data taken from Intel lab [1].

- In Chapter 3, PCI-CS has been studied in the context of missing data recovery. The algorithm has been further improved by introducing a second stage of reconstruction. This algorithm has been compared with various missing data recovery algorithms for WSN data.
- In Chapter 4, the proposed algorithm has been further verified by recovering the complete CSI from partial knowledge of the channel in mmwave massive MIMO wireless systems. The work has been compared with state-of-the-art methods.
- In Chapter 5, an integrated data and energy gathering protocol for WSN has been proposed, which focuses on energy saving and energy harvesting for WSN, while reconstructing the data using PCI-CS framework.
- Chapter 6 proposes a method of harvesting energy from the analog signal during the sampling process without affecting the performance of an ADC. The work has been examined through analysis, simulations as well as experimentally.
- In Chapter 7, an iDEG solution utilizing *e*Sampling has been proposed for the unstructured signal such as correlated WSS signal. The system jointly *e*sampled and reconstructed the multiple correlated stochastic signals by designing an optimal analog combining and reconstruction filter.
- Finally, Chapter 8 concludes this dissertation along with the suggested future research directions.

Chapter 2

Partial Canonical Identity based Compressive Sensing applied to Wireless Sensor Networks

2.1 Introduction to Compressive sensing

Compressive sensing (CS), also known as sub-Nyquist sampling and sparse sampling is a signal processing technique, which allows acquisition of the signal at a rate much below the Nyquist sampling rate [7–9]. For instance, according to the Shannon-Nyquist sampling theorem, a signal can be recovered if it's acquired at a rate twice the maximum signal frequency. However, if the signal is exactly or approximately sparse in some transform domain, then a few compressive measurements (less than Nyquist rate) of the original signal is sufficient to recover the original signal, if certain conditions are satisfied [48]. A signal is called exactly k-sparse if it has only k number of non-zero elements and all the

remaining elements are zero. While a signal is called approximately k-sparse, if the signal has only k number of entries with large coefficients and all remaining entries are tending to zero. CS has been utilizing in various applications, such as magnetic resonance imaging, high-speed video acquisition, and ultra-wideband communication.

Let us illustrate the concept of CS through a brief example. The M compressive measurements of a signal $\mathbf{x}$ (to be recovered) of length N can be written as

$$\mathbf{y} = \mathbf{\Phi x}, \tag{2.1}$$

where $\mathbf{\Phi}$ is a $M \times N$ sensing matrix and $M << N$. In general, $\mathbf{\Phi}$ is a Gaussian or Bernoulli matrix that provides linear combinations of $\mathbf{x}$ in $\mathbf{y}$. Let $\mathbf{x}$ is sparse in $\mathbf{\Psi}$ domain, i.e., $\mathbf{s} = \mathbf{\Psi x}$, where $\mathbf{s}$ is the sparse representation of $\mathbf{x}$. Therefore, $\mathbf{y}$ can also be written as:

$$\begin{aligned} \mathbf{y} &= \mathbf{\Phi \Psi}^{-1}\mathbf{s} \\ &= \mathbf{As} \qquad (\because \mathbf{A} = \mathbf{\Phi \Psi}^{-1}), \end{aligned} \tag{2.2}$$

where $\mathbf{A}$ of size $M \times N$ is termed as the measurement matrix.

The sparse signal $\mathbf{x}$ can be recovered from $\mathbf{y}$ if either the *Restricted isometric property (RIP)* or the *Mutual incoherence property* is satisfied by matrix $\mathbf{A}$. These properties can be understood as follows.

A matrix $\mathbf{A}$ is said to satisfy *RIP*, if there exists $\delta_k \in (0, 1)$ for all k-sparse

signals **s** such that

$$(1-\delta_k)\,||\mathbf{s}||_2^2 \leq ||\mathbf{A}\,\mathbf{s}||_2^2 \leq (1+\delta_k)\,||\mathbf{s}||_2^2. \tag{2.3}$$

The *mutual incoherence property* is said to be satisfied by matrix **A** if the sensing matrix $\mathbf{\Phi}$ and the sparsifying basis $\mathbf{\Psi}^{-1}$ are incoherent, where the coherence between the sensing matrix and the transform basis can be calculated as:

$$\mu(\mathbf{\Phi}, \mathbf{\Psi}^{-1}) = \sqrt{N} \max_{\forall i,j} \frac{\left|\left\langle \mathbf{\Phi}_i, \mathbf{\Psi}_j^{-1} \right\rangle\right|}{\left\|\mathbf{\Phi}_i\right\|_2 \left\|\mathbf{\Psi}_j^{-1}\right\|_2}, \tag{2.4}$$

where $\mathbf{\Phi}_i$ is the i^{th} row of $\mathbf{\Phi}$ and $\mathbf{\Psi}_j^{-1}$ is the j^{th} column of $\mathbf{\Psi}^{-1}$. It should be noted that $\mu(\mathbf{\Phi}, \mathbf{\Psi}^{-1}) \in [1, \sqrt{N}]$, and hence $\mu = 1$ represents maximum incoherence between the matrices. It is observed that the random matrices like Gaussian and Bernoulli follow the above constraints with mutual coherence of $\sqrt{2\log N}$ [10].

Note: CS framework can also be utilized with noisy input signal, in such a case, the obtained CS measurements will be written as

$$\begin{aligned} \mathbf{z} &= \mathbf{\Phi}(\mathbf{x}+\mathbf{n}) \\ &= \mathbf{\Phi}(\mathbf{\Psi}^{-1}\mathbf{s}+\mathbf{n}) \\ &\overset{(a)}{=} \mathbf{A}\mathbf{s}+\mathbf{n} \quad (\because \mathbf{A} = \mathbf{\Phi}\mathbf{\Psi}^{-1}), \end{aligned} \tag{2.5}$$

where (a) follows from the fact that noise vector, **n** is the random AWGN (additive white Gaussian noise), and hence $\mathbf{\Phi n}$ can be written as **n**.

2.2 Partial Canonical identity based CS (PCI-CS)

In this thesis, we have proposed a partial canonical identity (PCI) sensing matrix, which randomly selects M elements of **x**, instead of obtaining the M linear combination of **x**, unlike the conventional Gaussian and Bernoulli matrices. Therefore, the compressive measurements of **x** using PCI sensing matrix will be given by $\mathbf{y} = [x_1\ x_2\ ...x_M]'$. It can be visualized as follows

$$\mathbf{y} = \begin{bmatrix} x_1 \\ x_4 \\ \vdots \\ x_N \end{bmatrix}_{M\times 1} = \begin{bmatrix} 1 & 0 & 0 & 0 & 0 & 0 & ... & 0 \\ 0 & 0 & 0 & 1 & 0 & 0 & ... & 0 \\ \vdots & \vdots & \vdots & \vdots & \vdots & \vdots & ... & \vdots \\ 0 & 0 & 0 & 0 & 0 & 0 & ... & 1 \end{bmatrix}_{M\times N} \begin{bmatrix} x_1 \\ x_2 \\ x_3 \\ x_4 \\ \vdots \\ x_N \end{bmatrix}_{N\times 1}$$

$$= \mathbf{\Phi x}, \tag{2.6}$$

where $\mathbf{\Phi}$ is an $M \times N$ PCI sensing matrix, where each element of $\mathbf{\Phi}$ is given by

$$\Phi(i,j) = \begin{cases} 1 & 1 \leq i \leq \boldsymbol{M}, j = m, \text{where } m \in [1, \boldsymbol{N}] \\ & \text{and all } m \text{ are distinct.} \\ 0 & \text{otherwise.} \end{cases} \tag{2.7}$$

It can be observed that no multiplication or addition is required to compute **y** from **x** using PCI sensing matrix. On the other hand, if $\mathbf{\Phi}$ is a Gaussian matrix, then MN multiplications and $M(N-1)$ additions are required to compressively

sense the data. Similarly, if $\mathbf{\Phi}$ is a Bernoulli matrix, then $M(N-1)$ additions are required (refer to Table 2.1). Thus, the computational complexity associated with the sensing of data is greatly reduced with PCI matrix compared to the conventionally popular random sensing matrices.

Table 2.1: Computational Complexity of PCI and conventional sensing matrices.

Sensing Matrix ($\mathbf{\Phi}$)	Multiplications	Additions
Gaussian	MN	$M(N-1)$
Bernoulli	0	$M(N-1)$
PCI	0	0

Further, in order to recover the complete data from compressive measurements, the sensing matrix should be mutually incoherent with the transform basis. For the PCI sensing matrix, the expression of coherence (2.4) reduces to

$$\mu(\text{PCI}, \mathbf{\Psi}^{-1}) = \sqrt{N} \max_{\forall i,j} \frac{|\Psi^{-1}(i,j)|}{||\mathbf{\Psi}_j^{-1}||_2}. \tag{2.8}$$

The coherence value of PCI sensing matrix with various transform basis is provided in Table 2.2. From this table, it is observed that the PCI matrix is highly incoherent with FT (and inverse FT) and DCT (and inverse DCT) with coherence values of 1 and $\sqrt{2}$, respectively, that are independent of the length of input vector $\mathbf{x}$. However, the coherence of Gaussian and Bernoulli random matrices with any fixed basis is approximately $\sqrt{2 \log N}$ [10]. Thus, PCI matrix is more incoherent with FT, IFT, DCT and IDCT basis matrices as compared to Gaussian and Bernoulli matrices. However, in the wavelet domain, the coherence of Gaussian and Bernoulli matrices is proportional to $\sqrt{\log N}$, but coherence of

PCI matrix is quite large and proportional to $\sqrt{N}$. Fig. 2.1 compares the coherence of PCI matrix with the conventional random sensing matrices (Gaussian and Bernoulli) for different transform basis on values of N ranging from 50 to 500. We note that PCI sensing matrix has low coherence with FT and DCT and hence, can be effectively utilized with these sparsifying matrices in CS based applications. One such application is wireless sensor networks (WSN) discussed in the next section of this chapter.

Table 2.2: Coherence between PCI sensing matrix and various transform basis.

$\mathbf{\Psi}^{-1}$	μ	$\mathbf{\Psi}^{-1}$	μ
FT/IFT	1	db3 wavelet	$0.8069\sqrt{N}$
DCT/IDCT	$\sqrt{2}$	db4 wavelet	$0.7148\sqrt{N}$
Haar Wavelet	$0.7071\sqrt{N}$	coif2 wavelet	$0.8127\sqrt{N}$
db2 wavelet	$0.8365\sqrt{N}$	coif4 wavelet	$0.7822\sqrt{N}$

Note: Selecting M elements of $\mathbf{x}$ is equivalent to obtaining the M linear combinations of $\mathbf{s}$. This can be understood from Fig. 2.2.

2.3 PCI-CS applied to WSN

As mentioned in section 2.2, PCI matrix is highly incoherent with DCT and FT basis, and hence if the data is sparse in such domain, PCI based CS can be effectively used to reduce the sensing cost as well as to improve the performance.

Indeed, the WSN data is sparse in the DCT domain as seen from the plot of sorted DCT coefficients in Fig. 2.3. The coefficients are plotted for the temperature data taken from the Intel Lab [1]. The signal is less smooth in the

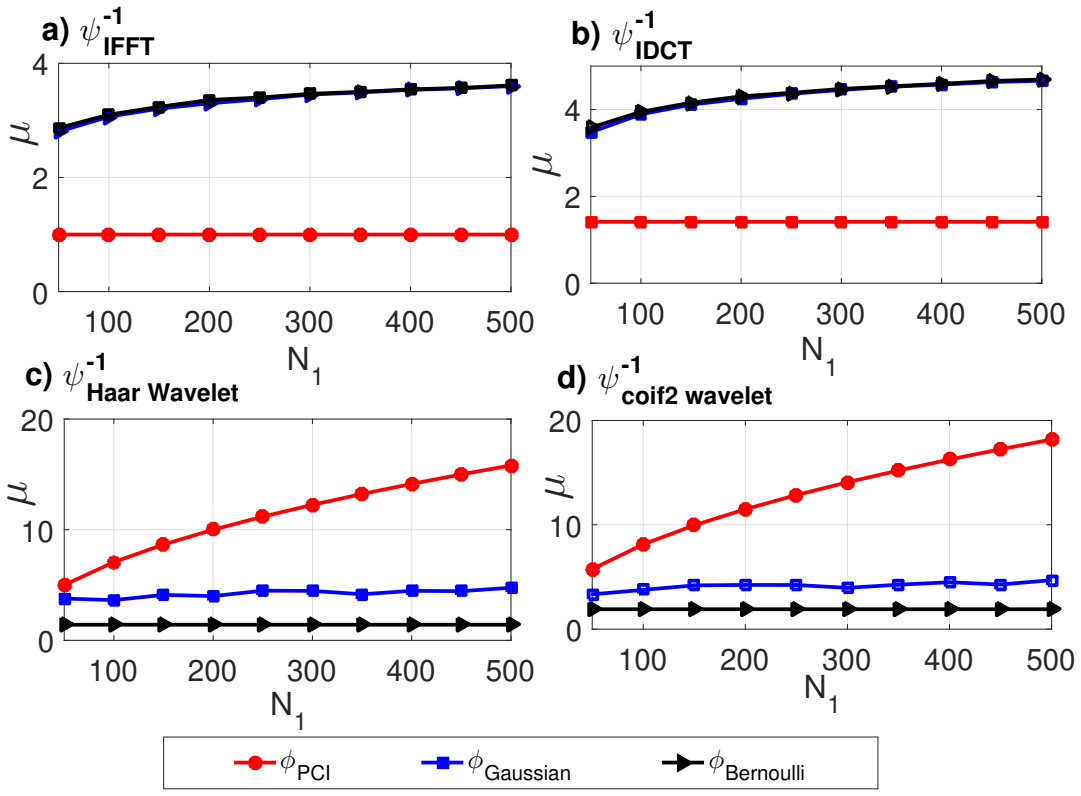

Figure 2.1: Coherence of PCI, Gaussian, and Bernoulli sensing matrices with a) IFT b) IDCT c) Haar wavelet d) coif2 wavelet for different value of N.

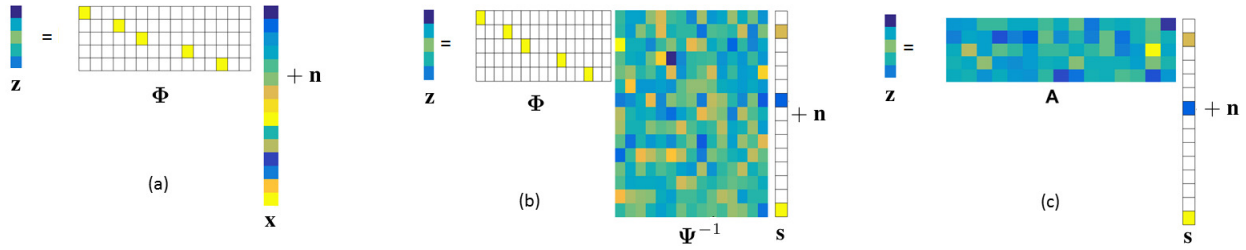

Figure 2.2: Each block is filled with some color that corresponds to some integer value. For example, white represents '0', and the yellow represents '1'. a) $\mathbf{z}$ is compressively sensed data of $\mathbf{x}$, but $\mathbf{\Phi}$ is chosen such that $\mathbf{z}$ contains few randomly sensed samples of $\mathbf{x}$. (b) Replace $\mathbf{x}$ by $\mathbf{\Psi}^{-1}\mathbf{s}$ in (a), $\mathbf{\Psi}^{-1}$ is the sparsifying basis matrix and $\mathbf{s}$ is the sparse vector. (c) Although $\mathbf{z}$ is obtained by randomly picking up a fewer sample of $\mathbf{x}$, mathematically this is equivalent to taking linear combinations of $\mathbf{s}$.

spatial domain as compared to the time domain because nodes are randomly distributed in the spatial domain. Hence, from Fig. 2.3, we observe that the data is less sparse in the spatial domain as compared to the time domain. The smoothness of the signal is captured by the parameter called Hurst exponent (H). If $H > 0.5$, the signals are smoother and their KL (Karhunen–Loeve) basis can be approximated by DCT [49]. In order to validate this, we computed the Hurst exponent, H of the considered data [1], and it was observed to be nearly 0.7 in the time domain. Correspondingly, we also generated the synthetic data with $H = 0.8$. The DCT coefficients of both synthetic and real data have been plotted in Fig. 2.3. We observe that both synthetic and real data are sparse in the DCT domain.

The reconstruction of the entire data from compressive measurements obtained through PCI sensing matrix by exploiting sparsity in the DCT domain has been discussed in the subsequent section.

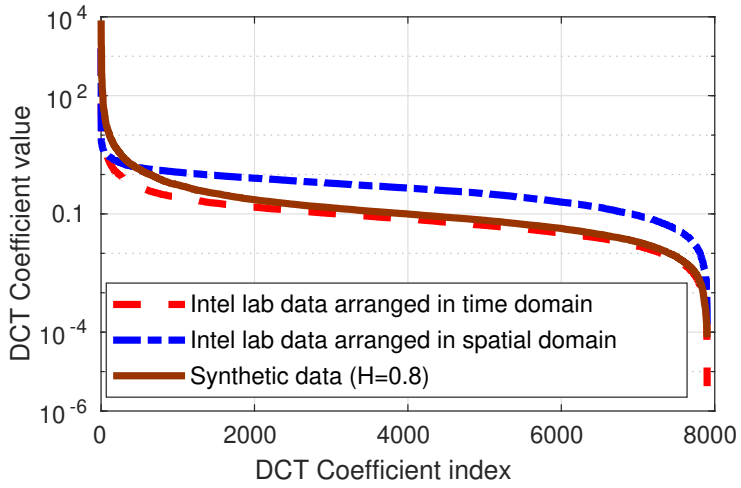

Figure 2.3: Sorted DCT coefficients of WSN Intel lab data [1] and synthetic data.

2.3.1 Reconstruction

WSN data is smoothly varying in both the spatial and temporal domain and results in DCT sparsity due to both domains. Therefore, in Section 2.3.1.1 and Section 2.3.1.2, we have shown the mathematical representation for exploiting both domains' sparsity separately and jointly, respectively.

2.3.1.1 Single sparsity

The DCT sparsity either due to the spatial domain or due to the temporal domain can be exploited as follows to reconstruct the complete data from the compressive measurements.

Assuming the data samples x_1, x_2... x_N of input signal **x** are either time domain or the spatial domain samples based upon the type of sparsity we would like to exploit. The sparse representation of signal **x**, i.e., **s** can be recovered from compressive measurements, **y** by using following l^1 minimization prob-

lem, if any of the mentioned conditions of CS (2.3), (2.4) is satisfied,

$$\min_{s} ||\mathbf{y} - \mathbf{As}||_2^2 + \lambda||\mathbf{s}||_1, \tag{2.9}$$

where λ is the regularization parameters to control the level of sparsity and the data accuracy. Iterative soft thresholding method (ISTA) [50] can be used to solve (2.9). The sparse vector, $\mathbf{s}$ determined above can recover the original signal $\mathbf{x}$ by using $\mathbf{x} = \mathbf{\Psi}^{-1}\mathbf{s}$.

2.3.1.2 Double Sparsity

In this section, we will exploit both spatial and temporal sparsity jointly to reconstruct complete data from compressive measurements. Consider the WSN data $\mathbf{X}$ for N nodes at T time instants as

$$\mathbf{X} = \begin{bmatrix} x_1^{(1)} & x_1^{(2)} & x_1^{(3)} & \dots & x_1^{(T)} \\ x_2^{(1)} & x_2^{(2)} & x_2^{(3)} & \dots & x_2^{(T)} \\ \vdots & \vdots & \vdots & \dots & \vdots \\ x_N^{(1)} & x_N^{(2)} & x_N^{(3)} & \dots & x_N^{(T)} \end{bmatrix}_{N \times T} \tag{2.10}$$

where $x_i^{(j)}$ represents data of i^{th} sensor at j^{th} time instant. Since data is correlated in both the spatial and temporal domains, it is assumed to be sparser in $\mathbf{\Psi}_1$ domain due to spatial correlation and sparser in $\mathbf{\Psi}_2$ domain due to temporal correlation. Thus, the sparse representation of $\mathbf{X}$ can be written as $\mathbf{S} = \mathbf{\Psi}_1\mathbf{X}\mathbf{\Psi}_2'$, or

$$\mathbf{X} = \mathbf{\Psi}_1^{-1}\mathbf{S}(\mathbf{\Psi}_2')^{-1}. \tag{2.11}$$

Furthermore, (2.11) can be written in the vectorized form using the Kronecker multiplication of basis matrices as [51],

$$\begin{aligned}\mathbf{x} = \text{vec}(\mathbf{X}) &= (\mathbf{\Psi}_2^{-1} \otimes \mathbf{\Psi}_1^{-1})\text{vec}(\mathbf{S}) \\ &= (\mathbf{\Psi}_2^{-1} \otimes \mathbf{\Psi}_1^{-1})\mathbf{s}. \end{aligned} \tag{2.12}$$

Thus, the reconstructed signal can be written as

$$\begin{aligned}\mathbf{y} &= \mathbf{\Phi}(\mathbf{\Psi}_2^{-1} \otimes \mathbf{\Psi}_1^{-1})\mathbf{s}, \\ &= \mathbf{As} \quad (\because \mathbf{A} = \mathbf{\Phi}(\mathbf{\Psi}_2^{-1} \otimes \mathbf{\Psi}_1^{-1})). \end{aligned} \tag{2.13}$$

Equation (2.13) can be solved using the convex optimization formulation given in (2.9) and accordingly, $\hat{\mathbf{x}}$ can be recovered from $(\mathbf{\Psi}_2^{-1} \otimes \mathbf{\Psi}_1^{-1})\hat{\mathbf{s}}$.

2.3.2 Simulation Results

In this section, the PCI sensing matrix has been compared with the conventional Gaussian and Bernoulli sensing matrices. To ascertain performance improvement with the proposed methodology, the PCI sensing matrix based recovery has also been compared with various sparse sensing matrices [42, 52, 53]. Graphs are plotted for different compressive sampling ratios with normalized mean square error (NMSE) [1] as the performance metric of data recovery.

For the proof-of-concept demonstration and practical verification of the proposed work, simulations are performed on a real data set of Intel lab [1]. This

[1] NMSE=$\frac{||\mathbf{x}-\hat{\mathbf{x}}||_2^2}{||\mathbf{x}||_2^2}$, where $\mathbf{x}$ is the original data and $\hat{\mathbf{x}}$ is the recovered data.

data was collected in the Intel Berkeley Research Lab between 28^{th} Feb and 5^{th} April 2004. Mic2Dot sensors were arranged in a Lab of dimension $40\text{m} \times 20\text{m}$ to collect readings of temperature, humidity, light, and voltage. We have chosen the day of 28^{th} Feb [2] with data value at each minute for the 52 sensors[3]. The matrix $\mathbf{X}$ in (2.10) is filled with temperature values such that $N = 52$ represents the number of sensor nodes and $T = 500$ represents the total number of timestamps.

Further, this dataset is observed to have some missing entries. This is an obvious scenario for practical WSNs, where some data points may not be available due to environmental factors, channel conditions, faulty sensors, etc. Since conventional CS based methods with Gaussian sensing matrices require the linear combination of data, these entries are filled by techniques such as linear interpolation, KNN [25], or by using statistical methods of data estimation in sensor networks [54]. For example, this particular dataset has 6593 missing entries from the total of 26,000 entries (52×500), i.e., 25.36% of data is not available. Thus, in order to apply CS on the complete data set, the conventional Gaussian and Bernoulli sensing matrices will first interpolate these values to compute the M random linear projections of the dataset. This process may also lead to noisy recovery because of the inherent noise in filling the missing entries that would further lead to cumulative noise owing to picking up linear combinations. However, the proposed PCI matrix is self-sufficient in estimating the missing entries without any additional noise in sensing and doesn't require any

[2] The chosen date has no impact on the results. The pattern will be similar for any other date.

[3] Out of 54 sensors, 52 sensors have been chosen because data value for the 5th and 28th sensor was not available

complementary method to fill the missing data. This saves both time and energy and also leads to better performance. The contribution of the proposed work in terms of missing data recovery has been elaborated in Chapter 3.

2.3.2.1 Single Sparsity with Spatial Correlation

In this section, we have exploited the spatial correlation of the data. Accordingly, data is obtained by vectorizing matrix $\mathbf{X}$ as

$$\mathbf{x} = \begin{bmatrix} x_1^{(1)} \dots & x_N^{(1)} & x_1^{(2)} \dots & x_N^{(2)} \dots & x_1^{(T)} \dots & x_N^{(T)} \end{bmatrix}' \text{ or,}$$

$$\mathbf{x} = \begin{bmatrix} x_1^{(1)} \dots & x_N^{(1)} & x_N^{(2)} \dots & x_1^{(2)} \dots & x_1^{(T)} \dots & x_N^{(T)} \end{bmatrix}'.$$

The length of vector $\mathbf{x}$ for our case is $N_T = N \times T = 26000$. However, due to missing entries only $N_a = 19407$ samples are present ($N_T > N_a$). Therefore, the analysis is performed on the known data only. For instance, at sampling ratio=0.5, the number of obtained measurements, i.e., M_a will be equal to $0.5 \times N_a$. Fig. 2.4 presents NMSE computed at N_a sample points (denoted as, NMSE_{N_a}) with various sensing matrices, i.e., PCI, Gaussian, and Bernoulli matrices at different sampling ratios ($\frac{M_a}{N_a}$) varied from 0.1 to 0.9. DCT is chosen as the sparsifying domain. From Fig. 2.4, we observe that the PCI sensing matrix outperforms both Gaussian and Bernoulli matrices at all sampling ratios. Hence, it is evident from the discussion in Section 2.2 and Fig. 2.4 that PCI sensing matrix reduces the computational complexity and improves the NMSE performance.

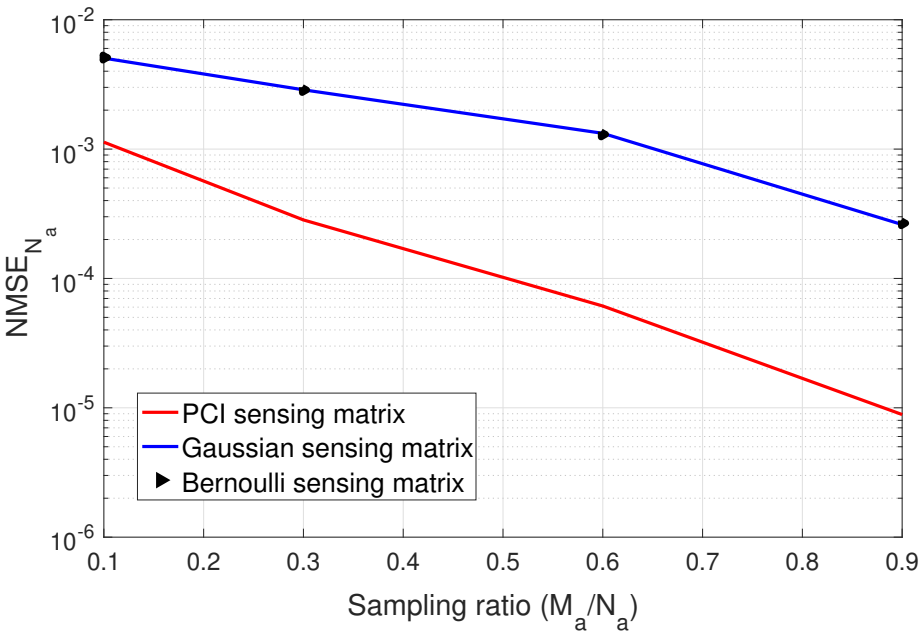

Figure 2.4: NMSE_{N_a} obtained with PCI, Gaussian, and Bernoulli sensing matrices by exploiting spatial correlation.

Consider Fig. 2.5 for the visual illustration of the obtained results. This figure shows the temperature values corresponding to the original dataset of length $N_a = 19407$ and the recovered data using all three sensing matrices at a sampling ratio of 60%, i.e., $\frac{M_a}{N_a} = 0.6$. From this figure, it can be observed that the data recovered from the PCI sensing matrix is close to the original data as compared to Gaussian and Bernoulli sensing matrices.

2.3.2.2 Single Sparsity with Time Correlation

In this section, we have exploited the time correlation of the data. Accordingly, data is obtained by vectorizing matrix $\mathbf{X}$

$$\mathbf{x} = \left[x_1^{(1)} \ldots \quad x_1^{(T)} \quad x_2^{(1)} \ldots \quad x_2^{(T)} \ldots \quad x_N^{(1)} \ldots \quad x_N^{(T)} \right]' \text{ or,}$$

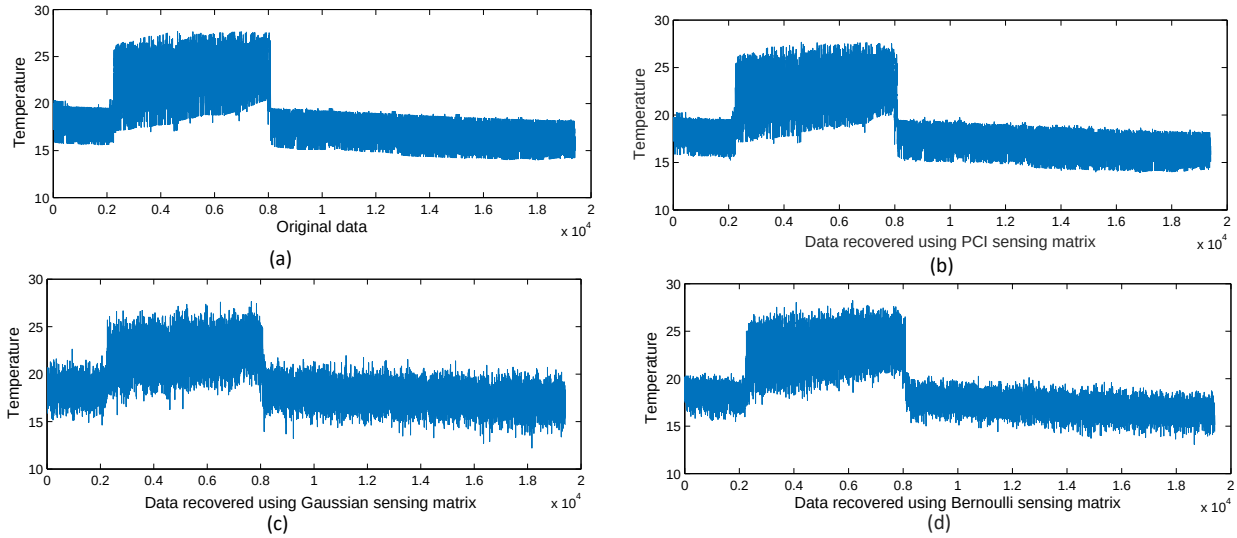

Figure 2.5: Temperature values of a) Original data b), c) and d) recovered data using PCI, Gaussian and Bernoulli sensing matrix respectively at 60% sampling ratio.

$$\mathbf{x} = \left[x_1^{(1)} \ldots \; x_1^{(T)} \;\; x_2^{(T)} \ldots \;\; x_2^{(1)} \ldots \;\; x_N^{(1)} \ldots \;\; x_N^{(T)} \right]'.$$

Again, $\mathbf{x}$ should be of length N_T. However, owing to missing entries, only N_a samples are present. Fig. 2.6(a) presents NMSE_{N_a} obtained with various sensing matrices, i.e., PCI, Gaussian, and Bernoulli matrices at different sampling ratios $(\frac{M_a}{N_a})$ varied from 0.1 to 0.9. Again, DCT is chosen as the sparsifying domain. From this figure, it is observed that Gaussian and Bernoulli's matrices perform better than PCI for $\frac{M_a}{N_a} < 0.4$. This is because, for low values of sampling ratio, there could be a case where no data is sensed from any particular sensor while using the PCI sensing matrix. It is obvious that while exploiting time correlation, we must have samples from all the sensor nodes as all nodes are independent, unlike the case of spatial correlation, where the data is estimated with the help of neighbouring nodes. To mitigate the above drawback, we have considered the following two cases:

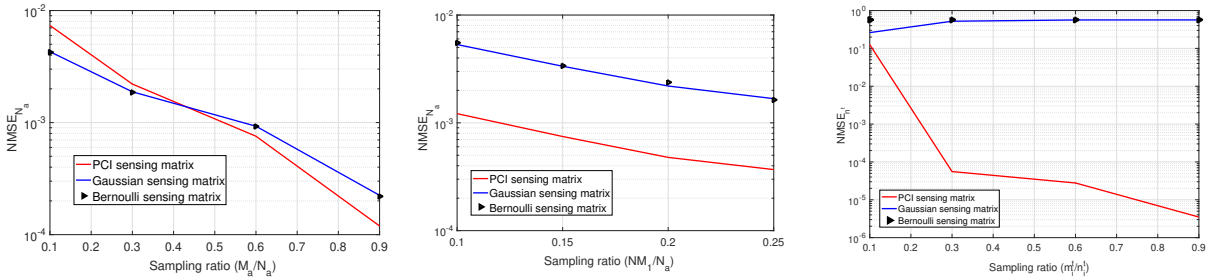

(a) *Exploiting time correlation* (b) *Case-1* (c) *Case-2*

Figure 2.6: NMSE_{N_a} obtained with PCI, Gaussian, and Bernoulli sensing matrices by exploiting time correlation for different cases.

Case-1: Here, the data of all the nodes at all timestamps is vectorized, with a constraint that the same number of data is sensed from each of the sensor nodes. Therefore, if the minimum available data for 500 timestamps at any sensor node is M_1, then sampling ratio will be equal to $\frac{NM_1}{N_a}$ The results for this is provided in Fig. 2.6(b), from where we can observe that the PCI matrix is outperforming the conventional sensing matrices.

Case-2: The reconstruction algorithm at each sensor node is applied separately as data is considered to be time correlated. Therefore, if n_i^t samples are available at i^{th} sensor node such that $\sum_{i=1}^{N} n_i^t = N_a$, then the number of measurements picked from each sensor node can be given as m_i^t = sampling ratio $\times n_i^t$. The NMSE for each sensor node on available n_i^t samples is computed separately. Further, the mean of obtained NMSEs, denoted as NMSE_{n^t} is plotted in Fig. 2.6(c). As mentioned before, $T = 500$ timestamps are taken for each sensor node, and all the corresponding entries are not available. In 500 timestamps, the maximum filled entries at a particular sensor is 490 whereas, the minimum is 139 (such that $(n_i^t \in [139, 490])$). For such a low number of observations, both the conventional methods are giving a very high value of NMSE. However,

the PCI sensing matrix is still performing better, as shown in Fig. 2.6(c).

2.3.2.3 Double sparsity with both space and time correlation

In this section, both time and space correlation are exploited on the matrix **X**. For both the dimensions, DCT sparsifying domain is taken. As mentioned before, missing entries are present and conventional sensing matrices can't be applied in this case as they take the linear combination of the data. Therefore, the technique like linear interpolation is first used to fill the missing entries of the matrix **X** and then compressive sensing is applied for Gaussian and Bernoulli matrix [25]. However, such an interpolation technique is not required while sensing with PCI sensing matrix as it is self-sufficient in estimating the missing entries. In Fig. 2.7, $NMSE_{N_a}$ with sampling ratio ($\frac{M_a}{N_a}$) is plotted for for PCI, Gaussian and Bernoulli sensing matrix. We can observe the PCI sensing matrix outperforms the conventional matrices, without using the interpolation technique.

2.3.2.4 Reconstruction performance of different sparse random matrices

In this section, we have compared the reconstruction performance of the PCI sensing matrix with different sparse random sensing matrices. The considered sparse sensing matrices are described below:

- A binary matrix, $\mathbf{\Phi_1}$ [42, 52] given as

$$Pr(\Phi_1(i,j) = w) = \begin{cases} p & w = 0 \\ 1-p & w = 1 \\ 0 & \text{otherwise,} \end{cases} \quad \forall i, j$$

where $\Phi_1(i,j)$ is the element of the matrix $\mathbf{\Phi_1}$. The considered value of p is 0.5 and 0.3.

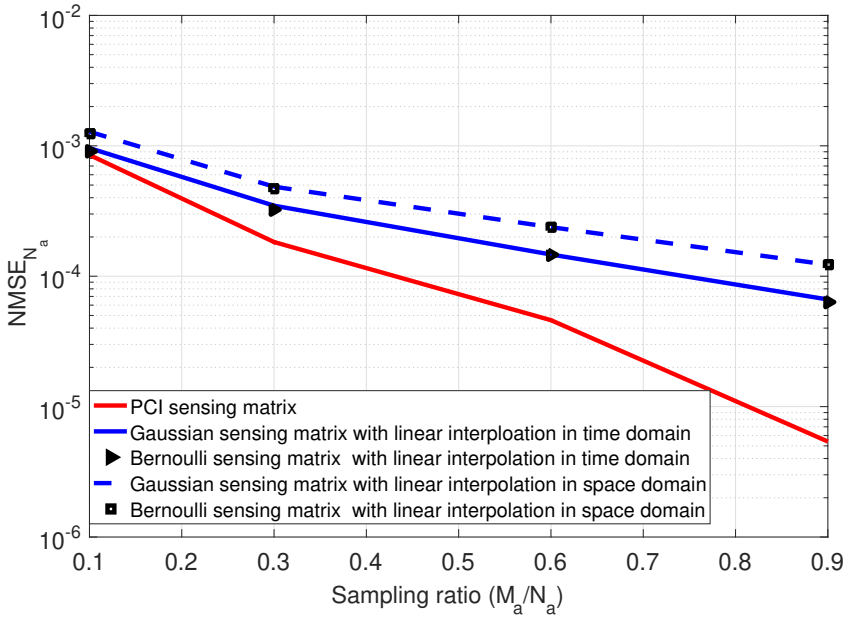

Figure 2.7: NMSE_{N_a} obtained with PCI, Gaussian, and Bernoulli sensing matrices by exploiting both space and time correlation.

- Another class of sparse matrix, say $\mathbf{\Phi}_2$, is introduced in [53], in which each entry can be +1, -1 and 0 with the some probability. The considered probability mass function is given below

$$Pr(\Phi_2(i,j) = w) = \begin{cases} \frac{1}{3} & w \in \{0, 1, -1\} \\ 0 & \text{otherwise,} \end{cases} \quad \forall i, j$$

where $\Phi_2(i,j)$ is the element of the matrix $\mathbf{\Phi}_2$.

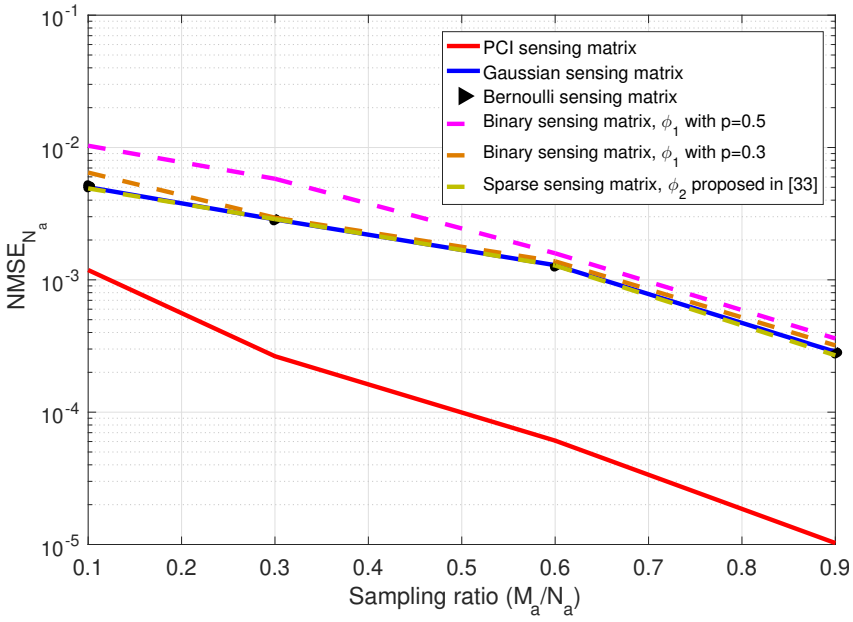

Figure 2.8: NMSE_{N_a} obtained with various sensing matrices and DCT sparsifying domain.

The DCT domain has been considered as the sparsifying domain. From Fig. 2.8, we can observe binary matrix with $p = 0.5$ is performing worse than conventional Gaussian and Bernoulli matrices, whereas, the performance of binary matrix with $p = 0.3$ and the sparse matrix proposed in [53] have the almost similar performance with the conventional Gaussian and Bernoulli matrices. However, the proposed PCI sensing matrix based reconstruction is outperforming all sensing matrices with considerable difference.

2.4 Discussion

As mentioned above, the proposed PCI-CS framework is self-sufficient in recovering the missing entries from the original data, and the detailed analysis has been provided subsequently in Chapter 3. However, a few observations are mentioned below:

- Fig. 2.9 shows the original data (with missing entries), and the data recovered data using all three sensing matrices (i.e., Gaussian, Bernoulli and PCI). There were $N_T - N_a = 6593$ missing entries in the original data set which could be recovered successfully only with PCI sensing matrix as a complimentary by-product.

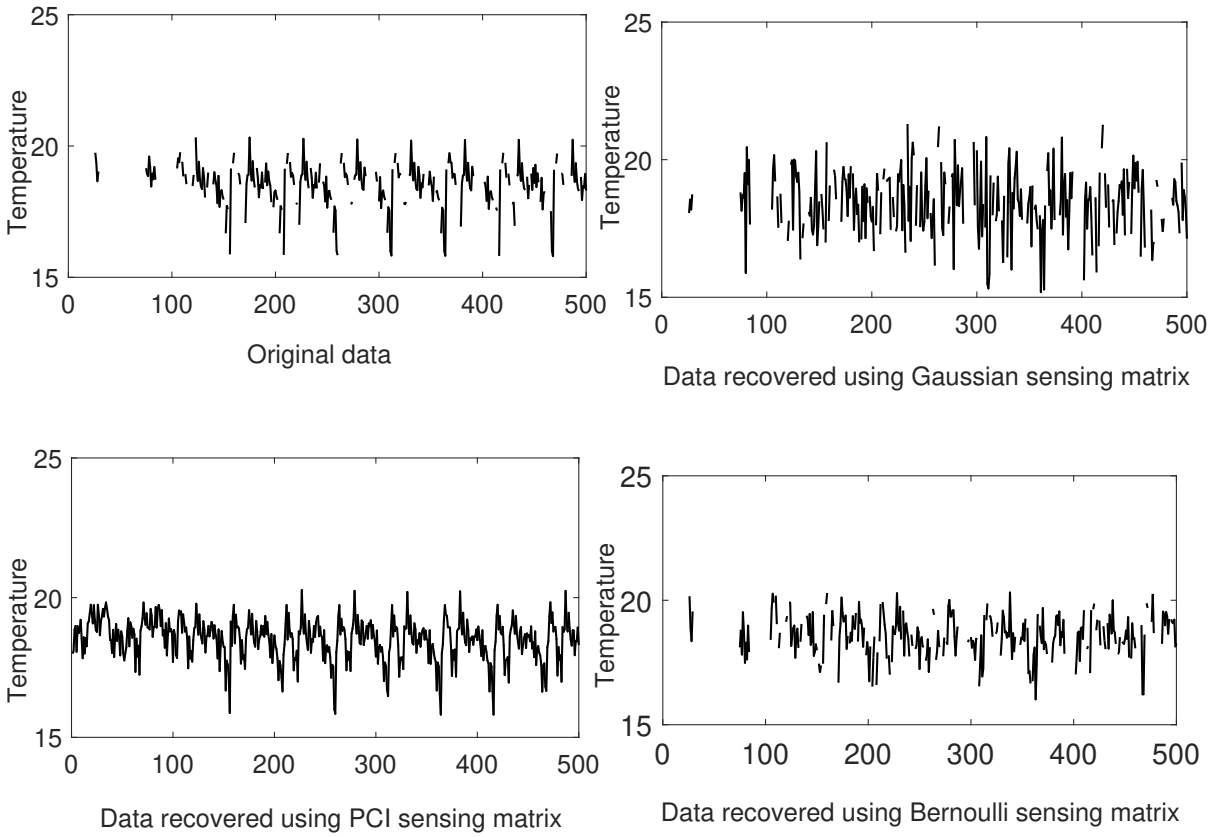

Figure 2.9: Recovery of missing values from the original data, a by-product of PCI sensing matrix.

- Consider Fig. 2.4 to evaluate the performance of PCI sensing matrix in context of missing data recovery. It can be observed that NMSE of approximately 10^{-3}, 10^{-4} and 10^{-5} is obtained with PCI sensing matrix at the sampling ratios of 0.1, 0.5 and 0.9, which is equivalent to the case when 90%, 50% and 10% data are missing, respectively.

Chapter 3

Robust two-stage algorithm for Missing data recovery in WSN

In recent years, wireless sensor networks (WSNs) are being widely used for both critical as well as non-critical applications. The data collected by sensor nodes may be corrupted or distorted due to hardware impairments and severe environmental conditions such as deep fading. For critical applications such as detection of the forest fire, ocean currents, chemical pills and earthquake, it is essential to obtain complete data accurately at the fusion centre (FC) for taking an appropriate decision. Previously, to recover the missing and corrupted data in WSN, various interpolation techniques such as K-nearest neighbours (KNN) [55], and Delaunay Triangulation (DT) [56] have been used. However, when missing entries are large, the accuracy of the above techniques are deemed insufficient. In addition, missing values are effectively recovered by using the low-rank constraint in various applications such as recommender systems, image inpainting and WSN, since most of the real-world signals are low rank.

3.1 Background

Consider a WSN matrix $\mathbf{X}_{N\times T}$, where N is the number of sensor nodes and T is the number of time stamps at which data is collected. The received incomplete matrix can be written as

$$\mathbf{Y} = \mathbf{B} \bullet \mathbf{X}, \tag{3.1}$$

where '$\bullet$' denotes element wise multiplication and $\mathbf{B}$ is a binary index matrix such that $B(i,j) = 1$, if $X(i,j)$ is present and is 0 if $X(i,j)$ is missing. If $\mathbf{X}$ is low-rank, it can be recovered by solving the following convex optimization program

$$\min_{\mathbf{X}} \ \text{rank}(\mathbf{X}) \quad \text{s.t} \quad \mathbf{Y} = \mathbf{B} \bullet \mathbf{X}. \tag{3.2}$$

However, minimizing rank of the data is an NP-hard problem. Hence, instead of minimizing the rank of $\mathbf{X}$, sum of the singular values of $\mathbf{X}$ is minimized using the following formulation

$$\min_{\mathbf{X}} ||\mathbf{X}||_* \quad \text{s.t.} \quad \mathbf{Y} = \mathbf{B} \bullet \mathbf{X}. \tag{3.3}$$

where $||\mathbf{X}||_*$ is the nuclear norm of $\mathbf{X}$. (3.3) can be solved by *singular value thresholding (SVT)* algorithm [26]. *Matrix factorization* is also one of the famous techniques for matrix completion (MC) [57], if rank of $\mathbf{X}$ (say r) is known. In such a scenario, (3.2) can be solved as:

$$\min_{\mathbf{U},\mathbf{V}} (||\mathbf{U}||_F^2 + ||\mathbf{V}'||_F^2) \ \text{ s.t.} \quad \mathbf{Y} = \mathbf{B} \bullet (\mathbf{U}\mathbf{V}'). \tag{3.4}$$

Here, we need to find matrices $\mathbf{U}$ and $\mathbf{V}$ such that $\mathbf{X} = \mathbf{U}\mathbf{V}'$. The dimensions of $\mathbf{U}$ and $\mathbf{V}$ are $N \times r$ and $T \times r$, respectively. It may be noted that the rank of an incomplete matrix can not be determined, and hence, a low-rank matrix fitting (LMaFit) algorithm [34] has been presented for MC, in which r is dynamically adjusted. Moreover, in [28], spatial and temporal correlation along with the rank constraint have been exploited to recover the missing data in WSN by solving following optimization framework

$$\min_{\mathbf{U},\mathbf{V}}(||\mathbf{B} \bullet (\mathbf{U}\mathbf{V}') - \mathbf{Y}||_F^2 + \lambda(||\mathbf{U}||_F^2 + ||\mathbf{V}'||_F^2) + ||\mathbf{H}\mathbf{U}\mathbf{V}'||_F^2 + ||\mathbf{U}\mathbf{V}'\mathbf{T}||_F^2), \quad (3.5)$$

where λ is the Lagrange multiplier. $\mathbf{T}$ and $\mathbf{H}$ matrices are used to exploit the temporal and spatial correlation, respectively. This method requires both rank and topology of the data for correct estimation of missing values, which is not known in practical scenario for incomplete data matrix. Furthermore, robust principal component analysis (RPCA) [58] is also one of the known method used for MC in the noisy environment, in which the data matrix $\mathbf{X}$ is assumed to be the sum of a low rank matrix ($\mathbf{L}$) and a sparse matrix ($\mathbf{S}$). Hence, along with minimizing the nuclear norm of $\mathbf{L}$, the algorithm also minimizes the l_1 norm of $\mathbf{S}$ as shown below

$$\min_{\mathbf{L},\mathbf{S}}(||\mathbf{B} \bullet (\mathbf{L} + \mathbf{S}) - \mathbf{Y}||_F^2 + \lambda_1||\mathbf{L}||_* + \lambda_2||\mathbf{S}||_1. \quad (3.6)$$

Several fast and efficient algorithms have been proposed to solve RPCA problem [59, 60]. In [59], Robust PCA has been solved via gradient descent method. This method is called as RPCA-GD.

3.2 Proposed methods

In this section, we will discuss three different proposed methods to recover the missing data values in the context of WSN, which are listed below. It is to be noted that all the proposed algorithms outperform various matrix completion algorithms and do not require any prior knowledge of the data, such as the rank or the network topology.

- ***PCI-MDR***: In continuation with Section 2.4 of Chapter 2, we have proposed a two-stage PCI based missing data recovery (MDR) method, named as *PCI-MDR*. The first stage of this algorithm utilizes PCI-CS to recover the entire data, and the second stage de-noise the data by exploiting the low-rank nature while minimizing the nuclear norm of the WSN dataset. This algorithm has been discussed in details in Section 3.2.1.

  Some of the open questions of the proposed *PCI-MDR* algorithm are

  1. Can we use double DCT sparsity in context of matrix completion framework (3.1), instead of PCI-CS to recover the data?
  2. Can we improve the de-noising stage (second stage) by exploiting more properties of the recovered data from the first stage?

  In order to answer the above questions, two algorithms employing "*two stage matrix completion (TS-MC)*" for WSN have been proposed.

- ***TS-MC-1***: The first stage of this algorithm performs matrix completion by minimizing the DCT coefficients (named as *MC-DCT*) jointly in both

spatial and temporal domain and the second stage de-noises the data in the matrix factorization framework.

- ***TS-MC-2***: The first stage of this algorithm utilizes PCI-CS to recover the sparsest solution and the rank of the data from the partial available information, which are jointly utilized in the second stage to de-noise the data in a matrix factorization framework. Hence, this algorithm also named as *PCI-MF*. Both TS-MC methods have been discussed in details in Section 3.2.2.

3.2.1 PCI-MDR algorithm

The received incomplete WSN matrix (3.1) can also be written as

$$\mathbf{y} = \mathbf{\Phi x}, \tag{3.7}$$

where $\mathbf{x} = \mathbf{X}(:)$ is a vector of length NT. Further, $\mathbf{\Phi}$ is the matrix of size $M \times NT$ with M as the number of available entries of full data $\mathbf{x}$. Here, each row of $\mathbf{\Phi}$ contains single '1' at the position corresponding to the data samples available in $\mathbf{x}$. This implies vector $\mathbf{y}$ contains the available M entries of $\mathbf{x}$. This particular non-square matrix $\mathbf{\Phi}$ with a single '1' in every column and row is the PCI matrix. Since the WSN matrix is sparse in DCT domain due to spatial and temporal smoothness, (refer Section 2.3), the vector $\mathbf{x}$, and hence $\mathbf{X}$ can be recovered from $\mathbf{y}$ as shown in Section 2.3.1. Therefore, the PCI based CS framework (PCI-CS) proposed in Chapter 2 can also be used to recover the missing data

values. However, in presence of noise, the smoothness in the data is affected, which in turn impacts the level of sparsity which deteriorates the performance of the algorithm. Since, the WSN data is also low-rank, a de-noising framework with low-rank constraint is subsequently applied on the matrix recovered using PCI-CS, denoted as $\hat{\mathbf{X}}$, as shown below

$$\tilde{\mathbf{X}} = ||\hat{\mathbf{X}} - \mathbf{X}||_F^2 + \lambda_l ||\mathbf{X}||_*, \tag{3.8}$$

where λ_l is the regularization parameter.

3.2.2 TS-MC algorithms

This section provides the detailed description of *TS-MC-1* and *TS-MC-2* algorithms. The first stage of both TS-MC algorithms, exploited the DCT sparsifying domain, as the WSN signal is sparse in the DCT domain 2.3. However, the implementation of both algorithms is different. In the first stage of *TS-MC-1*, matrix completion is performed by minimizing the DCT coefficients jointly in both the spatial and temporal domain. However, the first stage of *TS-MC-2* solves the missing data recovery problem by using PCI-CS framework. The first stage of both TS-MC has been discussed subsequently in Section 3.2.2.1.

It is to be noted that the second stage of both the algorithms is the same and discussed in Section 3.2.3. In this stage, the recovered data from the first stage is further de-noised using matrix factorization framework. The rank required for matrix factorization can be estimated from the data recovered from the first

stage.

3.2.2.1 First stage of TS-MC algorithms

The first stage of TS-MC-1 and TS-MC-2 has been discussed in the following subsections 3.2.2.2 and 3.2.2.2, respectively.

3.2.2.2 First stage of *TS-MC-1*

In this method, the matrix completion problem is formulated as

$$\min_{\mathbf{X}} ||\mathbf{Y} - \mathbf{B} \bullet \mathbf{X}||_F^2 + \lambda_1 ||\mathbf{D}_1 \mathbf{X} \mathbf{D}_2||_1, \tag{3.9}$$

where $\mathbf{D}_1$ and $\mathbf{D}_2$ are the DCT matrices of size $N \times N$ and $T \times T$, respectively. The constraint $||\mathbf{D}_1 \mathbf{X} \mathbf{D}_2||_1$ used in (3.9) enforces the double DCT sparsity as data is slowly-varying in both spatial and temporal domains. Further, $\lambda_1 \in \mathbb{R}$ is the regularization parameter that controls the trade-off between data accuracy and the sparsity level. A proxy variable $\mathbf{W}$ is introduced to rewrite (3.9) as

$$\min_{\mathbf{X},\mathbf{W}} ||\mathbf{Y} - \mathbf{B} \bullet \mathbf{X}||_F^2 + \lambda_1 ||\mathbf{W}||_1 + \lambda_2 ||\mathbf{W} - \mathbf{D}_1 \mathbf{X} \mathbf{D}_2||_F^2, \tag{3.10}$$

where λ_2 is the controlling parameter to control the degree of equality between the original term and the proxy variable. For small value of λ_1, the equality constraint is relaxed and for high value of λ_1, the constraint is enforced. The above problem (3.10) can be divided into the following sub-problems by using

the alternating direction method of multipliers (ADMM):

$$\mathrm{P}_1 : \min_{\mathbf{W}} ||\mathbf{W} - \mathbf{D}_1\mathbf{X}\mathbf{D}_2||_F^2 + \lambda_a||\mathbf{W}||_1 \quad \left(\because \lambda_a = \frac{\lambda_1}{\lambda_2}\right),$$
$$\mathrm{P}_2 : \min_{\mathbf{X}} ||\mathbf{Y} - \mathbf{B} \bullet \mathbf{X}||_F^2 + \lambda_2||\mathbf{W} - \mathbf{D}_1\mathbf{X}\mathbf{D}_2||_F^2 \tag{3.11}$$

P_1 can be solved using soft-thresholding [61] and P_2 is a simple least squares problem.

Algorithm 1 *TS-MC-1*

Input: $\mathbf{B}$, $\mathbf{Y}$, $\mathbf{D}_1$, $\mathbf{D}_2$, $\mathbf{X}_{int}$, λ_a, μ, max_{iter1}, max_{iter2}
Initializing: $\mathbf{X} = \mathbf{X}_{int}$
Obtain $\mathbf{B}_c$ such that $B_c(i,j) = \begin{cases} 1 & \text{if } B(i,j) = 0 \\ 0 & \text{if } B(i,j) = 1 \end{cases}$
for $k_1 = 1 : max_{iter1}$
  $\mathbf{W} = sgn(\mathbf{D}_1\mathbf{X}\mathbf{D}_2)\max(0, |\mathbf{D}_1\mathbf{X}\mathbf{D}_2| - 0.5\lambda_a)$ [1]
  $\mathbf{X} = \mathbf{D}_1^T\mathbf{W}\mathbf{D}_2^T$
  $\mathbf{X} = \mathbf{Y} + \mathbf{B}_c \bullet \mathbf{X}$
end
$\begin{bmatrix}\mathbf{U} & \mathbf{D} & \mathbf{V}\end{bmatrix} = svd(\mathbf{X})$; svd is the singular value decomposition.
$\mathbf{d} = diag(\mathbf{D})$; $diag$ picks the diagonal elements.
r = number of highest values in $\mathbf{d}$
for $k_2 = 1 : max_{iter2}$
  $\mathbf{U} \leftarrow \min_{\mathbf{U}} \left\| \begin{bmatrix}\hat{\mathbf{X}} & \mathbf{0}_{n\times r}\end{bmatrix} - \mathbf{U}\begin{bmatrix}\mathbf{V} & \sqrt{\mu}\mathbf{I}_r\end{bmatrix} \right\|_F^2$
  $\mathbf{V} \leftarrow \min_{\mathbf{V}} \left\| \begin{bmatrix}\hat{\mathbf{X}} \\ \mathbf{0}_{r\times t}\end{bmatrix} - \begin{bmatrix}\mathbf{U} \\ \sqrt{\mu}\mathbf{I}_r\end{bmatrix}\mathbf{V} \right\|_F^2$
end
X=UV
Output: $\mathbf{X}$

3.2.2.3 First stage of *TS-MC-2*

In this method, the problem of missing data recovery is formulated as a CS problem and solved using PCI-CS framework, the same as in the first stage of PCI MDR algorithm. Refer to Section 3.2.1. Compared to *TS-MC-1*, this

[1] $sgn = \begin{cases} -1 & \text{if } x < 0 \\ 0 & \text{if } x = 0 \\ 1 & \text{if } x > 0 \end{cases}$

method also carries out de-noising of data.

3.2.3 Second stage of TS-MC algorithms

The data recovered from the first stage ($\hat{\mathbf{X}}$) is de-noised in the second stage using matrix factorization such as $\hat{\mathbf{X}} = \mathbf{UV}$. The dimension of $\mathbf{U}$ and $\mathbf{V}$ are chosen to be $n \times r$ and $r \times t$, respectively, where r is the rank of the data that can be estimated from $\hat{\mathbf{X}}$. The problem can be formulated as

$$\min_{\mathbf{U},\mathbf{V}} ||\hat{\mathbf{X}} - \mathbf{UV}||_F^2 + \mu||\mathbf{U}||_F^2 + \mu||\mathbf{V}||_F^2. \tag{3.12}$$

The problem in (3.12) can be divided into two sub-problems using ADMM as

$$\begin{aligned} \mathrm{P}_3 : \mathbf{U} &\leftarrow \min_{\mathbf{U}} ||\hat{\mathbf{X}} - \mathbf{UV}||_F^2 + \mu||\mathbf{U}||_F^2, \\ \mathrm{P}_4 : \mathbf{V} &\leftarrow \min_{\mathbf{V}} ||\hat{\mathbf{X}} - \mathbf{UV}||_F^2 + \mu||\mathbf{V}||_F^2. \end{aligned} \tag{3.13}$$

The above sub-problems can be re-written as

$$\begin{aligned} \mathrm{P}_3 : \mathbf{U} &\leftarrow \min_{\mathbf{U}} \left\| \begin{bmatrix} \hat{\mathbf{X}} & \mathbf{0}_{n\times r} \end{bmatrix} - \mathbf{U} \begin{bmatrix} \mathbf{V} & \sqrt{\mu}\mathbf{I}_r \end{bmatrix} \right\|_F^2 \\ \mathrm{P}_4 : \mathbf{V} &\leftarrow \min_{\mathbf{V}} \left\| \begin{bmatrix} \hat{\mathbf{X}} \\ \mathbf{0}_{r\times t} \end{bmatrix} - \begin{bmatrix} \mathbf{U} \\ \sqrt{\mu}\mathbf{I}_r \end{bmatrix} \mathbf{V} \right\|_F^2. \end{aligned} \tag{3.14}$$

The above sub-problems are the simple least squares problems. Further, the original WSN matrix $\mathbf{X}$ can be recovered as $\tilde{\mathbf{X}} = \mathbf{UV}$.

The algorithmic steps of *TS-MC-1* and *TS-MC-2* algorithm have been pro-

vided in Algorithm 1 and Algorithm 2, respectively.

Algorithm 2 *TS-MC-2*

Input: $\mathbf{\Phi}$, $\mathbf{y}$, $\mathbf{D}_1$, $\mathbf{D}_2$, $\mathbf{x}_{int}$, n, t, μ, λ_3, max_{iter1}, max_{iter2}
Initializing: $\mathbf{x} = \mathbf{x}_{int}$
$\mathbf{H} = \mathbf{\Phi}(\mathbf{D}_2 \otimes \mathbf{D}_1^T)$
$\alpha = \max(eig(\mathbf{H}^T\mathbf{H}))$
for $k_1 = 1 : max_{iter1}$
    $\mathbf{x} = sgn(\mathbf{x} + \frac{1}{\alpha}\mathbf{H}^T\mathbf{y} - \mathbf{H}\mathbf{x}) \max(0, |\mathbf{H}^T\mathbf{y} - \mathbf{H}\mathbf{x}| - \frac{\lambda_3}{2\alpha})^1$
end
$\mathbf{X}$ = reshape($\mathbf{x}$, (n, t)); reshape converts the vector $\mathbf{x}$ into a matrix of size $n \times t$.
$\begin{bmatrix}\mathbf{U} & \mathbf{D} & \mathbf{V}\end{bmatrix} = svd(\mathbf{X})$; svd is the singular value decomposition.
$\mathbf{d} = diag(\mathbf{D})$; $diag$ picks the diagonal elements.
r = number of highest values in $\mathbf{d}$
for $k_2 = 1 : max_{iter2}$
    $\mathbf{U} \leftarrow \min_{\mathbf{U}} \left\| \begin{bmatrix}\hat{\mathbf{X}} & \mathbf{0}_{n\times r}\end{bmatrix} - \mathbf{U}\begin{bmatrix}\mathbf{V} & \sqrt{\mu}\mathbf{I}_r\end{bmatrix} \right\|_F^2$
    $\mathbf{V} \leftarrow \min_{\mathbf{V}} \left\| \begin{bmatrix}\hat{\mathbf{X}} \\ \mathbf{0}_{r\times t}\end{bmatrix} - \begin{bmatrix}\mathbf{U} \\ \sqrt{\mu}\mathbf{I}_r\end{bmatrix}\mathbf{V} \right\|_F^2$
end
X=UV
Output: **X**

3.3 Complexity

The complexity of all three proposed algorithms are provided below: ***PCI-MDR***: The complexity of the first and the second stage of the *PCI-MDR* algorithm is $\mathcal{O}(MNT)$ and $\mathcal{O}(N^2T)$ per iteration, respectively. Therefore, the overall complexity of the proposed algorithm will be $\mathcal{O}(MNT+N^2T) \approx \mathcal{O}(MNT)$ per iteration.

TS-MC-1: The complexity of the first and the second stage of the *TS-MC-1* algorithm is $\mathcal{O}(NT)$ and $\mathcal{O}(NrT)$ per iteration, respectively. Therefore, the overall complexity of the proposed algorithm will be $\mathcal{O}(NT + NrT) \approx \mathcal{O}(NrT)$ per iteration.

TS-MC-2: The complexity of the first and the second stage of the *TS-MC-2* al-

Table 3.1: Complexity comparison of all three proposed methods

	PCI-MDR	***TS-MC-1***	***TS-MC-2*** **(PCI-MF)**
First stage	PCI-CS $\mathcal{O}(MNT)$	MC-DCT $\mathcal{O}(NT)$	PCI-CS $\mathcal{O}(MNT)$
Second stage	SVT $\mathcal{O}(N^2T)$	MF $\mathcal{O}(NrT)$	MF $\mathcal{O}(NrT)$
Total complexity	$\mathcal{O}(MNT)$	$\mathcal{O}(NrT)$	$\mathcal{O}(MNT)$

gorithm is $\mathcal{O}(MNT)$ and $\mathcal{O}(NrT)$ per iteration, respectively. Therefore, the overall complexity of the proposed algorithm will be $\mathcal{O}(MNT + NrT) \approx \mathcal{O}(MNT)$ per iteration.

The complexity of *TS-MC-1* is same as of the matrix factorization $\mathcal{O}(NrT)$ [57] and a bit smaller than the complexity of *PCI-MDR* and *TS-MC-2*. However, the complexity of these two algorithms (*PCI-MDR* and *TS-MC-2*) is dominated by ISTA and quite higher even with the complexity of SVT ($\mathcal{O}(n^2t)$) [62]. Although it should be observed that at massive data loss, M will decrease, and hence complexity will also decrease. In addition to the above, the computations will be performed at the fusion centre (FC), which is generally equipped with powerful processors. Furthermore, algorithms like Fast ISTA (FISTA) [50] also exist in the literature, which reduces the complexity of ISTA and hence, the complexity of these algorithms can be further reduced.

3.4 Simulation Results

This section compares the performance of all three proposed algorithms with various recent and state-of-the-art methods in the context of missing data recov-

ery. The simulation results for *PCI-MDR* have been discussed in Section 3.4.1, whereas the simulation results for TS-MC algorithms have been discussed in Section 3.4.2.

3.4.1 PCI-MDR algorithm

In this section, we have computed the performance of the proposed PCI-MDR method for missing data recovery in both absence as well as in the presence of noise. The results have been compared with matrix factorization [57] and SVT [26] algorithms on the real data set of temperature taken from **Intel Lab** [1]. The data from 53 sensor nodes at every minute has been considered for 200 minutes in the simulation Hence, $N = 53$ and $T = 200$. It is to be noted that out of 10600 entries (53×200), 2699 entries are missing i.e., 25.4623% of data is not available. Since the ground truth of the missing data mentioned above is not available, we manually removed m_2 entries randomly, in addition to the values already missing in the original dataset i.e., m_1. We designed the PCI matrix to recover the original m_1 missing entries and also the simulated m_2 missing entries, therefore the overall missing data will be $N - M = m_1 + m_2$. The data loss percentage is calculated as $\frac{m_2}{N-m_1} \times 100\%$. Further, NMSE is given by $\frac{||\mathbf{x}_{m_2} - \hat{\mathbf{x}}_{m_2}||_2^2}{||\mathbf{x}_{m_2}||_2^2}$, where $\hat{\mathbf{x}}_{m_2}$ is the recovered data at the simulated missing positions (i.e., m_2) and $\mathbf{x}_{m_2}$ is the ground truth available at m_2 positions.

All the data points of $\mathbf{x}$ i.e., N has been reconstructed, however, for computing the performance of the algorithm, the performance is calculated only at the simulated missing values, i.e., m_2 since the ground truth is available at these

positions only. If the data at the simulated missing positions are recovered with good accuracy, it will indicate that the actual missing data must have also been recovered with good accuracy. Furthermore, in order to create the noisy data, additive Gaussian noise is added to the dataset such that the average signal-to-noise (SNR) power ratio is 10 dB.

Fig. 3.1 and 3.2 shows the NMSE of data recovered at simulated missing positions as a function of data loss percentage in the absence and presence of noise, respectively. From Fig. 3.1, we observe that *a)* the reconstruction performance of the PCI-MDR method is better in the time domain as compared to the spatial domain. This is because the data in the time domain is smoother than the spatial domain and hence will be more sparse in the DCT domain, this is also evident from Fig. 2.3; *b)* PCI-MDR is performing better than both matrix factorization [57] and SVT [26] methods. It may be noted that the matrix factorization technique also requires the rank of the data, which is generally unavailable for the realistic scenario. Therefore, we have computed matrix factorization algorithm for two values of rank, r = 1 and 2. Further, it can be observed that as the data loss percentage increases, the performance of the proposed method compared to existing methods also increases.; *c)* double sparsity can be exploited using both spatial and temporal domain together to further improve the performance of PCI-MDR.; and *d)* at massive data loss of 90%, the proposed method is still giving NMSE of 4.0445×10^{-5}, however, the matrix factorization with $r = 1$ has NMSE of 0.019348, and hence providing ~ 25 dB improvement.

The second stage of de-noising in PCI-MDR method (3.8) provides the sig-

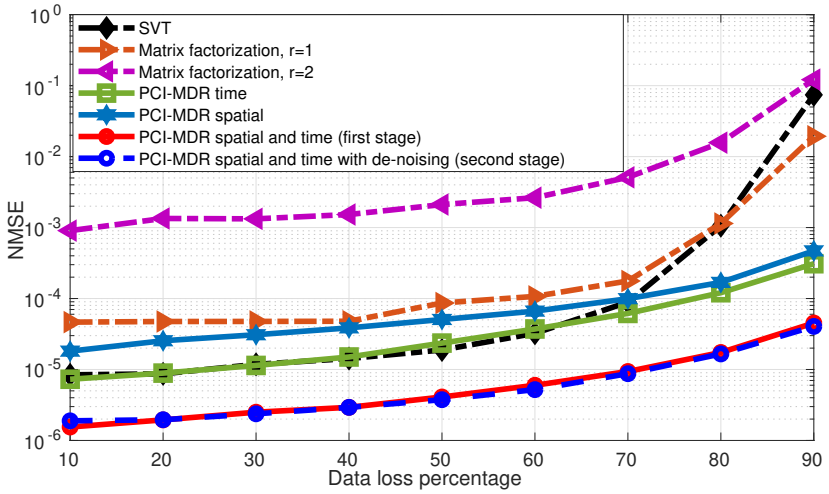

Figure 3.1: NMSE versus data loss for WSN Intel Lab data in the absence of noise.

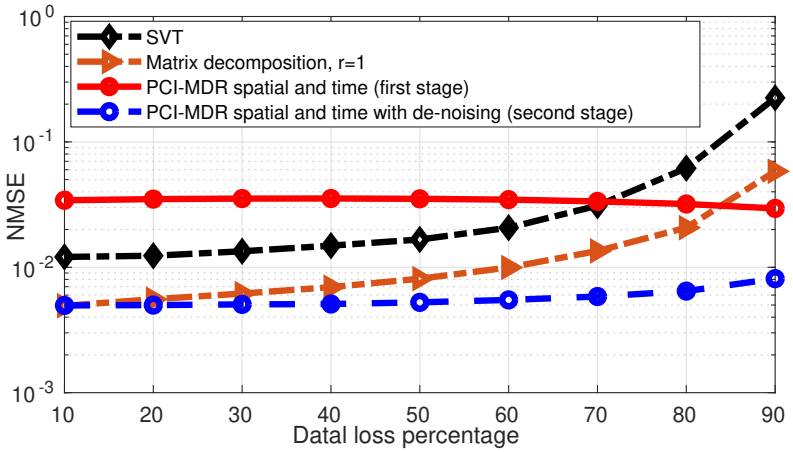

Figure 3.2: NMSE versus data loss for WSN Intel Lab data in the presence of noise with SNR = 10 dB.

nificant improvement in the case of noisy data as shown in Fig. 3.2 but no improvement for noiseless data as shown in Fig. 3.1. This is because in the presence of noise, the smoothness of the real data gets affected, therefore exploiting low-rank constraint at the second stage provides an improvement in the reconstruction performance. However, in the absence of noise, the PCI and DCT based CS framework (first stage) is sufficient in recovering the missing data accurately, and hence no additional constraint such as low-rank is required. Compared to the existing matrix factorization algorithm with $r = 1$, the proposed method provides 8.6 dB improvement in the presence of noise.

3.4.2 TS-MC algorithms

The performance of *PCI-MDR* can be further improved by using proposed *TS-MC-1* and *TS-MC-2* algorithms. Consider Fig.3.3, which compares all three proposed algorithms and also various other matrix completion algorithms such as SVT [26], LMaFit [34], OptSpace [63] and RPCA-GD [59]. From the obtained

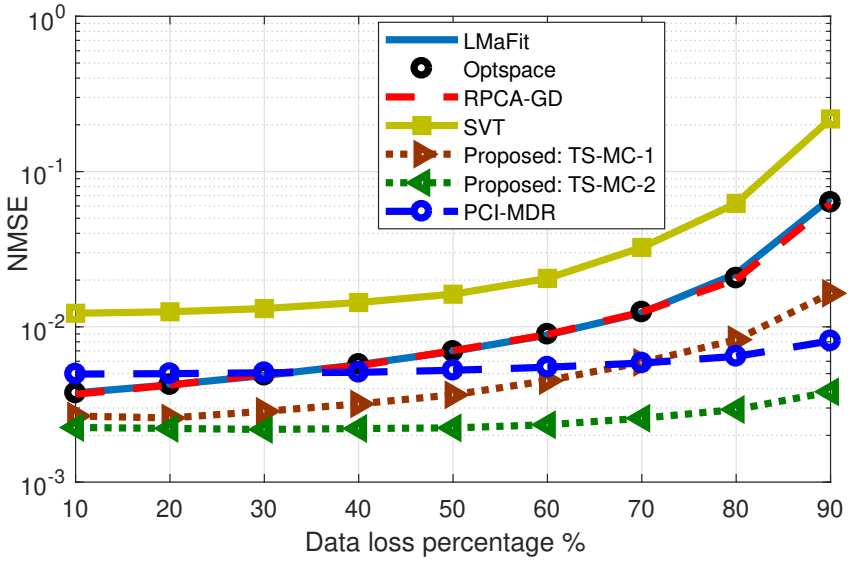

Figure 3.3: NMSE versus data loss for WSN Intel Lab data in the presence of noise with SNR = 10dB.

results, it is observed that both proposed algorithms of TS-MC outperforming the various matrix completion algorithms as well as *PCI-MDR*. Furthermore, the performance of *TS-MC-2* is much better than *TS-MC-1* at high data loss. From Fig. 3.5, we observe that at 90% data loss, *TS-MC-1* is providing around 6 dB improvement, while *TS-MC-2* is providing around 12.5 dB improvement as compared to LMaFit, Optspace and RPCA-GD. Therefore, at higher data losses, the proposed algorithm is performing very well, and hence in Fig. 3.4, we have plotted the NMSE with respect to SNR for 90% data loss. The comparison has also been shown on humidity dataset of the Intel lab [1] in Fig. 3.5.

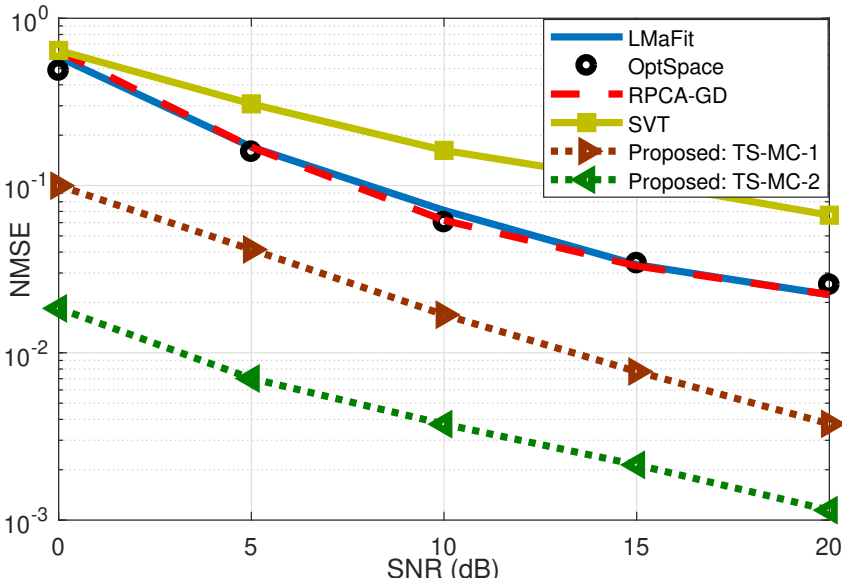

Figure 3.4: NMSE against SNR at 90% data loss for temperature dataset taken from Intel lab

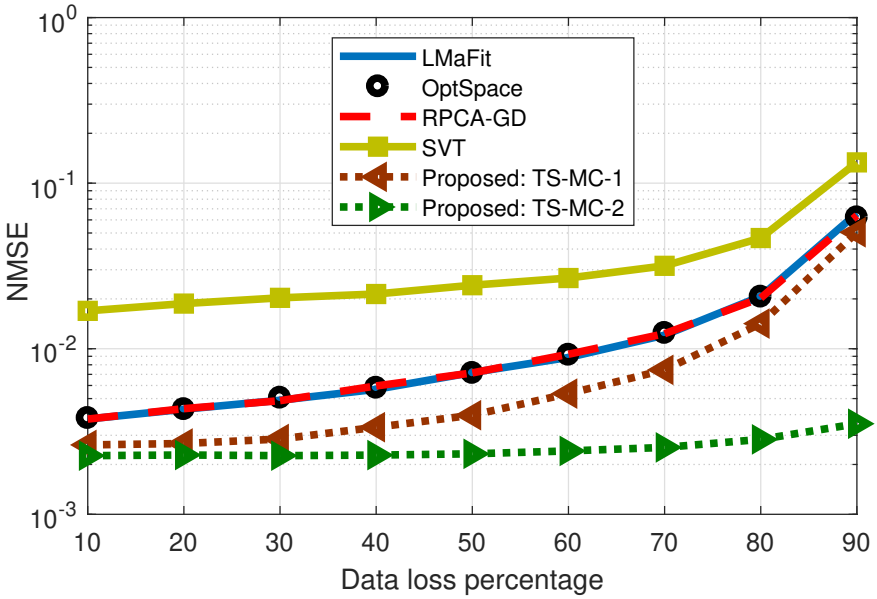

Figure 3.5: NMSE against data loss percentage at SNR = 10 dB for Intel Lab humidity dataset

For further verification, we have also compared the algorithms using the dataset of another lab (data sensing lab [64]). In this dataset, $N = 38$ sensor nodes are present and similar to above $T = 200$ timestamps have been taken. Further, in this dataset, 9.16% of entries are not available, as $NT = 7600$ and

$N - m_1 = 6904$. In Fig. 3.6, NMSE for m_2 entries has been plotted against data loss percentage. It can be observed that the proposed algorithms are consistently outperforming the conventional MC algorithms on this dataset as well.

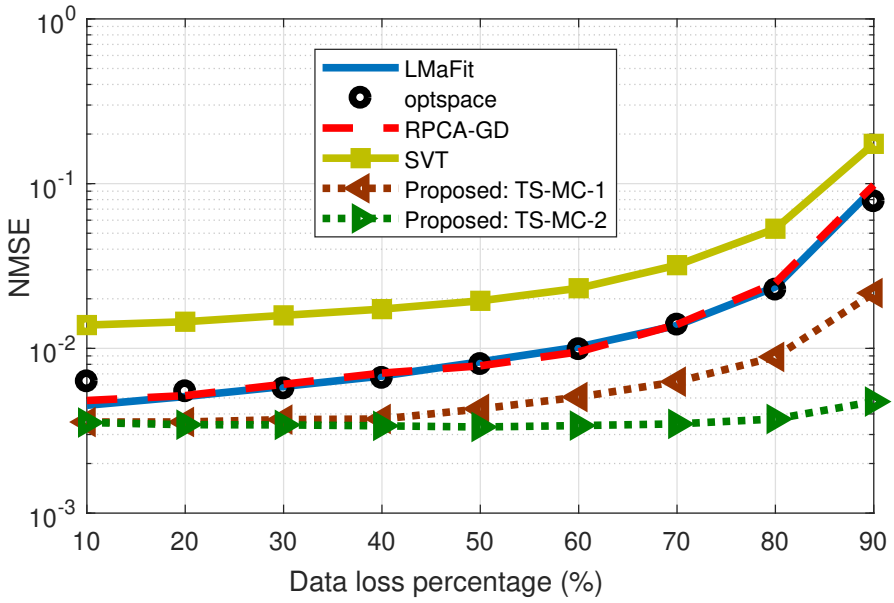

Figure 3.6: NMSE against data loss percentage at SNR = 10 dB for temperature dataset taken from Data sensing lab

3.5 Discussion

We have observed that the proposed *TS-MC-2* (also known as PCI-MF), which is exploiting PCI-CS to recover the incomplete data in the first stage and then de-noising the recovered data in the second stage using matrix factorization framework by estimating the rank from the first stage is the best performing algorithm. In this chapter, this algorithm has been used in the WSN application. However, the proposed algorithm can be applied in various other applications, if the data is sparse in a domain such that the sparsifying domain is mutually incoherent with PCI matrix, for instance, DCT and DFT, and also the low-rank

in any domain.

In the subsequent chapter, *TS-MC-2*/PCI-MF has been modified to recover the channel coefficients in mmWave massive MIMO wireless system. This is due to the fact that mmWave channel forms a sparsity pattern in the DFT domain, and further the channel coefficients also has various dependencies which reduce the rank of the channel matrix. This also implies the proposed algorithm is not only designed for a correlated data such as WSN, it will equally perform even for a random data such as wireless channel.

Chapter 4

PCI-MF: Partial canonical identity and Matrix factorization framework for channel estimation in mmWave Massive MIMO systems

4.1 Introduction

To facilitate the vision of fifth-generation (5G) cellular standard, numerous advanced technologies such as shrinking the cell's size, and advanced multiple-input-multiple-output (MIMO) have been proposed in the literature [65, 66]. However, the existing microwave band (< 6 GHz) is mostly occupied and may not be able to meet future demands even after employing these technologies [67, 68]. Therefore, there is a need to move to extremely high frequency (EHF) band (30-300 GHz), also known as millimetre wave (mmWave) band, which has the capability of providing data rates in giga-bits-per-second (Gbps)

[29, 30]. The transmission at such high frequency comes at the expense of significant path attenuation [69]. Therefore, to overcome the propagation losses at mmWave frequencies, directional beamforming between transmitter and receiver is employed by using multiple antennas at both transmitter as well as receiver [70, 71]. Fortunately, due to shorter wavelength of mmWave communication system, more antennas can be placed together in a small area because the separation required between consecutive antennas is around half of the signal's wavelength at both the transmitter as well as the receiver [72]. However, to provide sufficient beamforming gain, a well-aligned narrow beam between transmitter and receiver is required, which requires perfect channel state information (CSI). Since mmWave massive MIMO system utilizes multiple antennas at both transmitter and receiver, estimation of channel coefficients between every pair increases the overhead considerably.

To reduce the overhead, the problem of channel estimation in mmWave massive MIMO is formulated as either beam-alignment problem or compressive sensing (CS) problem. In beam alignment, the transmitter and receiver search for the best beam pair, which increases the feedback overhead [31–33]. However, the CS problem exploits the sparse behaviour of mmWave channel [73–75] and does not require feedback. Consequently, a few compressive measurements are obtained to recover the entire CSI by using sparse recovery methods, such as orthogonal matching pursuit (OMP) [76]. Apart from CS based techniques that exploit the sparse behaviour of mmWave channel, [77, 78] have exploited the low-rank property of mmWave channel to recover the CSI. In [77, 78] low-rank

tensor factorization methods have been employed, which improve the accuracy and reduce the complexity as compared to the sparsity-based CS techniques. Recently, researchers have exploited both low-rank as well as sparse behaviour of mmWave channel to considerably improve the accuracy of the estimated CSI [20, 21]. In [20], a two-stage method has been developed for mmWave channel estimation, where the low-rank property in a matrix completion framework [62] and the sparse property in a sparse recovery framework have been used in two consecutive stages. Unlike above, in [21] both low-rank as well as the sparse property of mmWave channel matrix have been exploited jointly to obtain the entire CSI from a few channel coefficients. It uses an alternating direction method of multipliers (ADMM) for jointly exploiting the low-rank and sparse properties in a matrix completion framework. Simulations show considerable improvement in channel estimation in [21] as compared to [20].

The performance of existing methods is still restricted because these methods are not leveraging the known properties of mmWave massive MIMO channel matrix judiciously. In this chapter, the proposed PCI-MF has been used to recover complete CSI from a few noisy mmWave channel coefficients. The mmWave channel matrix is modeled as a two dimensional discrete Fourier transform (DFT) form of a sparse matrix due to the directional beamforming [79]. Since PCI and DFT matrices are mutually incoherent, the Fourier representation of the channel matrix is utilized in PCI based CS framework to estimate the sparse matrix associated with the channel matrix in the DFT domain. The rank of the channel matrix (or the number of dominant paths) is estimated by

calculating the number of non-zero coefficients in the above estimated sparse matrix. This estimated rank and sparse coefficients have been used jointly in an MF framework to recover the channel matrix. The main contributions of the proposed method, PCI-MF have been summarized below:

- Unlike the existing algorithm of [80], PCI-MF is not constrained due to the following: *number of minimum transmissions during training phase* should be greater than or equal to the total number of transmitter antennas (N_{T}). Hence, it can estimate the full CSI from a few channel coefficients.
- PCI-MF has been shown to estimate the massive MIMO mmWave channel more accurately as compared to recent state-of-the-art algorithms such as [20, 21] and hence, provides a better achievable spectrum efficiency (ASE) for a mmWave MIMO communication system. For instance, it has been shown that at 25 dB SNR and 32 $\times$ 32 MIMO configuration, PCI-MF is able to achieve ASE of 16.09 bits/sec/Hz with only 30% of CSI, which is comparable to ASE achieved when full CSI is available.
- The improvement in the performance of PCI-MF has also been verified against numerous parameters such as antenna configuration (uniform linear array, uniform planar array), MIMO configurations (32 $\times$ 32, 64 $\times$ 64), operating frequencies (28 GHz, 92 GHz) and fading channel models (Rayleigh fading and Nakagami fading).
- Results have also been verified on realistic data given in [2, 3]. PCI-MF is obtaining 5.45 dB and 16.93 dB improvement with 10% and 90% availabil-

ity of channel information as compared to the existing methods.

Notations: $\mathbf{X}'$, $\mathbf{X}^*$ and $\mathbf{X}^H$ denote the transpose, conjugate, and the Hermitian (conjugate transpose) of matrix $\mathbf{X}$, respectively. The element corresponding to the i^{th} row and j^{th} column of a matrix $\mathbf{X}$ is represented by $X(i,j)$. The i^{th} element of a vector $\mathbf{x}$ is represented as $x(i)$. The vectorization of matrix $\mathbf{X}$ is denoted as $\mathbf{X}(:)$. $\mathcal{D}_a$ is a normalized DFT matrix of size $a \times a$. $\mathbf{X} \otimes \mathbf{Y}$ and $\mathbf{X} \odot \mathbf{Y}$ represent the Kronecker and Hadamard products between matrices $\mathbf{X}$ and $\mathbf{Y}$, respectively. The l^p norm of a matrix or a vector is represented as $||\cdot||_p$. Binary, complex and real matrices of size $a \times b$ are represented by $\mathbb{B}^{a\times b}$, $\mathbb{C}^{a\times b}$ and $\Re^{a\times b}$, respectively. A random variable Z with Gaussian distribution with mean μ_g and variance σ_g^2 is represented as $Z \sim \mathcal{N}(\mu_g, \sigma_g^2)$. Similarly, the complex Gaussian random variable will be represented as $Z \sim \mathcal{CN}(\mu_g, \sigma_g^2)$. An exponentially distributed random variable Z with mean λ_e^{-1} is denoted as $Z \sim \varepsilon(\lambda_e)$. The Rayleigh distribution with variance σ_r^2 is represented as $Z \sim \mathcal{R}(\sigma_r^2)$. Further, a random variable with the Nakagami distribution is denoted as $Z \sim \mathcal{NG}(m, \Omega)$, where m is the shape parameter and Ω is the controlling parameter. Moreover, Poisson distribution with mean μ_{po} and Laplace distribution with standard deviation σ_{lp} are represented as $Z \sim \mathcal{P}(\mu_{po})$ and $Z \sim \mathcal{L}(\sigma_{lp})$, respectively. Lastly, a uniformly distributed Z between variables a_u and b_u is represented as $Z \sim \mathcal{U}(a_u, b_u)$.

4.2 Channel and System Model

4.2.1 Channel model

Consider a mmWave massive MIMO channel with N_{T} transmit and N_{R} receive antennas. The geometrical model of $\mathbf{H} \in \mathbb{C}^{N_{\mathrm{R}} \times N_{\mathrm{T}}}$ is given in [31, 79] as:

$$\mathbf{H} = \sqrt{\frac{N_{\mathrm{R}} N_{\mathrm{T}}}{\rho}} \sum_{l=1}^{L} \alpha_l \mathbf{A}_{\mathrm{T}}(l) \mathbf{A}_{\mathrm{R}}(l)^H, \tag{4.1}$$

where $\mathbf{A}_{\mathrm{T}}(l) \in \mathbb{C}^{N_{\mathrm{T}} \times 1}$ and $\mathbf{A}_{\mathrm{R}}(l) \in \mathbb{C}^{N_{\mathrm{R}} \times 1}$ represent the steering vectors at the transmitter and receiver of the l^{th} path, respectively. In addition, L is the total number of dominant paths. The maximum possible value of L can be obtained using $L = \sum_{j=1}^{N_{\mathrm{c}}} L_j$, where N_{c} is the total number of clusters and L_j is the number of dominant paths in the j^{th} cluster. Furthermore, α_l is the complex small scale fading gain of the l^{th} path and ρ is the average path loss between transmitter and receiver. The channel model of (4.1) can be re-written in the matrix form as:

$$\mathbf{H} = \mathbf{A}_{\mathrm{R}} \mathbf{Z} \mathbf{A}_{\mathrm{T}}^H, \tag{4.2}$$

where $\mathbf{A}_{\mathrm{R}} \in \mathbb{C}^{N_{\mathrm{R}} \times L}$ and $\mathbf{A}_{\mathrm{T}} \in \mathbb{C}^{N_{\mathrm{T}} \times L}$ are given by $[\mathbf{A}_{\mathrm{R}}(1) \;\; \mathbf{A}_{\mathrm{R}}(2) \; ... \; \mathbf{A}_{\mathrm{R}}(L)]$ and $[\mathbf{A}_{\mathrm{T}}(1) \; \mathbf{A}_{\mathrm{T}}(2) \; ... \; \mathbf{A}_{\mathrm{T}}(L)]$, respectively. $\mathbf{Z} \in \mathbb{C}^{L \times L}$ is a diagonal matrix with diagonal entries $\sqrt{\frac{N_{\mathrm{T}} N_{\mathrm{R}}}{\rho}} \alpha_l$, where $l = 1, 2...L$.

Based upon the geometrical arrangement of the antennas at the transmitter as well as the receiver, different type of steering vectors can be obtained [21]. The commonly used geometrical arrangements are uniform linear array (ULA)

and uniform planar array (UPA), which are described below.

4.2.1.1 ULA

For ULA, antennas are placed in a line with uniform spacing of d_{x} between all consecutive antennas as shown in Fig. 4.1. If $\Theta_{\mathrm{l}}^{\mathrm{T}}$ is the azimuth angle of departure (AoD) of the l^{th} path, then the steering vector at the transmitter for the l^{th} path will be given by

$$\mathbf{A}_{\mathrm{T}}(\Theta_{\mathrm{l}}^{\mathrm{T}}) = \frac{1}{\sqrt{N_{\mathrm{T}}}}[1 \; e^{j\frac{2\pi}{\lambda_{\mathrm{c}}}d_{\mathrm{x}}\sin\Theta_{\mathrm{l}}^{\mathrm{T}}} \; \ldots \; e^{j\frac{2\pi}{\lambda_{\mathrm{c}}}d_{\mathrm{x}}(N_{\mathrm{T}}-1)\sin\Theta_{\mathrm{l}}^{\mathrm{T}}}]'. \tag{4.3}$$

Similarly the steering vector of ULA at the receiver for the l^{th} path can be

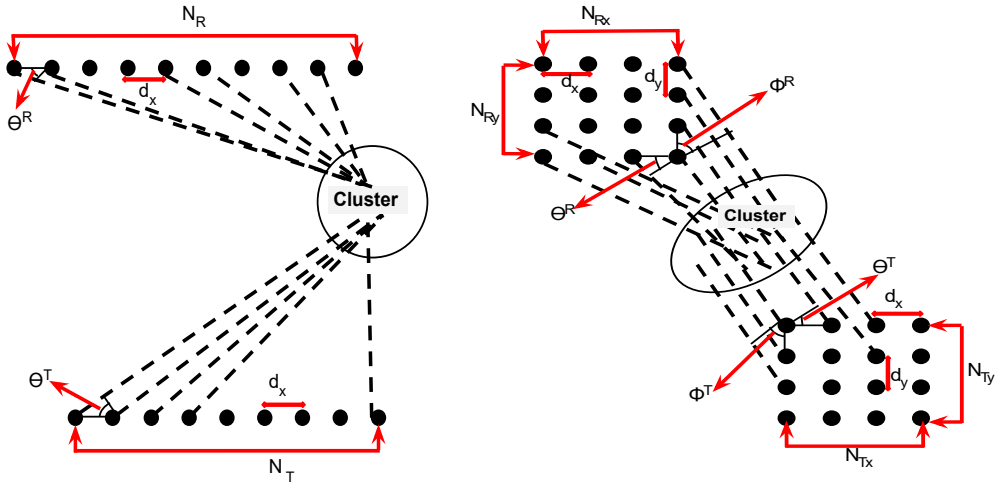

a) ULA b) UPA

Figure 4.1: Beamforming between transmitter and receiver with different antenna configurations

obtained from (4.3) by replacing AoD, i.e., $\Theta_{\mathrm{l}}^{\mathrm{T}}$ with angle of arrival (AoA), i.e, $\Theta_{\mathrm{l}}^{\mathrm{R}}$ and N_{T} with N_{R}. Further, λ_{c} is the wavelength of the signal. Moreover, inline with the previous work [20, 21], it is assumed that AoA and AoD lie on the discretized grids.

From (4.2) and (4.3), it is observed that the structure of $\mathbf{A}_{\mathrm{T}}$ and $\mathbf{A}_{\mathrm{R}}$ for ULA resemble normalized DFT matrix and hence, the DFT matrix can be segregated from (4.2) as follows

$$\begin{aligned}\mathbf{H} &= \mathcal{D}_{\mathrm{N_R}}\mathcal{D}_{N_{\mathrm{R}}}^{H}\mathbf{A}_{\mathrm{R}}\mathbf{Z}\mathbf{A}_{\mathrm{T}}^{H}\mathcal{D}_{\mathrm{N_T}}\mathcal{D}_{\mathrm{N_T}}^{H} \\ &= \mathcal{D}_{\mathrm{N_R}}\mathbf{S}\mathcal{D}_{N_{\mathrm{T}}}^{H},\end{aligned} \tag{4.4}$$

where $\mathbf{S} = \mathcal{D}_{N_{\mathrm{R}}}^{H}\mathbf{A}_{\mathrm{R}}\mathbf{Z}\mathbf{A}_{\mathrm{T}}^{H}\mathcal{D}_{\mathrm{N_T}} \in \mathbb{C}^{N_{\mathrm{R}}\times N_{\mathrm{T}}}$ is a diagonal matrix with L non-zero diagonal entries and contains the information of AoAs, AoDs and α_l.

4.2.1.2 UPA

For UPA, antennas are placed in a plane, with d_{x} and d_{y} spacing between two consecutive antennas lying in a horizontal and vertical line, respectively as shown in Fig. 4.1. Let us assume that N_{Tx} and N_{Ty} are the number of antennas placed horizontally and vertically, respectively, at the transmitter such that $N_{\mathrm{T}} = N_{\mathrm{Tx}}N_{\mathrm{Ty}}$. Similarly, N_{Rx} and N_{Ry} are the number of antennas placed horizontally and vertically, respectively, at the receiver such that $N_{\mathrm{R}} = N_{\mathrm{Rx}}N_{\mathrm{Ry}}$. If $\Theta_{\mathrm{l}}^{\mathrm{T}}$ and Φ_l^T are the azimuth and elevation AoDs of the l^{th} path, respectively, then the steering vector at the transmitter for UPA will be given by

$$\begin{aligned}&\mathbf{A}_{\mathrm{T}}(\Theta_{\mathrm{l}}^{\mathrm{T}}, \Phi_{\mathrm{l}}^{\mathrm{T}}) = \\ &\frac{1}{\sqrt{N_{\mathrm{Tx}}N_{\mathrm{Ty}}}}[1 \; e^{j\frac{2\pi}{\lambda_{\mathrm{c}}}[d_{\mathrm{x}}\sin\Theta_{\mathrm{l}}^{\mathrm{T}}\cos\Phi_{\mathrm{l}}^{\mathrm{T}} + d_{\mathrm{y}}\sin\Theta_{\mathrm{l}}^{\mathrm{T}}\sin\Phi_{\mathrm{l}}^{\mathrm{T}}]} \ldots \\ &e^{j\frac{2\pi}{\lambda_{\mathrm{c}}}[d_{\mathrm{x}}(N_{\mathrm{Tx}}-1)\sin\Theta_{\mathrm{l}}^{\mathrm{T}}\cos\Phi_{\mathrm{l}}^{\mathrm{T}} + d_{\mathrm{y}}(N_{\mathrm{Ty}}-1)\sin\Theta_{\mathrm{l}}^{\mathrm{T}}\sin\Phi_{\mathrm{l}}^{\mathrm{T}}]}]'.\end{aligned} \tag{4.5}$$

Similarly, the steering vector of UPA at the receiver for the l^{th} path can be obtained from (4.5) by replacing $\Theta_{\mathrm{l}}^{\mathrm{T}}$ with $\Theta_{\mathrm{l}}^{\mathrm{R}}$, $\Phi_{\mathrm{l}}^{\mathrm{T}}$ with $\Phi_{\mathrm{l}}^{\mathrm{R}}$ (elevation AoA), N_{Tx} with N_{Rx} and, N_{Ty} with N_{Ry}.

Unlike ULA, in UPA the structure of $\mathbf{A}_{\mathrm{T}}$ and $\mathbf{A}_{\mathrm{R}}$ resemble the Kronecker product of the normalized DFT matrices (from (4.2), (4.5)) and hence, (4.2) can be simplified as below:

$$\begin{aligned}\mathbf{H} &= \mathcal{K}_{\mathrm{N_R}}\mathcal{K}_{N_{\mathrm{R}}}^{H}\mathbf{K}_{R}\mathbf{Z}\mathbf{K}_{T}^{H}\mathcal{K}_{\mathrm{N_T}}\mathcal{K}_{\mathrm{N_T}}^{H} \\ &= \mathcal{K}_{\mathrm{N_R}}\mathbf{S}\mathcal{K}_{N_{\mathrm{T}}}^{H}, \end{aligned} \tag{4.6}$$

where $\mathcal{K}_{\mathrm{N_R}} = \mathcal{D}_{\mathrm{N_{Rx}}} \otimes \mathcal{D}_{\mathrm{N_{Ry}}}$ and $\mathcal{K}_{\mathrm{N_T}} = \mathcal{D}_{\mathrm{N_{Tx}}} \otimes \mathcal{D}_{\mathrm{N_{Ty}}}$. Further, $\mathbf{S} = \mathcal{K}_{N_{\mathrm{R}}}^{H}\mathbf{A}_{\mathrm{R}}\mathbf{Z}\mathbf{A}_{\mathrm{T}}^{H}\mathcal{K}_{\mathrm{N_T}} \in \mathbb{C}^{N_{\mathrm{R}} \times N_{\mathrm{T}}}$ is a diagonal matrix with L non-zero diagonal entries containing the information of AoAs, AoDs (azimuth as well as elevation), and α_l.

From (4.4) and (4.6), it is observed that $\mathbf{S} \in \mathbb{C}^{N_{\mathrm{R}} \times N_{\mathrm{T}}}$ has only L non-zero diagonal coefficients. This implies that $\mathbf{S}$ is a sparse matrix because the number of non-zero coefficients is much smaller than the total number of coefficients in the matrix i.e., $L << N_{\mathrm{T}}N_{\mathrm{R}}$. Furthermore, it is a diagonal matrix with the number of non-zero coefficients at the diagonal less than their dimension ($L < \min(N_{\mathrm{T}}, N_{\mathrm{R}})$). Hence, $\mathbf{H}$ is a low-rank matrix.

In mmWave massive MIMO systems, the value of N_{R} and N_{T} is large, and hence, the estimation of many channel coefficients corresponding to $\mathbf{H}$ will be impractical. Therefore, in Section-4.3, various properties of massive MIMO based mmWave channel matrix, such as low rank property, sparsity and its DFT

representation have been utilized jointly to recover entire CSI from a few estimated channel coefficients.

4.2.2 System Model

Given a hybrid architecture of mmWave massive MIMO system with N_{RF} number of RF chains deployed at both transmitter as well as receiver. Let us assume that the transmitter is beamforming a data stream of length N_{s}, represented by $\mathbf{x}$ at the receiver (shown in Fig. 4.2). The transmitter applies an $N_{\mathrm{RF}} \times N_{\mathrm{s}}$ baseband precoder denoted by $\mathbf{F}_{\mathrm{T-BB}}$, followed by an $N_{\mathrm{T}} \times N_{\mathrm{RF}}$ RF precoder denoted by $\mathbf{F}_{\mathrm{T-RF}}$ and hence, the transmitter precoding matrix is given by $\mathbf{F}_{\mathrm{T}} = \mathbf{F}_{\mathrm{T-RF}} \times \mathbf{F}_{\mathrm{T-BB}}$. The signal observed at the receiver is passed to an $N_{\mathrm{RF}} \times N_{\mathrm{R}}$ RF precoder denoted by $\mathbf{F}_{\mathrm{R-RF}}$, followed by an $m_{\mathrm{r}} \times N_{\mathrm{RF}}$ baseband precoder to obtain m_{r} measurements denoted by $\mathbf{F}_{\mathrm{R-BB}}$ and hence, the receiver combining precoding matrix is given by $\mathbf{F}_{\mathrm{R}} = \mathbf{F}_{\mathrm{R-BB}} \times \mathbf{F}_{\mathrm{R-RF}}$. The system model has been illustrated in Fig. 4.2.

4.2.2.1 Training phase

During the training phase, the transmitter transmits the known data symbol, also known as pilot to estimate the channel coefficients. If the transmitter is beamforming a pilot p, i.e., $N_{\mathrm{s}} = 1$, then the combined received signal at the receiver with m_{r} measurements of p can be written as

$$\mathbf{y} = \mathbf{F}_{\mathrm{R}}\mathbf{H}\mathbf{F}_{\mathrm{T}}p + \mathbf{n}, \tag{4.7}$$

where $\mathbf{F}_{\mathrm{T}} \in \mathbb{C}^{N_{\mathrm{T}} \times 1}$. Further, the receiver combining precoding matrix obtaining m_{r} measurements of the transmitted symbol at the receiver can be expressed as $\mathbf{F}_{\mathrm{R}} = [\mathbf{f}_{\mathrm{R}_1}\ \mathbf{f}_{\mathrm{R}_2}\ ...\mathbf{f}_{\mathrm{R}_{\mathrm{m_r}}}]' \in \mathbb{C}^{m_{\mathrm{r}} \times N_{\mathrm{R}}}$, where $\mathbf{f}_{\mathrm{R_i}} \in \mathbb{C}^{N_{\mathrm{R}} \times 1}\ \forall i$. Additionally, $\mathbf{n} \in \mathbb{C}^{m_{\mathrm{r}} \times 1}$ is the noise vector and $\mathbf{H} \in \mathbb{C}^{N_{\mathrm{R}} \times N_{\mathrm{T}}}$ is the mmWave MIMO channel matrix.

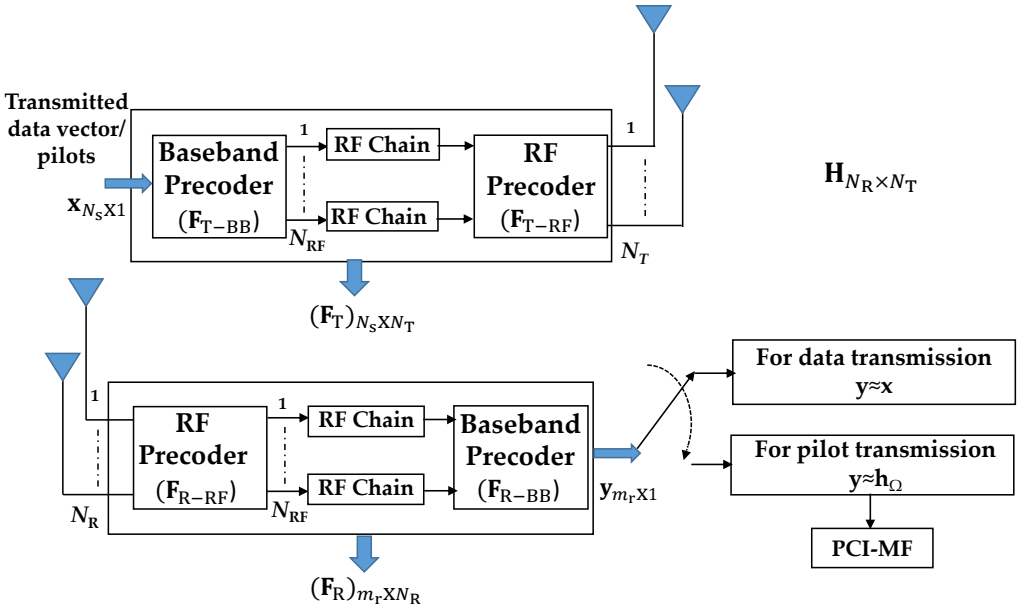

Figure 4.2: System model

It may be noted that inline with the previous work [21, 80, 81], to reduce the power consumption and complexity during the training phase, only one transmitting antenna is activated in each transmission. Hence, the number of pilots transmitted is equal to the number of transmitting antennas selected. If i^{th} transmitting antenna is activated, then $\mathbf{F}_{\mathrm{T}}$ should be designed in such a way that $\mathbf{F}_{\mathrm{T}}(i) = 1$ and all the remaining entries will be zero [80]. The pilot, p is known at the receiver and assumed to be 1. Let's assume, $H(i, j_1)$, $H(i, j_2)$ and $H(i, j_3)$ needs to be estimated, which implies $\mathbf{f}_{\mathrm{R}_1}(j_1) = 1$, $\mathbf{f}_{\mathrm{R}_2}(j_2) = 1$, $\mathbf{f}_{\mathrm{R}_3}(j_3) = 1$, and all the remaining entries of $\mathbf{F}_{\mathrm{R}}$ will be zero and hence, the received signal,

$\mathbf{y} = [H(i, j_1)\ H(i, j_2)\ H(i, j_2)]'$. It may be noted that the number of channels estimated per transmission is limited by m_{r}, which is again limited by the number of RF chains at the receiver (N_{RF}), as $m_{\mathrm{r}} \leq N_{\mathrm{RF}}$. Therefore, in order to reduce the pilots overhead and hardware constraints during the training phase, only M coefficients of $\mathbf{H}$ have been estimated from the total $N_{\mathrm{T}}N_{\mathrm{R}}$ coefficients. In the subsequent section, we will show how the complete channel matrix can be estimated from these M coefficients.

4.3 Proposed *PCI-MF* for mmWave channel estimation

This section shows the utilization of proposed *PCI-MF* method to recover the entire channel matrix from a few estimated channel coefficients (i.e., M). The estimated coefficients of $\mathbf{H}$ are stacked in a vector $\mathbf{h}_\Omega \in \mathbb{C}^{M\times 1}$ and is written as:

$$\mathbf{h}_\Omega = \mathbf{\Phi h} + \mathbf{n}, \tag{4.8}$$

$\mathbf{h} \in \mathbb{C}^{N_{\mathrm{R}}N_{\mathrm{T}}\times 1}$ is equal of $\mathbf{H}(:)$ and $\mathbf{n} \in \mathbb{C}^{N_{\mathrm{R}}N_{\mathrm{T}}\times 1}$ is a complex Gaussian noise vector. However, the measurement matrix $\mathbf{\Phi} \in \mathbb{B}^{M\times N_{\mathrm{R}}N_{\mathrm{T}}}$ is the PCI matrix. We illustrate the above with an example. Consider a channel matrix, $\mathbf{H} = \begin{bmatrix} h_{11} & h_{12} \\ h_{21} & h_{22} \end{bmatrix}$, and only two coefficients h_{21} and h_{22} have been estimated in the training phase. Hence, $\mathbf{h}_\Omega = \begin{bmatrix} h_{21} & h_{22} \end{bmatrix}'$ and the corresponding PCI matrix, $\mathbf{\Phi}$ will be $\begin{bmatrix} 0 & 0 & 1 & 0 \\ 0 & 0 & 0 & 1 \end{bmatrix}$.

For ULA, using (4.4), $\mathbf{h} = (\mathcal{D}^{*}_{\mathrm{NT}} \otimes \mathcal{D}_{\mathrm{NR}})\mathbf{s}$, where $\mathbf{s} = \mathbf{S}(:)$. Hence, (4.8) can also be re-written as:

$$\begin{aligned}\mathbf{h}_{\Omega} &= \mathbf{\Phi}(\mathcal{D}^{*}_{\mathrm{NT}} \otimes \mathcal{D}_{\mathrm{NR}})\mathbf{s} + \mathbf{n} \\ &= \mathbf{\Phi}\mathbf{\Psi}_{\mathrm{l}}\mathbf{s} + \mathbf{n} \quad (\because \mathbf{\Psi}_{\mathrm{l}} = \mathcal{D}^{*}_{\mathrm{NT}} \otimes \mathcal{D}_{\mathrm{NR}}) \\ &= \mathbf{A}_{\mathrm{l}}\mathbf{s} + \mathbf{n} \quad (\because \mathbf{A}_{\mathrm{l}} = \mathbf{\Phi}\mathbf{\Psi}_{\mathrm{l}}),\end{aligned} \tag{4.9}$$

where $\mathbf{A}_{\mathrm{l}} \in \mathbb{C}^{M \times N_{\mathrm{T}}N_{\mathrm{R}}}$ and $\mathbf{\Psi}_{\mathrm{l}} \in \mathbb{C}^{N_{\mathrm{T}}N_{\mathrm{R}} \times N_{\mathrm{T}}N_{\mathrm{R}}}$. However, for UPA (from (4.6)) $\mathbf{h} = (\mathcal{K}^{*}_{\mathrm{NT}} \otimes \bar{\mathcal{K}}_{NR})\mathbf{s}$, where $\mathbf{s} = \mathbf{S}(:)$. Hence, (4.8) can be re-written as

$$\begin{aligned}\mathbf{h}_{\Omega} &= \mathbf{\Phi}(\mathcal{K}^{*}_{\mathrm{NT}} \otimes \mathcal{K}_{NR})\mathbf{s} + \mathbf{n} \\ &= \mathbf{\Phi}((\mathcal{D}_{\mathrm{N_{Tx}}} \otimes \mathcal{D}_{\mathrm{N_{Ty}}})^{*} \otimes (\mathcal{D}_{\mathrm{N_{Rx}}} \otimes \mathcal{D}_{\mathrm{N_{Ry}}}))\mathbf{s} + \mathbf{n} \\ &= \mathbf{\Phi}\mathbf{\Psi}_{\mathrm{p}}\mathbf{s} + \mathbf{n} \\ &= \mathbf{A}_{\mathrm{p}}\mathbf{s} + \mathbf{n}. \quad (\because \mathbf{A}_{\mathrm{p}} = \mathbf{\Phi}\mathbf{\Psi}_{\mathrm{p}}),\end{aligned} \tag{4.10}$$

where $\mathbf{A}_{\mathrm{p}} \in \mathbb{C}^{M \times N_{\mathrm{T}}N_{\mathrm{R}}}$ and $\mathbf{\Psi}_{\mathrm{p}} \in \mathbb{C}^{N_{\mathrm{T}}N_{\mathrm{R}} \times N_{\mathrm{T}}N_{\mathrm{R}}}$.

Since $\mathbf{s} \in \mathbb{C}^{N_{\mathrm{T}}N_{\mathrm{R}} \times 1}$ is the sparse vector, (4.9) and (4.10) resemble the compressive sensing framework [10], where $\mathbf{h}_{\Omega}$ is the compressive measurements, $\mathbf{\Phi}$ is the PCI sensing matrix, and $\mathbf{\Psi}_{\mathrm{l}}$ and $\mathbf{\Psi}_{\mathrm{p}}$ are the sparsifying matrices for ULA and UPA, respectively. The mutual coherence between $\mathbf{\Phi}$ and $\mathbf{\Psi}_{\mathrm{l}}$ for CS framework provided in (4.9) is calculated using (2.4) as follows:

$$\mu(\mathbf{\Phi}, \mathbf{\Psi}_{\mathrm{l}}) = \sqrt{N_{\mathrm{T}}N_{\mathrm{R}}} \max_{\forall i,j} |\mathbf{\Psi}_{\mathrm{l}}(i,j)| = 1. \tag{4.11}$$

Similarly, the mutual coherence between $\mathbf{\Phi}$ and $\mathbf{\Psi}_{\mathrm{p}}$ for CS framework shown

in (4.10) will be given by:

$$\mu(\mathbf{\Phi}, \mathbf{\Psi}_{\mathrm{p}}) = \sqrt{N_{\mathrm{Tx}} N_{\mathrm{Ty}} N_{\mathrm{Rx}} N_{\mathrm{Ry}}} \max_{\forall i,j} |\mathbf{\Psi}_{\mathrm{p}}(i,j)| = 1. \tag{4.12}$$

From (4.11) and (4.12), it is observed that both ULA (4.9) as well as UPA (4.10) CS frameworks have minimum coherence of 1 and hence, the following l^1 minimization problem has been solved to recover $\mathbf{s}$ from $\mathbf{h}_\Omega$:

$$P_1 : \min_{s} ||\mathbf{h}_\Omega - \mathbf{A}\mathbf{s}||_2^2 + \lambda ||\mathbf{s}||_1, \tag{4.13}$$

where $\mathbf{A} = \begin{cases} \mathbf{A}_{\mathrm{l}} & \text{for ULA} \\ \mathbf{A}_{\mathrm{p}} & \text{for UPA} \end{cases}$, and λ is the regularization parameters to control the level of sparsity and the data accuracy. Iterative soft thresholding method (ISTA) [50, 82] can be used to solve (4.13). The sparse vectors $\mathbf{s}$ determined above either for ULA or for UPA can be used to estimate channel matrix $\mathbf{H}$ by jointly exploiting it's low-rank nature in a matrix factorization framework as follows:

$$P_2 : \min_{\mathbf{H},\mathbf{U},\mathbf{V}} (||\mathbf{H} - \mathbf{U}\mathbf{V}||_F^2 + \rho_1 ||\mathbf{U}||_F^2 + \rho_2 ||\mathbf{V}||_F^2) + \mu ||\mathbf{h}_\Omega - \mathbf{A}\mathbf{s}||_F^2. \tag{4.14}$$

Matrices $\mathbf{U}$ and $\mathbf{V}$ have the dimension of $N_{\mathrm{R}} \times r$ and $r \times N_{\mathrm{T}}$, respectively, where r is the rank of the channel matrix $\mathbf{H}$ that can be determined by calculating the number of non-zero values in $\mathbf{s}$ [2]. The parameter ρ_1 and ρ_2 control the magnitude of matrices $\mathbf{U}$ and $\mathbf{V}$, respectively. The term $\mu ||\mathbf{h}_\Omega - \mathbf{A}\mathbf{s}||_F^2$ has been added to penalize the error caused due to noisy estimation of $\mathbf{s}$ (in (4.13)). Generally, $\mathbf{s}$

[2]The coefficients of $\mathbf{s}$ having smaller value tending towards zero will be considered as zero.

will be estimated noisy for lower received signal-to-noise ratio (SNR) and/or for low value of measurement ratio defined as $\mathrm{MR} = \frac{M}{N_{\mathrm{T}} N_{\mathrm{R}}}$. Hence, addition of this term provides robust estimation of $\mathbf{H}$. A higher value of μ implies more weight to the term $||\mathbf{h}_\Omega - \mathbf{A}\mathbf{s}||_F^2$, in the case of noisy estimation of $\mathbf{s}$. The problem P_2 given in (4.14) can be solved using the alternate direction method of multipliers (ADMM) by dividing into following three sub-problems [83] as follows:

$$P_2(a) : \min_{\mathbf{U}} ||\mathbf{H} - \mathbf{U}\mathbf{V}||_F^2 + \rho_1 ||\mathbf{U}||_F^2. \tag{4.15}$$

$$P_2(b) : \min_{\mathbf{V}} ||\mathbf{H} - \mathbf{U}\mathbf{V}||_F^2 + \rho_2 ||\mathbf{V}||_F^2. \tag{4.16}$$

$$P_2(c) : \min_{\mathbf{H}} ||\mathbf{H} - \mathbf{U}\mathbf{V}||_F^2 + \mu ||\mathbf{h}_\Omega - \mathbf{A}\mathbf{s}||_F^2. \tag{4.17}$$

All three sub-problems mentioned above are the simple least square problems and are solved as follows. The problem $P_2(a)$ is written as:

$$P_2(a) : \min_{\mathbf{U}} ||\tilde{\mathbf{H}} - \mathbf{U}\tilde{\mathbf{V}}||_F^2, \tag{4.18}$$

where $\tilde{\mathbf{H}} = \begin{bmatrix} \mathbf{H} & \mathbf{0}_{N_{\mathrm{R}} \times r} \end{bmatrix}$ and $\tilde{\mathbf{V}} = \begin{bmatrix} \mathbf{V} & \sqrt{\rho_1}\mathbf{I}_r \end{bmatrix}$. This implies

$$\mathbf{U} = \tilde{\mathbf{H}}\tilde{\mathbf{V}}'(\tilde{\mathbf{V}}\tilde{\mathbf{V}}')^{-1}. \tag{4.19}$$

Similarly the problem $P_2(b)$ is written as:

$$P_2(b) : \min_{\mathbf{V}} ||\hat{\mathbf{H}} - \hat{\mathbf{U}}\mathbf{V}||_F^2, \tag{4.20}$$

where $\hat{\mathbf{H}} = \begin{bmatrix} \mathbf{H} \\ \mathbf{0}_{r \times N_{\mathrm{T}}} \end{bmatrix}$ and $\hat{\mathbf{U}} = \begin{bmatrix} \mathbf{U} \\ \sqrt{\rho_2}\mathbf{I}_r \end{bmatrix}$. Hence,

$$\mathbf{V} = (\hat{\mathbf{U}}'\hat{\mathbf{U}})^{-1}\hat{\mathbf{U}}'\hat{\mathbf{H}}. \tag{4.21}$$

The problem $P_2(c)$ is written as:

$$\min_{\mathbf{h}} ||\mathbf{h} - (\mathbf{I}_{N_\mathrm{T}} \otimes \mathbf{U})\mathbf{v}||_F^2 + \mu||\mathbf{\Phi h} - \mathbf{As}||_F^2, \tag{4.22}$$

where $\mathbf{h} = \mathbf{H}(:)$ and $\mathbf{v} = \mathbf{V}(:)$. Differentiating (4.22) for $\mathbf{h}$ yields:

$$\mathbf{h} = (\mathbf{I}_{N_\mathrm{T}N_\mathrm{R}} + \mu\mathbf{\Phi}'\mathbf{\Phi})^{-1}((\mathbf{I}_{N_\mathrm{T}} \otimes \mathbf{U})\mathbf{v} + \mu\mathbf{\Phi}'\mathbf{As}). \tag{4.23}$$

It is to be noted that for high received SNR with high MR [3], the problem $P_2(c)$ can be simply reduced into two steps: 1) $\mathbf{H} = \mathbf{UV}$. 2) Replace the estimated channel coefficients i.e., $\mathbf{h}_\Omega$ by $\mathbf{As}$. The algorithmic steps for the proposed PCI-MF method are provided in Algorithm 1.

4.4 Complexity Analysis

The complexity of the state-of-the-art methods such as for the two-stage methods of [20] and [21] is given as $\mathcal{O}(max(N_\mathrm{R}, N_\mathrm{T})N_\mathrm{R}N_\mathrm{T})$ because both these methods are dominated by singular value thresholding (SVT) [62].

The complexity of the proposed method will depend upon the complexity of problem P_1 and all three sub-problems of P_2, i.e, $P_2(a)$, $P_2(b)$ and $P_2(c)$. The complexity of P_1, which is usually solved by method such as ISTA is given as

[3] Typically, for our experimental setup, low SNR implies 0 to 5 dB and low MR implies availability of 10% to 20% channel coefficients. Hence, high SNR with high MR implies availability of more than 5 dB SNR and 20% channel coefficients.

[4] n_1, n_2 and n_3 represent the maximum number of iterations.

[5] $\mathcal{D}_\mathrm{a}$ will generate a DFT matrix of size a.

[6] $sgn = \begin{cases} -1 & \text{if } x < 0 \\ 0 & \text{if } x = 0 \\ 1 & \text{if } x > 0 \end{cases}$

[7] resize converts the given vector into a matrix of given size.

Algorithm 3 PCI-MF

Input: $\mathbf{\Phi}$, $\mathbf{h}_\Omega$, N_T, N_R, N_Tx, N_Ty, N_Rx, N_Ry, μ, λ, ρ_1, ρ_2, n_1, n_2, n_3 [4]
Initialization: $\mathbf{s} = zeros(N_\mathrm{T}N_\mathrm{R} \times 1)$
For ULA: $\mathbf{\Psi}_\mathrm{l} = \mathcal{D}_\mathrm{NT}^* \otimes \mathcal{D}_\mathrm{NR}$ [5]
For UPA: $\mathbf{\Psi}_\mathrm{p} = (\mathcal{D}_{\mathrm{N_{Tx}}} \otimes \mathcal{D}_{\mathrm{N_{Ty}}})^* \otimes (\mathcal{D}_{\mathrm{N_{Rx}}} \otimes \mathcal{D}_{\mathrm{N_{Ry}}})$
$\mathbf{A} = \mathbf{\Psi}\mathbf{\Phi}$, where $\mathbf{\Psi} = \begin{cases} \mathbf{\Psi}_\mathrm{l} & \text{for ULA} \\ \mathbf{\Psi}_\mathrm{p} & \text{for UPA} \end{cases}$
$\alpha = \max(eig(\mathbf{A}'\mathbf{A}))$
for k_1 = $1 : n_1$ **do**
  $\mathbf{s} = sgn(\mathbf{s} + \frac{1}{\alpha}\mathbf{A}'\mathbf{h}_\Omega - \mathbf{A}\mathbf{s}) \max(0, |\mathbf{A}'\mathbf{h}_\Omega - \mathbf{A}\mathbf{s}| - \frac{\lambda}{2\alpha})$ [6]
end for
r = sparsity of **s**
$\mathbf{h} = \mathbf{\Psi}\mathbf{s}$
for k_2 = $1 : n_2$ **do**
  $\mathbf{H} = resize(\mathbf{h}, [N_\mathrm{R}, N_\mathrm{T}])$ [7]
  $\mathbf{V} = \mathbf{H}(1 : r, :)$
  for k_3 = $1 : n_3$ **do**
    $\tilde{\mathbf{H}} = \begin{bmatrix} \mathbf{H} & \mathbf{0}_{N_\mathrm{R} \times r} \end{bmatrix}$ and $\tilde{\mathbf{V}} = \begin{bmatrix} \mathbf{V} & \sqrt{\rho_1}\mathbf{I}_r \end{bmatrix}$
    $\mathbf{U} = \tilde{\mathbf{H}}\tilde{\mathbf{V}}'(\tilde{\mathbf{V}}\tilde{\mathbf{V}}')^{-1}$
    $\hat{\mathbf{H}} = \begin{bmatrix} \mathbf{H} \\ \mathbf{0}_{r \times N_\mathrm{T}} \end{bmatrix}$, $\hat{\mathbf{U}} = \begin{bmatrix} \mathbf{U} \\ \sqrt{\rho_2}\mathbf{I}_r \end{bmatrix}$.
    $\mathbf{V} = (\hat{\mathbf{U}}'\hat{\mathbf{U}})^{-1}\hat{\mathbf{U}}'\hat{\mathbf{H}}$
  end for
  At low SNR and/or low MR:
  $\mathbf{h} = (\mathbf{I}_{N_\mathrm{T}N_\mathrm{R}} + \mu\mathbf{\Phi}'\mathbf{\Phi})^{-1}((\mathbf{I}_{N_\mathrm{T}} \otimes \mathbf{U})\mathbf{v} + \mu\mathbf{\Phi}'\mathbf{A}\mathbf{s})$
  At high SNR with high MR:
  H=UV
  $\mathbf{p} = find(\mathbf{\Phi}(:) == 1)$
  $\mathbf{h} = \mathbf{H}(:), \mathbf{h}(\mathbf{p}) = \mathbf{A}\mathbf{s}$
end for
$\mathbf{H} = resize(\mathbf{h}, [N_\mathrm{R}, N_\mathrm{T}])$
Output: **H**

($\mathcal{O}(MN_{\mathrm{R}}N_{\mathrm{T}})$). However, the complexity of $P_2(a)$ and $P_2(b)$ is $\mathcal{O}(rN_{\mathrm{R}}N_{\mathrm{T}})$. For high SNR with high MR, the complexity of $P_2(c)$ is also $\mathcal{O}(rN_{\mathrm{R}}N_{\mathrm{T}})$. Therefore, in this case, the complexity of PCI-MF is $(\mathcal{O}(MN_{\mathrm{R}}N_{\mathrm{T}} + 3rN_{\mathrm{R}}N_{\mathrm{T}})) \approx \mathcal{O}(MN_{\mathrm{R}}N_{\mathrm{T}})$. The value of M varies from 1 to $N_{\mathrm{R}}N_{\mathrm{T}}$ and hence, the computational complexity of PCI-MF increases at higher values of M. Further, it is observed that the complexity of PCI-MF is dominated by ISTA and hence, method such as fast iterative soft thresholding method (FISTA) [50] can be used instead of ISTA to reduce the computational complexity of PCI-MF. However, at low SNR and/or low MR, the complexity of $P_2(c)$ is $(\mathcal{O}(N_{\mathrm{R}}^2N_{\mathrm{T}}^2))$. Hence, the complexity of PCI-MF will be $(\mathcal{O}(MN_{\mathrm{R}}N_{\mathrm{T}} + 2rN_{\mathrm{R}}N_{\mathrm{T}} + N_{\mathrm{R}}^2N_{\mathrm{T}}^2)) \approx \mathcal{O}(N_{\mathrm{R}}^2N_{\mathrm{T}}^2)$, which is a trade-off between complexity and performance. It may be noted that the above is a rare scenario and is applicable for applications with a very low value of SNR $\leq$ 5 dB and also a very low percentage of MR $\leq$ 20%. Consider Table I that presents the complexity comparison of different algorithms.

Table 4.1: Complexity comparison

Algorithm	**Complexity**
LMaFit [34]	$\mathcal{O}(rN_{\mathrm{R}}N_{\mathrm{T}})$
Two stage [20]	$\mathcal{O}(max(N_{\mathrm{R}}, N_{\mathrm{T}})N_{\mathrm{R}}N_{\mathrm{T}})$
E. Vlachos et al. [21]	$\mathcal{O}(max(N_{\mathrm{R}}, N_{\mathrm{T}})N_{\mathrm{R}}N_{\mathrm{T}})$
PCI-MF : At low SNR ($\leq$ 5 dB) and/or low MR ($\leq$ 20%)	$\mathcal{O}(N_{\mathrm{R}}^2N_{\mathrm{T}}^2)$
PCI-MF : At high SNR (>5 dB) with high MR (>20%)	$\mathcal{O}(MN_{\mathrm{R}}N_{\mathrm{T}})$

Table 4.2: Simulation parameters

f_c (GHz)	N_c	L_k	AoA/AoD	α_l
90 [21]	1	2	$\mathcal{L}(50^\circ)$	a) $\mathcal{R}(1)$ b) $\mathcal{NG}(0.5, 1)$
28 [2,3]	$max(1, \mathcal{P}(1.8))$	2	$\mathcal{N}(\mathcal{U}(0, 2\pi), \varepsilon(\lambda_a))$ $\lambda_a^{-1} = \begin{cases} 15.5 & \text{for } \Theta_l^{\mathrm{R}} \\ 6 & \text{for } \Phi_l^{\mathrm{R}} \\ 10.2 & \text{for } \Theta_l^{\mathrm{T}} \\ 0 & \text{for } \Phi_l^{\mathrm{T}} \end{cases}$	$\mathcal{R}(\gamma_l 10^{0.1PL})$ $\gamma_l = \frac{\gamma_l'}{\sum_{i=1}^{L} \gamma_l'}$, $\gamma_l' = U_l^{r_\tau - 1} 10^{-0.1 Z_l}$, $U_l \sim \mathcal{U}(0, 1)$, $Z_l \sim \mathcal{N}(0, 16)$, $PL = \alpha + 10\beta \log_{10}(d) + \zeta$ dB, $\alpha = 72$, $\beta = 2.92$, $\zeta \sim \mathcal{N}(0, 8.7$ dB$)$, $d_{t-r} = 100$ m.

4.5 Simulation and discussion

This section presents the simulation results of the proposed PCI-MF method. Results have been compared with the state-of-the-art methods such as the two-stage methods [20] and [21] presented by Xingjian et al. and by E. Vlachos et al., respectively. In addition to the above, the performance of PCI-MF has also been compared with the conventional matrix completion algorithm based on MF such as the low-rank matrix fitting (LMaFit) [34].

Simulations are performed against various parameters such as the MIMO configurations, SNR, MR, and L. Moreover, results have been obtained for two different operating frequencies (f_c) i.e., 90 GHz [21] and 28 GHz [2, 3]. The value of various parameters considered for both frequencies is summarized in Table II. Furthermore, for 28 GHz, simulations are performed for real-world parameters obtained at New York City. It is to be noted that for all the simulations, the distance between two consecutive antennas placed either horizontally or vertically is $\frac{\lambda_c}{2}$, which implies $d_x = d_y = \frac{\lambda_c}{2}$. The value of the regularization

parameters $\rho_1 = \rho_2 = 0.01$, whereas μ varies from 0.1 to 0.01.

For 90 GHz (Fig. 4.3-4.13), both AoA and AoD are Laplacian distributed with standard deviation 50° [21]. The value taken for the number of clusters (N_c) and the number of dominant paths in each cluster (L_k) are 2 and 1, respectively, which implies $L = 2$. For Figs. 4.3-4.10 instantaneous path loss is Rayleigh distributed with unit variance [21] and antenna configuration is ULA. Results for UPA are shown in Fig. 4.12. In prior literature [84–86], it has been observed that Nakagami channel fading model fits better than the Rayleigh fading model for mmWave band, especially, with directional beamforming. Therefore, results with Nakagami fading model are also shown in Fig. 4.13.

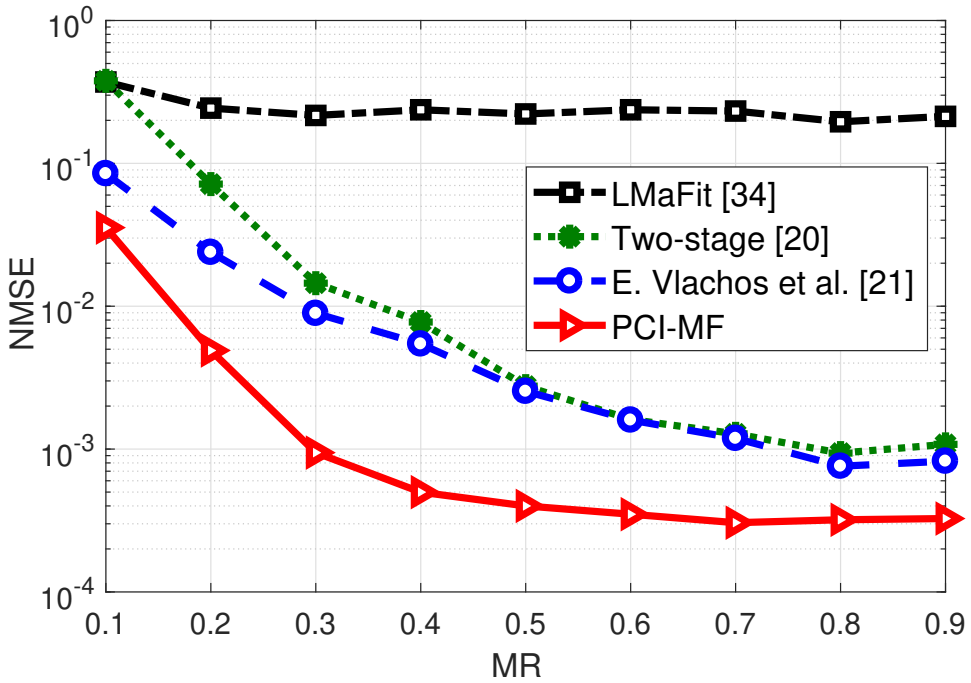

Figure 4.3: NMSE vs MR for ULA at 25 dB SNR with 32×32 MIMO configuration.

Fig. 4.3-4.4 compare the NMSE [8] against the MR for 32×32 and 64×64 MIMO configuration, respectively, with SNR = 25 dB. It is observed that PCI-

[8] NMSE = $\frac{||\mathbf{H}-\mathbf{H}_e||_2^2}{||\mathbf{H}||_2^2}$, where $\mathbf{H}$ and $\mathbf{H}_e$ are the actual and estimated channel matrices, respectively.

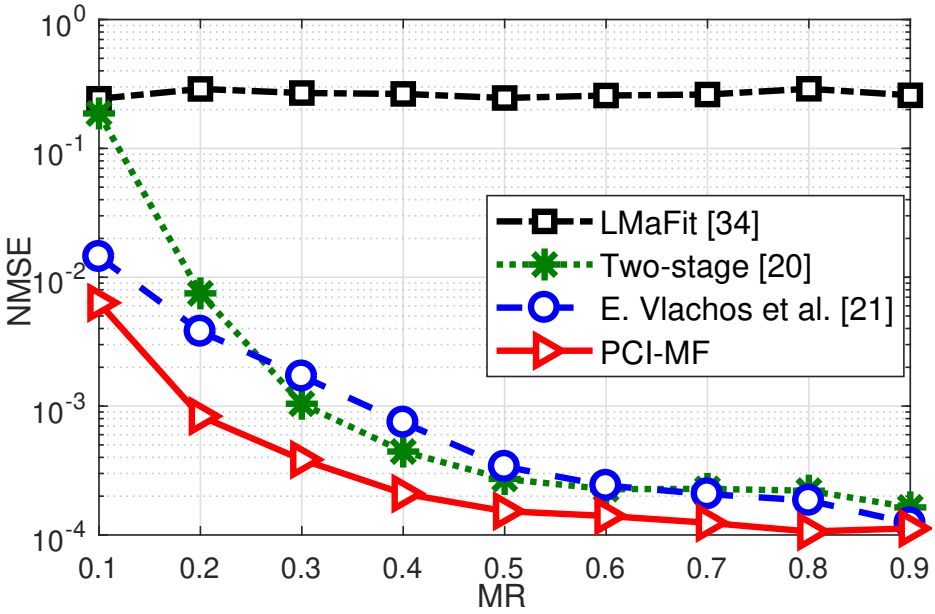

Figure 4.4: NMSE vs MR for ULA at 25 dB SNR with 64×64 MIMO configuration.

MF outperforms all existing methods at all MR ratios and for both MIMO configurations. For instance, for 32×32 MIMO configuration at MR = 0.4, the state-of-the-art methods [20] and [21] yielded NMSE of 7.755×10^{-3} and 5.44×10^{-3}, respectively, as shown in Fig. 4.3. On the other hand, we obtained an NMSE of 0.499×10^{-3} using PCI-MF. Hence, an improvement of $10 \log_{10}\left(\frac{5.44\times10^{-3}}{0.499\times10^{-3}}\right) = 11.91$ dB and 10.375 dB is obtained as compared to [20] and [21], respectively. Similarly, an improvement of 3.22 dB and 5.52 dB is obtained for 64×64 MIMO configuration (Fig. 4.4) with PCI-MF compared to [20] and [21], respectively.

To show the robustness of PCI-MF, we computed NMSE against SNR with only 10% measurement ratio, i.e., MR = 0.1 in Fig. 4.5-4.6 for 32×32 and 64×64 MIMO configuration, respectively. It is observed that PCI-MF outperforms in all the above scenarios. To further validate the proposed work, NMSE is also shown against SNR at MR = 0.5 in Fig. 4.7.

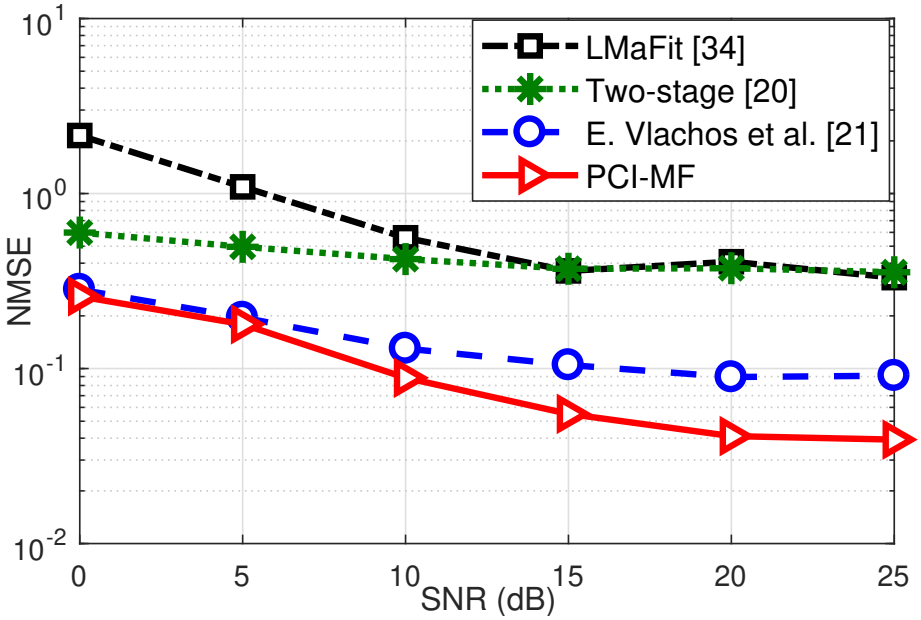

Figure 4.5: NMSE vs SNR for ULA at MR = 0.1 with 32×32 MIMO configuration.

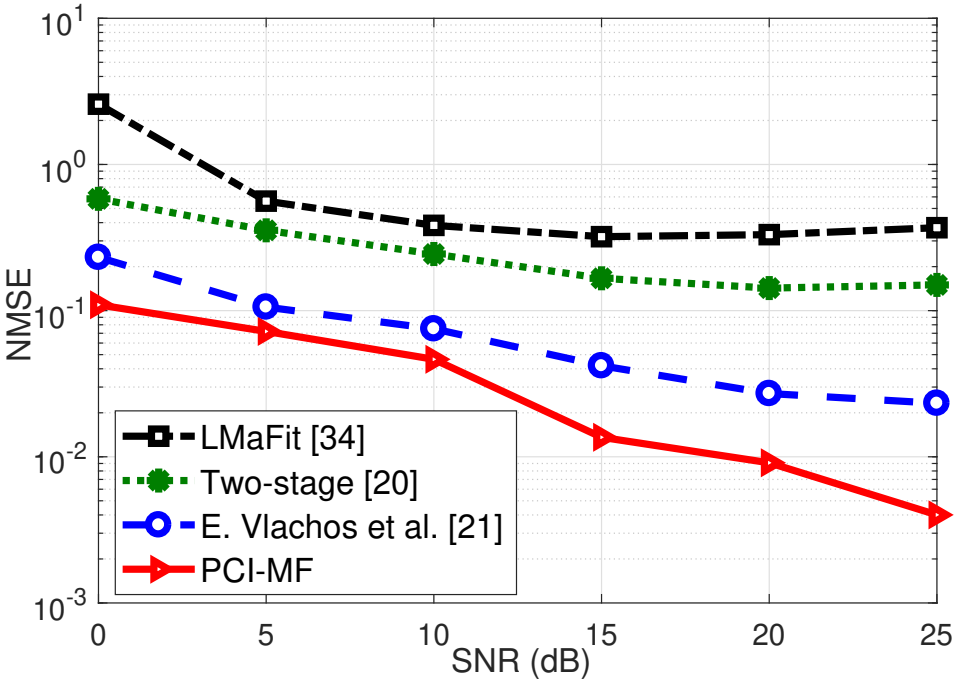

Figure 4.6: NMSE vs SNR for ULA at MR = 0.1 with 64×64 MIMO configuration.

In Fig. 4.8, NMSE is plotted against the number of paths, i.e., L for SNR = 25 dB and MR = 0.1 for 32×32 MIMO configuration. Results demonstrate that the performance of PCI-MF does not degrade even with different values of L.

It may be noted that the error between the estimated CSI and actual CSI will

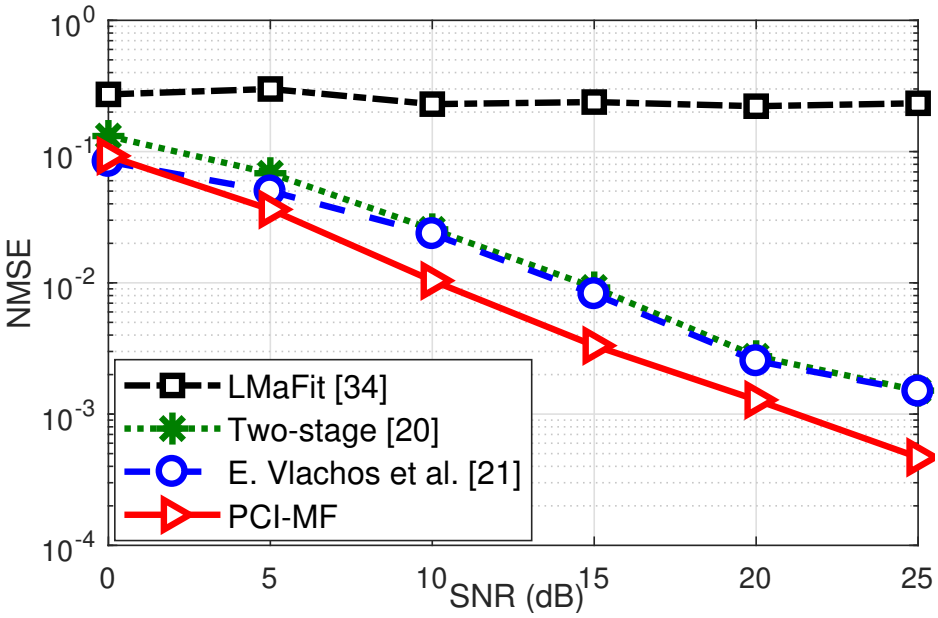

Figure 4.7: NMSE vs SNR for ULA at MR = 0.5 with 32 × 32 MIMO configuration.

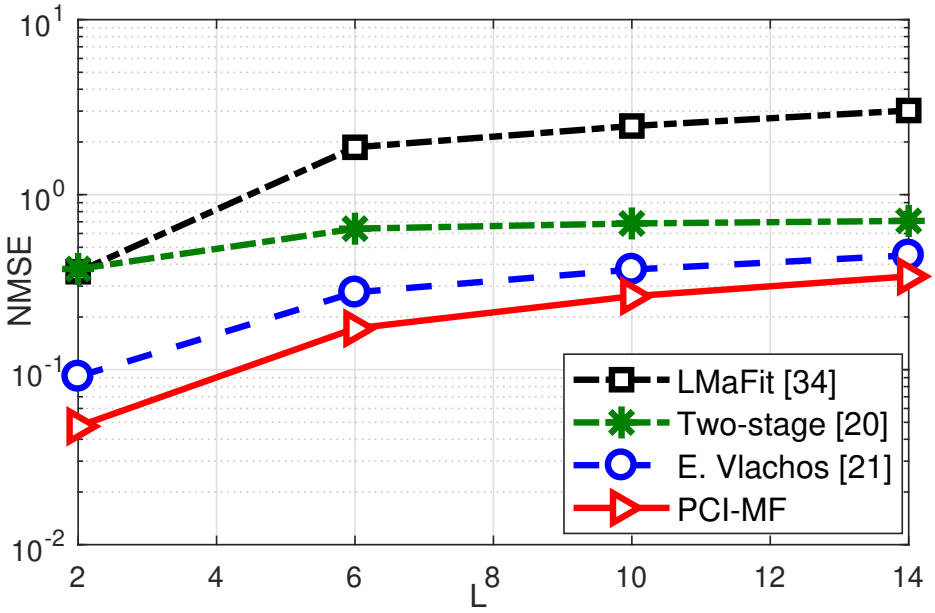

Figure 4.8: NMSE vs L for ULA at SNR = 25 dB, MR = 0.1 with 32 × 32 MIMO configuration.

directly impact the achievable spectral efficiency (ASE) of the wireless system as shown below [21, 87]:

$$ASE = \log_2 \left| I_{N_{\mathrm{R}}} + \frac{1}{N_{\mathrm{T}} N_{\mathrm{R}} \left(\mathrm{NMSE} + \frac{1}{\mathrm{SNR}}\right)} \mathbf{H}\mathbf{H}^H \right| \quad \text{bits/s/Hz.} \tag{4.24}$$

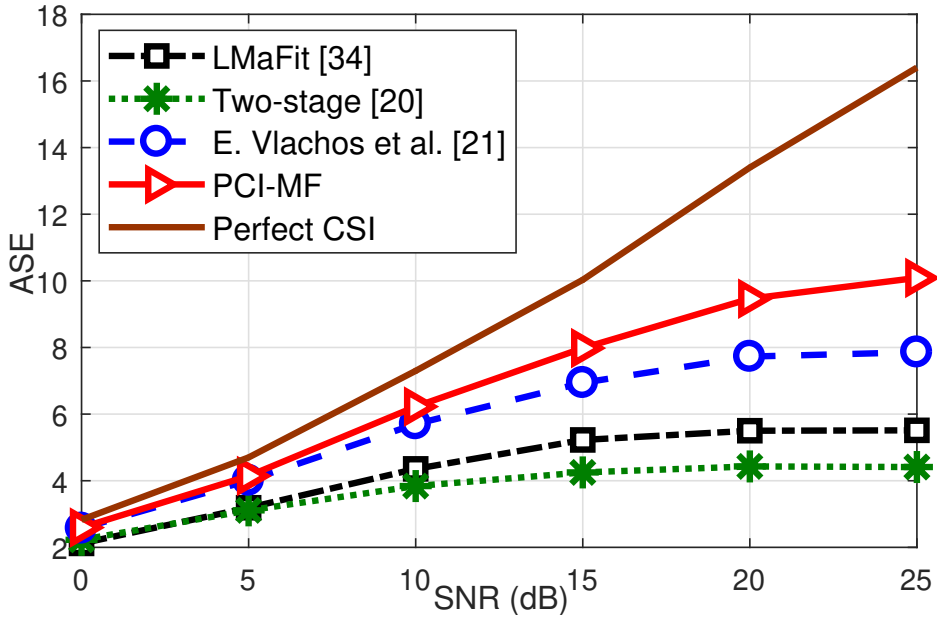

Figure 4.9: ASE vs SNR for ULA at MR = 0.1 with 32×32 MIMO configuration.

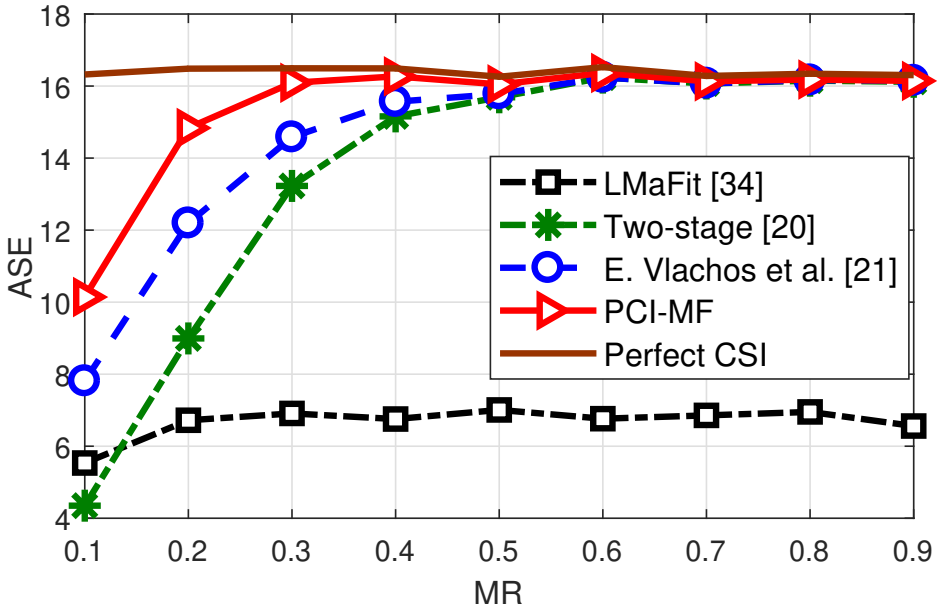

Figure 4.10: ASE vs MR for ULA at SNR = 25 dB with 32×32 MIMO configuration.

Hence, in Fig. 4.9, the ASE is plotted against SNR at MR = 0.1 for 32×32 MIMO configuration. It is observed that at 25 dB SNR, [21] performs best among the existing methods and yields an ASE of 8 bits/sec/Hz. However, the proposed method PCI-MF obtains an ASE equal to 10 bits/sec/Hz. It is noted that the ASE obtained with perfect CSI is nearly 16 bits/sec/Hz. Therefore, in

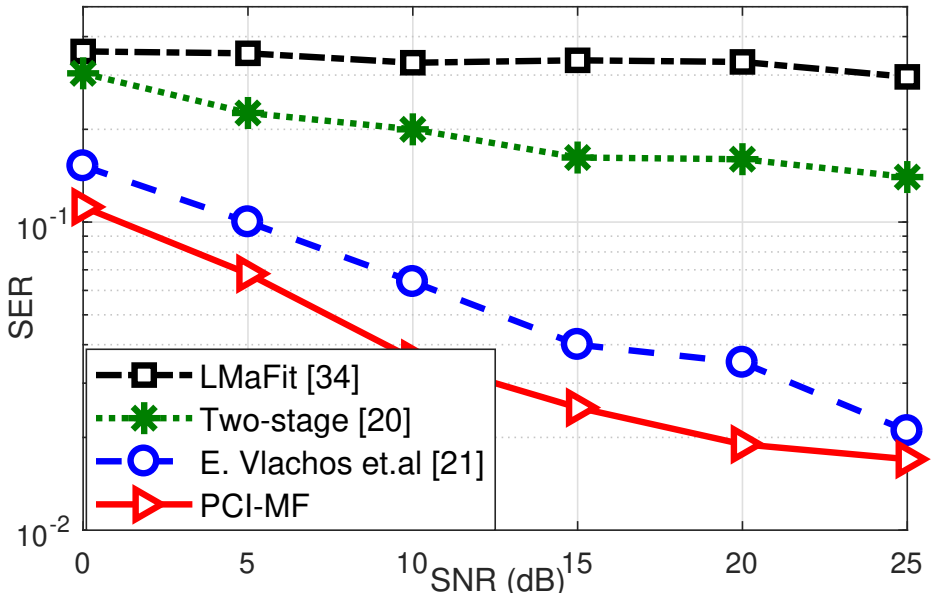

Figure 4.11: SER vs SNR for ULA at MR = 0.1 with 32×32 MIMO configuration.

Fig. 4.10, we have plotted ASE by varying the MR and it is observed that at MR $\geq$ 0.3, PCI-MF approaches close to the ASE value of 16 bits/sec/Hz, i.e., the value obtained with the perfect CSI.

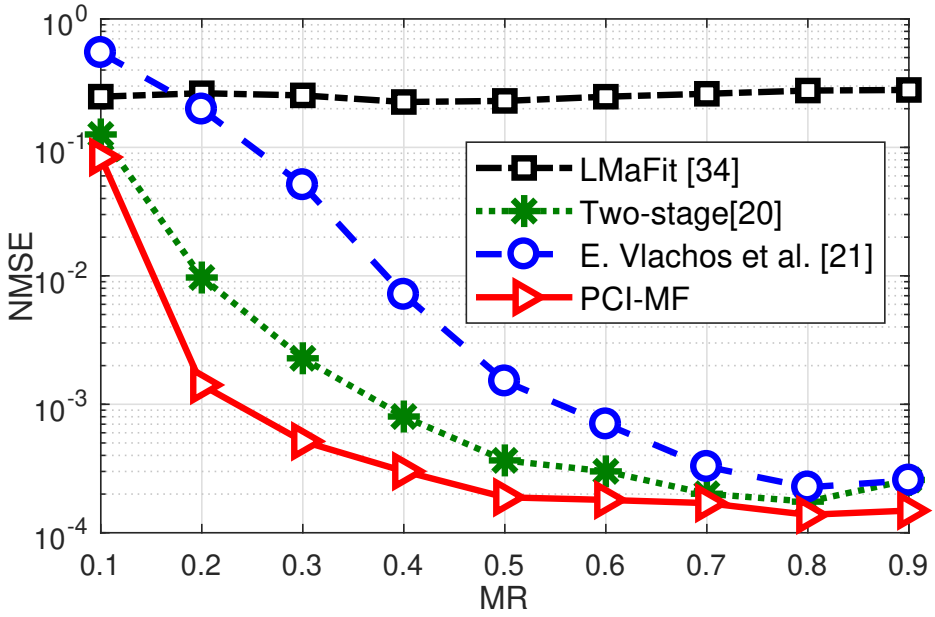

Figure 4.12: NMSE vs MR for UPA at SNR = 25 dB with 64×64 MIMO configuration.

Lastly, we examined the performance of the symbol error rate (SER) of PCI-MF against SNR by comparing it with other algorithms in Fig. 4.11. We mod-

ulated the data for ULA at MR = 0.1 with 32×32 MIMO configuration using BPSK (binary phase shift keying) modulation. The precoding vectors at the transmitter and receiver are implemented using random complex vectors in every iteration.

Fig. 4.12 shows the performance of PCI-MF with UPA. In this plot, NMSE is plotted against MR at 25 dB SNR for 64×64 MIMO configuration, where $N_{\mathrm{Tx}} = N_{\mathrm{Ty}} = N_{\mathrm{Rx}} = N_{\mathrm{Ry}} = 16$. Therefore, it can be concluded that PCI-MF performs better for both ULA as well as UPA.

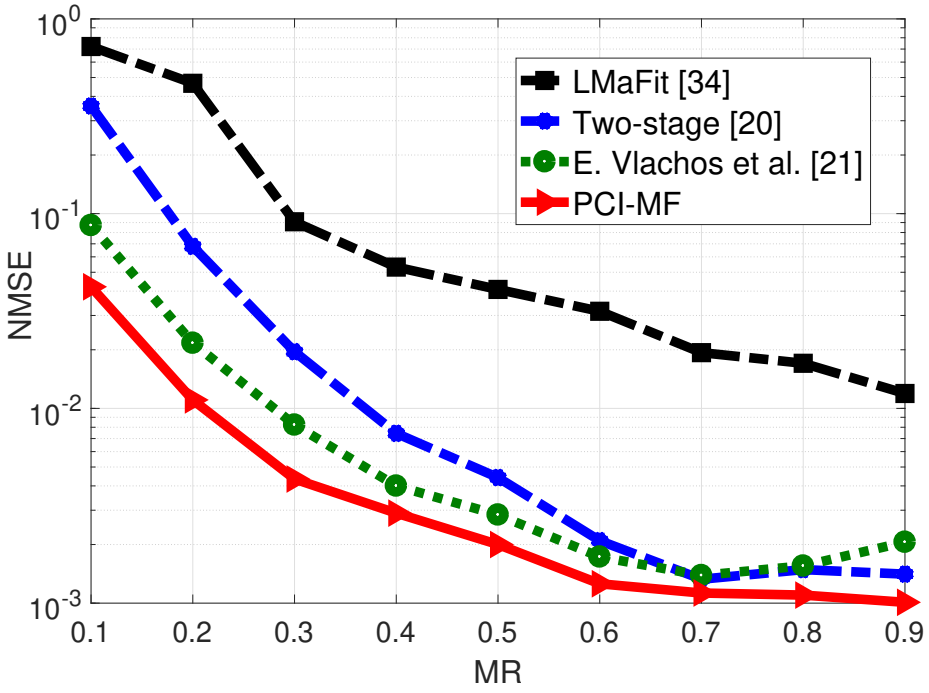

Figure 4.13: NMSE vs MR for ULA at SNR = 25 dB with 32×32 MIMO configuration in Nakagami fading with shape parameter as 0.5.

Fig. 4.13 evaluates the performance of PCI-MF in the presence of Nakagami fading channel. The shape parameter of Nakagami distribution (m) determines the fading channel conditions, for instance $m = 1$ represents Rayleigh fading and $m = 0.5$ represents half Gaussian pulse, which is more severe

than Rayleigh fading [88, 89]. Therefore, in Fig. 4.13, NMSE is plotted for $\mathcal{NG}(0.5, 1)$ against MR at 25 dB SNR. From the plot, it is observed that PCI-MF performs good even with severe fading.

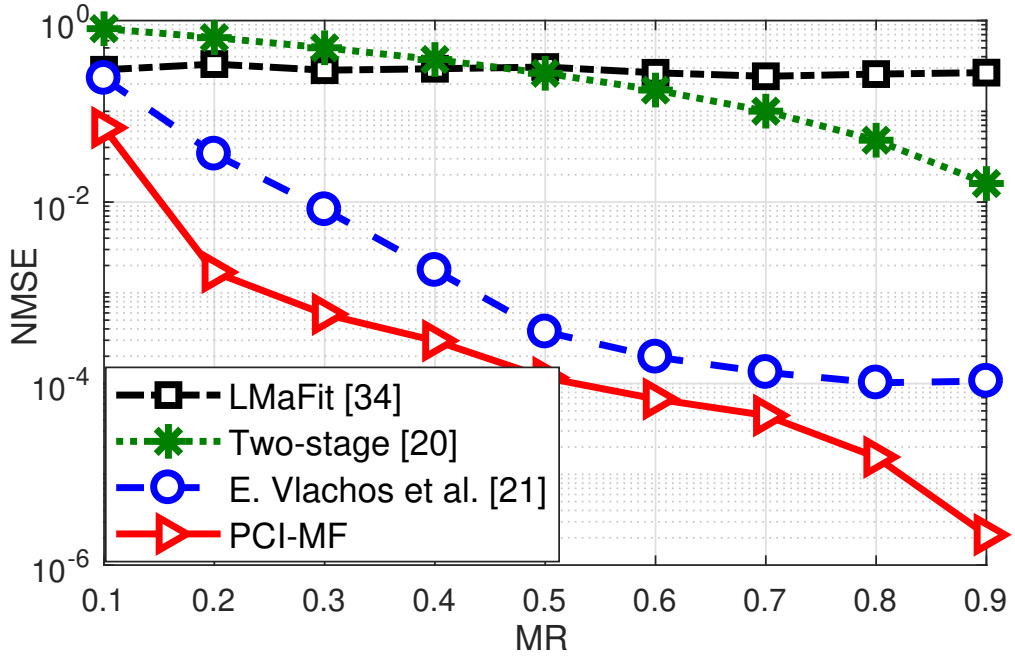

Figure 4.14: NMSE vs MR for realistic data set [2, 3] at SNR = 30 dB with d = 100 m.

Fig. 4.14 shows the results for statistical parameter values derived from real world mmWave outdoor cellular propagation at 28 GHz collected in New York City [2, 3]. As per the collected data, the number of clusters are Poisson distributed with mean value equal to 1.8 and number of dominant paths in each cluster i.e., L_k is assumed to be 2. The AoA and AoD are Gaussian distributed with mean and variance equal to μ_a and σ_a^2, respectively, where μ_a is uniformly distributed between 0 to 2π and σ_a is exponentially distributed with mean λ_a^{-1}. The values of λ_a^{-1} for azimuth AoA, elevation AoA, azimuth AoD and elevation AoD are 15.5, 6, 10.2 and 0, respectively [2, 3] (as summarized in Table II). It considers a UPA with 64×64 MIMO configuration.

The instantaneous path loss is Rayleigh faded with σ_l^2 variance. The variance σ_l^2 for l^{th} path is given as $\sigma_l^2 = \gamma_l 10^{(0.1PL)}$, where $\gamma_l = \frac{\gamma_l'}{\sum_{i=1}^{L}\gamma_l'}$. Furthermore, $\gamma_l' = U_l^{r_\tau - 1} 10^{-0.1Z_l}$, where r_τ is 2.8, $U_l \sim \mathcal{U}(0,1)$ and $Z_l \sim \mathcal{N}(0,16)$. Moreover, $PL = \alpha + 10\beta \log_{10}(d) + \zeta$ dB, where α = 72, β = 2.92 and $\zeta \sim \mathcal{N}(0, 8.7\ \mathrm{dB})$ for non line-of-sight (NLOS) [2, 3]. The distance considered between transmitter and receiver (d_{t-r}) is 100 m. It is observed that for realistic data set the performance of all existing methods except [21] is not acceptable, as they hardly achieve NMSE of 10^{-2} even when 90% data is available. However, NMSE achieved by [21] is 2.952×10^{-5}. Since PCI-MF achieves NMSE of 7.418×10^{-10}, 16.933 dB improvement is obtained as compared to [21].

4.6 Discussion

In this chapter, we have shown PCI-MF can recover the mmWave massive MIMO CSI from a few noisy channel coefficients. The performance of the method has been evaluated by calculating NMSE between the actual CSI and the recovered CSI. NMSE results show considerable improvement in performance with PCI-MF compared to the state-of-the-art methods. For validating the robustness of PCI-MF, the NMSE is simulated with various parameters, such as different MIMO configurations, low and high values of SNR and MR, as well as different channel fading models. It is observed that PCI-MF consistently outperforms the conventional methods for different MIMO configurations such as 32×32, 64×64, for all values of SNR and also for all MR. The improvement

in performance is observed with both ULA as well as UPA antenna configurations. The performance of PCI-MF is also shown by evaluating SER and ASE. It is also observed that PCI-MF approaches the ASE values of perfect CSI. For instance, at 25 dB SNR, ASE of 16.49 bits/sec/Hz is obtained with perfect CSI for 32×32 MIMO configuration. Using PCI-MF, with only 30% availability of channel information, ASE of 16.09 bits/sec/Hz (close to perfect CSI) has been obtained.

In order to validate the performance of PCI-MF in realistic scenarios, another data set of New York City with real-world outdoor cellular propagation parameters has also been considered. It is observed that even in a practical scenario when transmitter and receiver are 100 m apart, PCI-MF obtains 5.45 dB and 16.933 dB improvement with 10% and 90% availability of channel information, respectively, as compared to the existing methods.

Chapter 5

Integrated data and energy gathering for WSN

In Chapter 2 and 3, we have shown PCI-CS framework can tackle various problems of WSN such as efficient data gathering at sensor node, improvement in data reconstruction at FC and also missing data recovery at the FC. This chapter will show how PCI-CS also contributes to energy gathering. This integrated solution is henceforth called integrated data and energy gathering (iDEG) protocol for WSN. The term energy gathering here implies joint energy saving and energy harvesting.

5.1 Background: CS in WSN

Consider a wireless sensor network with of N sensor nodes, where every node transmits its information to either FC [12] or cluster head [40] based upon single-hop and multi-hop WSN respectively. Data of sensor nodes can be rep-

resented as $\mathbf{x} = [x_1, x_2, ..., x_N]'$, where x_i represents the data corresponding to the i^{th} sensor node.

The CS theory provides a better solution for data gathering in WSN by transmitting only M linear projections of $\mathbf{x}$, collected using a random sensing matrix ($\mathbf{\Phi}$), like Gaussian or Bernoulli such that $\mathbf{y} = \mathbf{\Phi x} = \boldsymbol{\phi_1} x_1 + \boldsymbol{\phi_2} x_2 + ... + \boldsymbol{\phi_N} x_N$ where $\boldsymbol{\phi_i}$ is the i^{th} column of $\mathbf{\Phi}$. The original raw data of length N can be recovered at FC by solving the convex optimization problem as given in (2.9). However, traditional CS based data gathering approaches suffer with a few drawbacks: Every i^{th} sensor node generates an $M \times 1$ vector $\boldsymbol{\phi_i}$ by using its network address as the seed of a pseudo-random number generator.[1]. Data collected at each node is multiplied by this vector $\boldsymbol{\phi_i}$ and transmitted [12]. Due to the additive nature of radio waves, the signal received at FC will be

$$\mathbf{y} = \sum_{i=1}^{N} \boldsymbol{\phi_i} x_i = \mathbf{\Phi x}. \tag{5.1}$$

Hence, effectively only M information is transmitted instead of N and hence network traffic will reduce. However, this will also increase the power consumption at the sensor nodes by M. Furthermore, MN multiplications are also required to compressively sense the data, which increase the complexity at the sensor nodes and also cause energy dissipation.

Therefore, [40–42] provided the energy efficient data gathering solutions using CS. Specifically, in [40], a multi-hop, cluster-based CS data collection (CCS) has been proposed, in which CS measurements are generated at each

[1]These seed values are used by FC to generate the complete $\mathbf{\Phi}$ matrix.

cluster head. Cluster head collects the CS measurements within its cluster and transmits it to the FC. As sensor nodes are closer to their cluster head as compared to the FC, hence less power will be consumed while collecting the CS measurements. In [41], a hybrid CS framework is utilized to minimize the energy consumption of WSN by selecting two types of traffic, namely, raw traffic and CS encoded traffic depending on the network capacity and energy requirements. Unlike the conventional data sampling approaches of CS, [42] proposes a multi-hop random walk based algorithm for data gathering in WSNs. In this, few random walks among the nodes are selected, and each random walk will contribute towards one random measurement. The sensor node will transmit its information to the next node on its path, and then the added information is transmitted to the next upcoming node. This process continues until the measurement obtained from the linear combination of the sensors data is transmitted to the FC. This will reduce the communication cost of the nodes as compared to the scenario where every node is transmitting its information to the cluster head or FC. However, multi-hop routing methods such as clustering [40] and random walk [42] also increases the latency at the FC, when compared to single-hop sensor network [12].

In addition to the above methods, significant research has also been devoted towards reducing the energy consumption of the CS framework by reducing the number of measurements [43, 44] or by using a sparse measurement matrix [45–47]. For instance, in [43], a power-law decaying data model and random projection-based estimation algorithm have been proposed for reducing the

compressive measurements. In [44], unlike the conventional CS based data gathering solutions that exploit the assumption of constant sparsity, the regression-based model for WSNs has been proposed, where sparsity of signals is unknown. The algorithm exploits the correlation in the data to determine the sparsity and to reconstruct the data. Hence, a suitable number of measurements are chosen according to the sensed data. In [45], data is collected randomly from a few sensor nodes, unlike the previous work where each measurement is obtained from the linear combination of raw data from all the sensor nodes. They have proposed a representation basis which sparsifies the data. However, it sparsifies the data in the spatial domain only. In [46] non-uniform sampling has been considered based upon heterogeneity. It has been shown that every sensor node has a different amount of energy, and the node that has a higher energy supply should sample more. Hence, a model has been developed which selects those nodes which have high energy supply to recover the data of all nodes. They have also shown their model can achieve good accuracy with the significant reduction in energy consumption. However, this methodology will increase the computation and transmission cost as every node has to share their amount of energy rate with other nodes. This further leads to energy dissipation. [47] proposes a sparsity model that allows the use of CS for the online recovery of large data sets in real WSN scenarios, exploiting Principal Component Analysis (PCA) to capture the spatial and temporal characteristics of real signals. This method is using sub-sampling for compressively sensing the data, PCA for capturing the spatial and temporal characteristics and finally interpolation techniques for

reconstructing the data.

5.2 Proposed iDEG framework

In the proposed protocol, a few M randomly selected sensor nodes from a set of N sensor nodes are used at a time to construct the complete raw data at the FC utilizing PCI-CS framework (discussed in Chapter 2), and the remaining $(N - M)$ sensor nodes harvest the energy from the received signal. To the best of our knowledge, there is no work that provides an approach to harvest energy for the remaining $(N - M)$ sensors owing to the fact that a combination of all the sensor nodes' data is generally required to collect the compressive measurements of the data. Instead, as noticed from above, extra energy is being dissipated in constructing the CS data. This work is aimed at overcoming the above limitations and proposes a joint framework for energy harvesting along with better data recovery in practical WSNs.

5.2.1 Proposed Architecture

Consider the proposed architecture of a sensor node, as shown in Fig. 5.1. In the proposed protocol, single-hop topology has been used, which reduces the latency of the network because sensor nodes directly transmit their data to the FC. Single-hop WSN consists of the transmit-only sensor node and is preferred for applications requiring dense and long-lasting deployment with reduced cost and latency [90]- [91]. In WSN, every node senses some physical condition

and produces an electrical output signal. It is assumed that there are N sensor nodes in the network and M out of N nodes are randomly selected every time to transmit their data to FC. These M nodes pass the electrical output signal to the 1^{st} path shown in Fig. 5.1. Thus, the analog signal of M nodes is converted to a digital output to transmit to the FC for the data reconstruction. The remaining $(N-M)$ nodes, that did not participate in data transmission, pass their electrical analog signal to the 2^{nd} path for harvesting the energy.

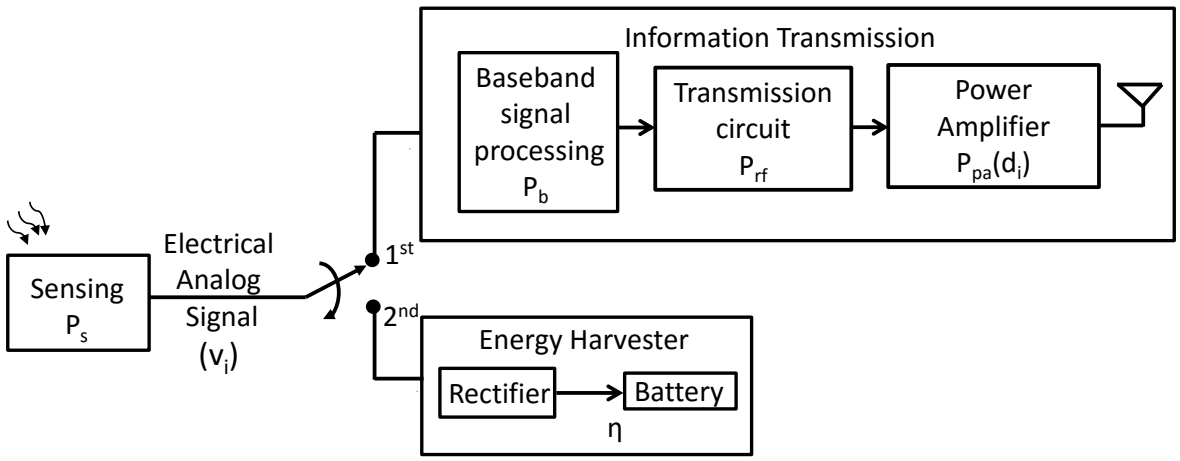

Figure 5.1: The Proposed architecture of a sensor node.

5.2.1.1 Data gathering and reconstruction

Let $\mathbf{y}^{(j)} = [x_1, x_6, ...x_M]'$ denotes the sensor nodes participating in information transmission to FC at time instant (j), which can be written as

$$\mathbf{y}^{(j)} = \begin{bmatrix} 1 & 0 & 0 & 0 & 0 & 0 & ... & 0 \\ 0 & 0 & 0 & 0 & 0 & 1 & ... & 0 \\ \vdots & \vdots & \vdots & \vdots & \vdots & \vdots & ... & \vdots \\ 0 & 0 & 0 & 0 & 0 & 0 & ... & 1 \end{bmatrix}_{M \times N} \begin{bmatrix} x_1^{(j)} \\ x_2^{(j)} \\ x_3^{(j)} \\ x_4^{(j)} \\ \vdots \\ x_N^{(j)} \end{bmatrix}_{N \times 1}$$

$$= \mathbf{\Phi x}, \tag{5.2}$$

where $x_i^{(j)}$ is the data generated at i^{th} sensor node (i=1,2...N) and j^{th} time instant. Further, $\mathbf{\Phi}$ is an $M \times N$ PCI sensing matrix, where each element of $\mathbf{\Phi}$ is given by

$$\Phi(i,j) = \begin{cases} 1 & 1 \leq i \leq \boldsymbol{M}, j = m, \text{where } m \in [1, \boldsymbol{N}] \\ & \text{and all } m \text{ are distinct.} \\ 0 & \text{otherwise.} \end{cases} \tag{5.3}$$

The vector $\mathbf{x}^{(j)}$ can be recovered from $\mathbf{y}^{(j)}$ using single sparsity as shown in Chapter 2. Further, we can also improve the accuracy by jointly reconstructing the data for T time instants ($\mathbf{y}^{(j)}$, $\mathbf{y}^{(j+1)}$,..., $\mathbf{y}^{(j+T-1)}$) while exploiting the double sparsity as shown in Chapter 2.

5.2.1.2 Energy gathering

Energy gathering symbolizes the total amount of energy that can be saved and/or harvested. The amount of power consumed by a sensor node can be divided into two parts: the power consumed in sensing, represented as P_s and the power consumed in transmission, which is given by $P_t = P_b + P_{rf} + P_{pa}$, where P_b is the power consumed in baseband signal processing, P_{rf} is the power consumed in the transmission circuit and P_{pa} is the power consumed by the power amplifier [92].

The power consumed by the power amplifier of a sensor node, i.e., P_{pa} will depend on the distance between the sensor node and the destination node, i.e. the node to which it will transmit the data. In the single-hop network, the destination node is the FC. However, in case of the multi-hop sensor network, the destination node can be the cluster head of a cluster [40] or the adjacent node on the path [42], depending on the selected routing method. Therefore, the power consumed by power amplifier can be given as $P_{pa}(d_i) = \frac{Ad(i)^{\alpha}}{\eta_1} P_{pd}$, where A depends upon the antenna characteristics of sensor node and destination node, d_i denotes the distance between the i^{th} sensor node and the destination node, η_1 represents the drain efficiency of power amplifier, α is the path loss exponent and P_{pd} is the minimum power required at destination to correctly recover the data.

For simplistic comparison, assume the distance between any two adjacent sensor node is d_s and power consumed in transmitting the data from one sensor

node to another is given by

$$P_t^{s-s} = P_b + P_{rf} + \frac{Ad_s^{\alpha}}{\eta_1} P_{pd}. \tag{5.4}$$

Similarly, the distance between a sensor node and the FC is taken as d_f and hence power consumed in transmission is given as

$$P_t^{s-f} = P_b + P_{rf} + \frac{Ad_f^{\alpha}}{\eta_1} P_{pd}. \tag{5.5}$$

Further it is assumed that the time taken in transmitting information between the sensor nodes is T_{s-s}, whereas the time taken in transmitting information from sensor node to the FC is T_{s-f}.

Assume all the sensor nodes are sharing the common frequency band. Therefore, the time taken by a generic single-hop WSN for transmitting the data of N sensor nodes can be computed as NT_{s-f}. In single-hop WSN every node transmits its data to the FC directly. Therefore, the overall power consumed in transmission is given by NP_t^{s-f}. However, after applying conventional CS in single-hop WSN framework [12], N information can be transmitted in M time slots. Therefore, the time taken by the single-hop CS based WSN framework will be MT_{s-f} only. Further, as mentioned earlier in Section 5.1, every node of single-hop CS based WSN framework transmits its data after multiplying it with a basis vector of length M, to obtain M compressive measurements. Therefore, if power dissipated in computing one multiplication is P_{b_m} then the overall

power consumed by a single-hop CS based WSN framework is given by

$$P_{t_{[12]}} = MNP_t^{s-f} + MNP_{b_m}. \tag{5.6}$$

where P_t^{s-f} is defined in (5.5). In order to overcome the drawback of single-hop CS based WSN, multi-hop CS based WSN framework such as clustering, and random routing has been proposed. In clustering [40], the sensor nodes are divided into clusters. In every cluster, one node is selected to work as a cluster head, which receives the data from the sensor nodes of its cluster. Later, cluster heads compute the compressive measurements by utilizing the received data and its own data and transmit the measurements to the FC. If all the sensor nodes are equally divided into k_c clusters, then the power consumption of clustering is given by

$$P_{t_{[40]}} = (N - k_c)P_t^{s-s} + k_c M P_t^{s-f} + \frac{MN}{k_c} k_c P_{b_m} + \left(\frac{N}{k_c} - 1\right) k_c P_{b_a}, \tag{5.7}$$

where P_t^{s-s} is the power consumed in transmitting the data of a sensor node to its cluster head (5.4), P_t^{s-f} is the power consumed in transmitting the data from cluster head to FC (5.5). Further, P_{b_m} and P_{b_a} represents the baseband computation power dissipated in computing one multiplication and one addition, respectively. In random routing [42], a sensor node will transmit its data to the adjacent node on its path and the combined information is transmitted to the next upcoming node and process continues. Finally, the data collected at the last node will be transmitted to the FC. To obtain M measurements, M such paths would be followed by a sensor network. If every path passes through k_r

random nodes, then the power consumption of random routing WSN will be given as

$$P_{t_{[42]}} = M(k_r - 1)P_t^{s-s} + MP_t^{s-f} + M(k_r - 1)P_{b_a}. \tag{5.8}$$

The multi-hop WSN increases the latency of the system. Even if frequency reuse among the clusters are assumed, the time taken by the cluster CS based WSN framework will be $\frac{N}{k_c}T_{s-s} + MT_{s-f}$. Similarly, in random routing method, if all M random paths are followed simultaneously, the time taken by random routing CS based WSN framework is given by $(k_r - 1)T_{s-s} + MT_{s-f}$.

In the proposed iDEG protocol, M nodes will be randomly selected to transmit its data to the FC. Therefore, the time taken in the proposed protocol will be MT_{s-f} only, therefore reducing the latency. Further, the power consumed in the proposed iDEG protocol is given as

$$P_{t_{\text{iDEG}}} = MP_t^{s-f}. \tag{5.9}$$

Please note that energy consumption can be calculated as the product of power consumption with the duration of time for which power is consumed. For instance, the energy consumption of iDEG will be $MP_t^{s-f}T_{s-f}$.

As mentioned above, M out of N nodes were used for the data aggregation. Hence, the remaining $(N - M)$ nodes, that are not participating in information transmission, will harvest energy from the sensed electrical analog signal, as shown in Fig. 5.1. Let's assume, v_i is the average voltage received at the i^{th}

node, therefore the amount of average power harvested at i^{th} sensor node will be given as $P_{h_i} = \eta v_i^2$ W, where η is the efficiency of the harvester circuit. Hence, the amount of energy harvested per slot for a complete WSN by using the iDEG protocol can be given as

$$E_h = \left(\eta \sum_{i=1}^{N-M} v_i^2 \right) T_{\text{slot}} \text{ J}, \tag{5.10}$$

where T_{slot} is the time duration of one slot in seconds. Hence it is evident from the above, the proposed iDEG protocol reduces the latency as well as power consumption and promotes energy harvesting. Table III compares the amount of power consumed and harvested for N sensor nodes for single-hop WSN framework, single-hop CS based WSN framework [12], a multi-hop CS based clustering WSN framework [40], a multi-hop random routing CS based WSN framework [42] and the proposed iDEG WSN.

Based on the above analysis, we have computed the amount of power saved using the iDEG protocol as compared to conventional CS based single-hop and multi-hop WSN frameworks. For instance, the amount of power saved using iDEG protocol, compared to the conventional single-hop CS based WSN framework [12] can be given as

$$P_d^{[12],\text{iDEG}} = P_{t_{[12]}} - P_{t_{\text{iDEG}}} = MP_t^{s-f}(N-1) + MNP_{b_m} \text{ W}. \tag{5.11}$$

The amount of power saved with iDEG as compared to a multi-hop CS based

clustering WSN framework [40] can be given as

$$\begin{aligned} P_d^{[40],\text{iDEG}} &= P_{t_{[40]}} - P_{t_{\text{iDEG}}} \\ &= MP_t^{s-f}(k_c - 1) + (N - k_c)P_t^{s-s} \\ &+ \frac{MN}{k_c}P_{b_m} + M\left(\frac{N}{k_c} - 1\right)P_{b_a} \text{ W}. \end{aligned} \tag{5.12}$$

Simillarly, the amount of power saved with iDEG as compared to a multi-hop random routing CS based WSN framework [42] can be given as

$$\begin{aligned} P_d^{[42],\text{iDEG}} =& P_{t_{[42]}} - P_{t_{\text{iDEG}}} \\ =& M(k_r - 1)P_t^{s-s} + M(k_r - 1)P_{b_a} \text{ W}. \end{aligned} \tag{5.13}$$

Table 5.1: Power consumed and power harvested in a WSN of N sensor nodes with different methods.

Different WSN frameworks	Required time	Transmit power consumption (W)	Power harvested (W)
Single-hop	NT_{s-f}	NP_t^{s-f}	0
Single-hop CS [12]	MT_{s-f}	$MNP_t^{s-f} + MNP_{b_m}$	0
Clustered [40]	$\frac{N}{k_c}T_{s-s} + MT_{s-f}$	$(N - k_c)P_t^{s-s} + k_cMP_t^{s-f}$ $+MNP_{b_m} + M(N - k_c)P_{b_a}$	0
Random routing [42]	$(k_r - 1)T_{s-s} + MT_{s-f}$	$M(k_r - 1)P_t^{s-s} + MP_t^{s-f}$ +M$(k_r - 1)P_{b_a}$	0
Proposed:iDEG	MT_{s-f}	MP_t^{s-f}	$\eta \sum_{i=1}^{N-M} v_i^2$

5.3 Simulation Results

In this section, the amount of energy that could be gathered by using iDEG protocol has been shown. As mentioned above, energy gathering refers to the total amount of energy that could be saved and harvested. For simulation, the

distance between the sensor nodes i.e., d_{s-s} is assumed to be 3 m. Further, the distance between sensor node and FC i.e., d_{s-f} is considered to be 100 m. The remaining parameter values are given as $P_{t0} = P_b + P_{rf} = 20\mu$ W, $\eta_1 = 0.7$, $\alpha = 2$, $A = 1$, $P_{pd} = 0.05$mW and $\eta = 0.7$. Further, k_c and k_r is assumed to be 4 and 25. The value of v_i at each sensor node can be calculated by using standard temperature and voltage relationship, i.e., $v_i = \frac{KT_i}{q}$, where K is the Boltzmann constant (1.38064852 $\times 10^{-23}$m^{2}kg s^{-2}K^{-1}), T_i is the temperature obtained at i^{th} sensor node [1] in Kelvin and q is the charge of an electron (1.60217662 $\times 10^{-19}$ coulombs). This implies at temperature value of 19.9002 °C, the obtained voltage will be $v_i = (19.9002 + 273)/11600 = 0.0253$V. The temperature value is taken from [1] [2].

The amount of power saved using the proposed iDEG protocol as compared to conventional CS based single-hop, $P_d^{[12],\text{iDEG}}$ (5.11) and multi-hop WSN frameworks such as clustering, $P_d^{[40],\text{iDEG}}$ (5.12) and random routing, $P_d^{[42],\text{iDEG}}$ (5.13) with respect to sampling ratio $(\frac{M}{N})$ have been plotted in Fig. 5.2. From the graph, it can be observed that the proposed iDEG protocol saves a considerable amount of power as compared to conventional CS based WSN frameworks. Further, in this graph, we have also plotted the amount of power that can be harvested for $N = 52$ sensor nodes. It can also be observed that as sampling ratio increases, the amount of power harvested decreases, and the amount of power saved increases because of the participation of more sensor nodes in the data gathering process. Please note that in the proposed analysis we have neglected

[2] Same as chosen in Chapter 2.

the extra computational power consumed in computing P_{b_m} and P_{b_a} for obtaining the compressive measurements in conventional frameworks, i.e. $P_{b_m} = 0$ and $P_{b_a} = 0$ otherwise, the performance of the conventional frameworks would further deteriorate.

In Fig. (5.3), the total amount of energy harvested for iDEG protocol with $N = 52$ sensor nodes, $T = 500$ time slots of duration 1 minute (i.e. $T_{\text{slot}} = 1$ min) each has been plotted with respect to sampling ratio $(\frac{M_e}{N_T})$, where M_e will be the number of samples picked from N_T for data gathering. For instance, sampling ratio of 0.5 implies $M_e = 50\%$ of N_T samples are used for data gathering and remaining time can be used for energy harvesting.

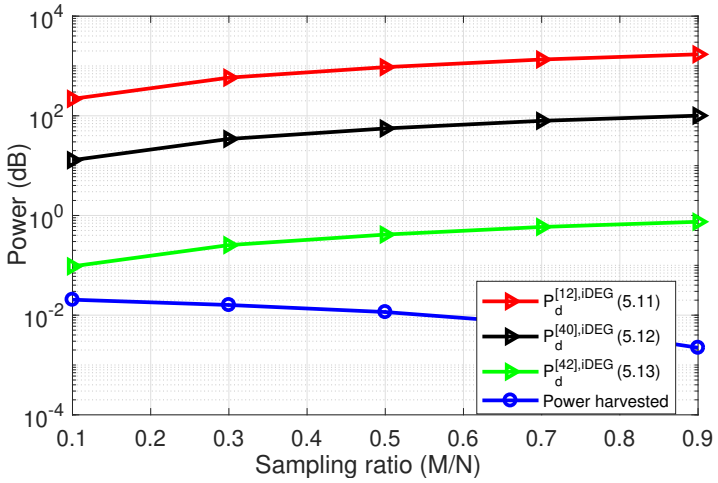

Figure 5.2: Power harvested and saved using the proposed iDEG protocol

5.4 Discussion

In this work, a methodology has been proposed (named as 'iDEG') to harvest the energy from the information signal at the sensor node without affecting the system performance. It can be understood as: only a fraction of signal portion

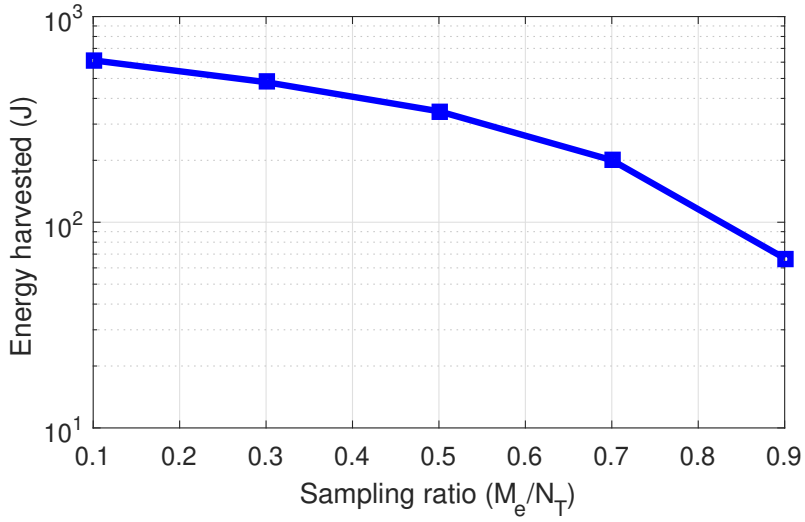

Figure 5.3: Energy harvested in the proposed iDEG protocol

has been utilized for the information transmission, as PCI-MF can be utilized at the FC to recover the entire information, and the remaining signal has been used for the energy harvesting. This motivated us to rethink the conventional sampling process, in which the input analog signal is acquired only for a small fraction of time in every sampling interval for discrete conversion. Hence, in the subsequent chapter, we will propose a method of harvesting the energy from the un-utilized input analog signal without affecting the data acquisition accuracy of the conventional sampling process.

Chapter 6

*e*Sampling: Energy Harvesting ADCs

6.1 Introduction

Physical signals are analog in nature, taking values in continuous sets over a continuous time interval. In order to process and extract information from such signals using digital hardware, they must be accurately represented in digital form. Analog-to-digital converters (ADCs) thus play an important role in digital signal processing systems [7]. ADCs are typically a major source of energy consumption, as their power dissipation grows with the sampling rate and the quantization resolution, and thus their ability to accurately represent the acquired signal is typically limited by the available power [93]. Nowadays, ADCs are utilized in a multitude of energy-limited systems, including communication devices [94], wireless sensors [95], and medically implanted devices [96]. Therefore, there is a growing need for ADCs that are capable of reliably acquiring signals while consuming low power.

The existing strategies proposed in the literature to facilitate energy efficient acquisition of analog signal can be divided broadly into two categories. First, those taking a signal processing approach, and second techniques focusing on circuit level design. Signal processing approaches typically aim for allowing the ADC to operate at reduced sampling rate and quantization resolution by accounting for how the acquired signal is processed and on the basis of the prior information on the signal itself [95, 97–100]. Additionally, in scenarios where the signal is acquired for some task, i.e., to recover some underlying information, it was recently shown that the desired information could be accurately recovered from the output of low-resolution ADCs by properly designing the acquisition system [101–104]. An alternative signal processing oriented method which does not limit the rate and resolution of ADC is based on acquiring a portion of the analog signal for information decoding while utilizing the remaining part for energy harvesting. This strategy, typically studied in the context of communication receivers as simultaneous wireless information and power transfer (SWIPT), considers time or power splitting of the analog signal [105–108]. However, it induces some inevitable loss on the system performance as only a portion of the signal is converted into a digital representation. These aforementioned signal processing methods typically focus on the signal model and the task for which it is acquired, without accounting for the ADC circuitry.

Circuit level methods rely on the hardware architecture of ADC devices. The circuit level approach generally considers designing energy efficient ADC circuitry, which is capable of operating with reduced power consumption. This

can be achieved by reducing the circuit power supply [96] and/or limiting the operating frequency [109] in order to reduce the overall power consumption. An alternative technique is to modify the circuit components in existing ADC architectures and combine various designs in the acquisition, such as sample-and-hold (S/H) ADCs, flash ADCs, sigma-delta ADCs, and time-interleaved ADCs, to improve their energy efficiency, see, e.g., [110–113]. Such circuit-oriented designs which focus on the hardware aspects of acquisition, do not account for the model of the analog signal and the task for which it is acquired.

A popular power efficient ADC is the S/H based successive approximation register (SAR) architecture, which is capable of operating at high resolution and a small form factor with relatively low power consumption [114]. The power consumption of SAR ADCs can be further reduced by incorporating energy efficient switching schemes, as proposed in [115, 116]. In S/H architectures, the circuit used to sample the input analog signal consists of two phases, *acquisition phase* and *hold phase* in each sampling period. In the acquisition phase, the S/H circuit tracks the input analog signal. The sampled value captured in the acquisition phase is then converted into digital form, i.e., a sequence of bits, during hold phase. Therefore, during the sampling process of S/H ADCs, the input signal is processed only for a fraction of the overall sampling period (acquisition phase) and neglected/discarded for the remaining time interval (hold phase) [117, 118]. The fact that the signal is not accessed in a dominant portion of the sampling period, motivates the extension of S/H ADCs, and particularly S/H SAR ADCs, to continuously utilize the analog signal in order to mitigate

power consumption.

In this work, we combine signal processing tools with circuit level methods to propose an *eSampling ADC*, which harvests energy from the acquired signal while converting it into a digital representation. The *e*Sampling ADC builds upon the S/H ADC architecture while introducing an additional energy harvesting circuit. In the resulting architecture, the signal is harvested during hold phase, i.e., when it is not utilized in conventional S/H ADCs. As opposed to SWIPT systems, in which the overall operation of the system is modified to allow energy harvesting while conventional ideal ADCs are assumed [108], *e*Sampling exploits the inherent property of ADC devices to harvest energy as a natural byproduct of their hardware architecture. This makes *e*Sampling an attractive technology which can be easily incorporated into existing devices.

Our theoretical study of *e*Sampling ADCs analyzes its potential in terms of the ability to harvest energy while maintaining a desired accuracy of signal reconstruction. To that aim, we focus on the acquisition of stationary random processes and characterize the resulting tradeoff between the ability to accurately reconstruct the signal from its samples and the energy harvested from it, referred to henceforth as the *energy-fidelity tradeoff*. Our analysis identifies how to set the sampling rate to optimize this tradeoff when operating under energy constraints or fidelity restrictions on the reconstruction. The results allow us to numerically characterize the maximal accuracy in which any signal can be *e*Sampled using only harvested energy, i.e., without requiring any energy from its power source. Our numerical results demonstrate that *e*Sampling ADCs are

capable of fully reconstructing bandlimited signals with zero distortion while harvesting at least as much energy as they consume. In particular, we show that an *e*Sampling ADC with 12 bits quantization can acquire a bandlimited signal with flat power spectral density (PSD) at the Nyquist rate while harvesting more energy than it consumes.

We then proceed to illustrate the hardware feasibility of such a device. To that aim, we design the circuitry of an *e*Sampling 8-bit SAR ADC which samples at 40 MHz on 65 nm complementary metal oxide semiconductor (CMOS) technology, and provide guidelines for setting its parameters to achieve a desired amount of harvested energy. The experimental evaluation of the *e*Sampling SAR ADC circuit, carried out on Cadence Virtuoso platform, shows that the amount of energy harvested is much larger than the amount of energy consumed during the conversion procedure. This is achieved without affecting the signal reconstruction accuracy when acquiring a bandlimited signal while satisfying Nyquist condition. Our experiment indicates that the theoretical potential of *e*Sampling can be translated into an actual ADC device, which accurately acquires analog signals while harvesting more power than it consumes.

The *e*Sampling ADCs have potential advantage in the IoT based applications. This is due to the fact that most of the link sensor nodes with IoT are energy constrained nodes and generate an analog signal corresponding to the sensed parameter. This analog signal is converted into digital bits by using the sampling and quantization process. Hence, by replacing sampling with *e*Sampling, the discarded energy of the analog signal could be harvested to develop a self-

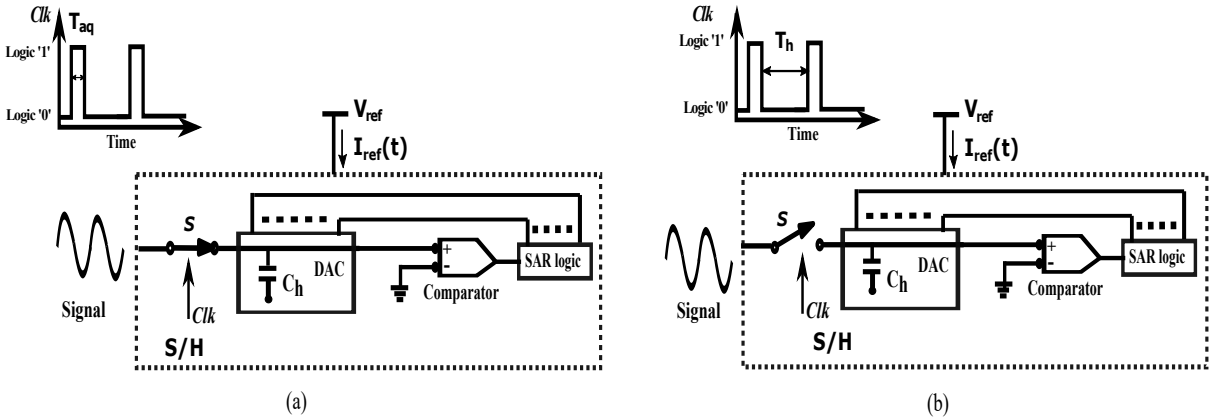

Figure 6.1: S/H SAR ADC illustration: (a) acquisition phase (b) hold phase.

sustainable sensor node. To experimentally demonstrate that energy harvesting can be combined with sampling, we have provided a real-time validation of *e*Sampling ADC for sensing circuit for environmental and health monitoring application.

The rest of this chapter is organized as follows: In Section 6.2, we present our *e*Sampling system model. Section 6.3 analyzes the associated energy-fidelity tradeoff. The circuit-level design is presented in Section 6.4. Section 6.5 details experimental study of the *e*Sampling ADC. Section 6.6 provides real-time validation of *e*Sampling ADC by demonstrating it on an actual hardware for sensing node application.

6.2 System Model

In this section, the proposed ADC model has been discussed from a high-level perspective. We begin by briefly reviewing S/H-based SAR ADCs and their associated energy consumption in Subsection 6.2.1. Then, we present how S/H

ADCs can be extended into *e*Sampling ADCs which harvest energy in addition to signal acquisition in Subsection 6.2.2.

6.2.1 Sample-and-Hold ADC Model

In this section, we briefly reviewing the S/H-based SAR ADCs and also their associated energy consumption.

6.2.1.1 High-level description

S/H is a common ADC architecture. Such ADCs acquire each sample in two phases, determined by a switch S, as illustrated in Fig. 6.1: In the acquisition phase, the signal is connected to a capacitor referred to as a holding capacitor, $C_{\rm h}$, which is charged to the input analog voltage, as depicted in Fig. 6.1(a). The time required by $C_{\rm h}$ to charge to the input voltage, which dictates the acquisition time, is given by [114]

$$T_{\rm aq} = \alpha_\tau R_{\rm on} C_{\rm h}, \tag{6.1}$$

where $R_{\rm on}$ is the on-resistance of the switch S, and α_τ is the number of time constants, i.e., $R_{\rm on}C_{\rm h}$ required for the capacitor to be fully charged.

Once the acquisition phase is over, the hold phase begins, in which the discrete sample, i.e., the voltage stored in the holding capacitor, is quantized into digital bits. During hold phase, whose duration is denoted by $T_{\rm h}$, the input signal is disconnected from the S/H circuit and $C_{\rm h}$ holds the acquired voltage to

accomplish the successful conversion of the acquired sample into digital bits as illustrated in Fig. 6.1(b). Both T_{h} and C_{h}, must be set to allow the quantization circuit of the ADC to complete the conversion.

When the quantizer is based on SAR logic, the overall architecture is referred to as a SAR ADC. An n-bit SAR ADC consists of a comparator, digital-to-analog converter (DAC), and an SAR logical circuit which successively refines the digital representation. To allow successful quantization into n bits, the hold time required to quantize each sample must satisfy [118]

$$T_{\mathrm{h}} \geq n\alpha_{\tau} R_{\mathrm{q}} C_{\mathrm{h}}, \tag{6.2}$$

where R_{q} is the equivalent resistance of the quantizer binary scale switches. Therefore, the sampling period, i.e., the duration of acquiring a single sample, is lower bounded by the following expression

$$T_{\mathrm{s}} = T_{\mathrm{aq}} + T_{\mathrm{h}} \geq (R_{\mathrm{on}} + nR_{\mathrm{q}})\alpha_{\tau} C_{\mathrm{h}}. \tag{6.3}$$

In S/H SAR ADCs, the on-resistance of the switch R_{on} is commonly not larger than the resistance of the quantizer binary scale switches R_{q}. Thus from (6.1) and (6.2), it is evident that T_{h} is typically much larger than T_{aq}, particularly when using high resolution quantizers, such as ADCs with $n \geq 8$ bits. Consequently, the input signal, which is tracked only during the acquisition phase, is discarded during most of the sampling period.

6.2.1.2 Energy consumption

In general, the energy consumption of a circuit is typically a function of the time duration it is active, and the amount of power drawn from the supply, denoted here by V_{ref}. As T_{h} is typically much larger than T_{aq}, most of the energy required by S/H SAR ADCs is consumed during hold phase [115, 118].

In particular, the only energy consumed during acquisition phase, denoted E_{aq}, is that needed to toggle the sampling switch S. In contrast the energy consumption during hold phase, denoted E_{hold}, is comprised of the energy used by each of the components taking part in the quantization:

$$E_{\text{hold}} = E_{\text{DAC}} + E_{\text{c}} + E_{\text{sl}}, \tag{6.4}$$

where E_{DAC}, E_{c}, and E_{sl} are the energy consumption of the DAC array, comparator, and SAR logic, respectively, resulting in E_{hold} effectively representing the power consumed per sample by S/H SAR ADCs [115, 118]. We elaborate on the quantities in (6.4), which are dictated by the specific circuit parameters used, in Section 6.4 where a concrete circuit-level design is discussed. Here, we note that E_{hold} typically takes the form of a second-order polynomial in the reference voltage V_{ref} [119], i.e.,

$$E_{\text{hold}} = a_1(n)V_{\text{ref}} + a_2(n)V_{\text{ref}}^2. \tag{6.5}$$

The coefficients $a_1(n)$ and $a_2(n)$ in (6.5) are positive constants determined by the number of bits n and the quantization circuit parameters, and can grow dra-

matically with n. This makes energy consumption a major bottleneck of high resolution ADCs, motivating the proposed *e*Sampling architecture detailed next.

6.2.2 *e*Sampling ADC Architecture

As mentioned above, during hold phase, the capacitor C_{h} holds the acquired voltage sample, which is converted into a set of digital bits. In this interval, the input signal is disconnected from the circuit by the switch S. In order to mitigate the energy consumption of S/H SAR ADCs without modifying their sampling and quantization procedure, we propose to harvest the input signal energy by connecting it to an energy harvesting circuit during the hold phase, as illustrated in Fig. 6.2. Henceforth, the proposed architecture is referred to *e*Sampling ADC.

As depicted in Fig. 6.2, the energy harvesting capability is enabled by passing the signal observed during hold time through a conditioning circuit, whose output is used to charge the energy harvesting capacitor C_{EH} to a voltage level V_{EH}. The energy harvesting circuit can be designed using passive elements, as we do in our proposed design detailed in Section 6.4. Hence, no external power supply is required [120]. The purpose of the signal conditioning circuit used in energy harvesting devices is to facilitate the storage of the energy of the signal in the capacitor C_{EH} [121–123]. For instance, a rectifier can act as a signal conditioning circuit, reducing fluctuations in the amount of energy harvested in the presence of alternating signals. Similarly, voltage regulator circuits and DC-DC step up converters can also be used to enhance the overall efficiency of the en-

ergy harvesting circuit [124]. The common measure for the quality of an energy harvesting circuit is the efficiency parameter, denoted by $\eta \in [0, 1]$, which represents the fraction of the energy of the input signal is harvested. Finally, in order to connect the input signal to the quantization circuit during acquisition time and to the energy harvesting circuit during hold time, the sampling switch S is replaced by a two-way switch $\tilde{S}$. The circuit design of $\tilde{S}$ has been explained in Section 6.4.

The amount of energy consumed in acquisition phase as given in (6.5) is dictated by the design parameters of the circuitry, which also affect the sampling rate via (6.3). In particular, the sampling duration is the sum of the acquisition time T_{aq} and the hold time T_{h}. Further, the amount of time during which energy is harvested from the input signal per sampling period is at most T_{h}. Recalling that typically $T_{\mathrm{h}} \gg T_{\mathrm{aq}}$, a significant portion of the sampling interval can be allocated for harvesting energy from the input signal. Since energy is only harvested during hold time, in which conventional S/H ADCs do not utilize the analog signal, the ability to harvest energy in *e*Sampling ADCs *does not affect the acquisition operation*. Specifically, for a given sampling rate, *e*Sampling ADCs implement the same conversion mapping as standard S/H ADCs operating at the same rate. Nonetheless, *e*Sampling provides the ability to trade acquisition accuracy for harvesting more energy. This is due to the fact that increasing the sampling interval, though may degrade the reconstruction of the analog signal, allows *e*Sampling ADCs to dedicate more time to energy harvesting. The theoretical potential benefits of such an architecture, which is capable

of simultaneously acquiring analog signals into a digital form while harvesting their energy, is studied in the following section.

6.3 *e*Sampling ADC Analysis

In this section, we analyze the capabilities of the proposed *e*Sampling ADC in terms of the amount of energy one can harvest while meeting a given level of reconstruction accuracy, as well the achievable accuracy for harvesting a desired amount of energy. The interplay between these key performance measures is determined by the selection of the sampling rate, as we show in the following. We begin by formulating the signal model under which our analysis is carried out and the corresponding problem of characterizing the associated energy-fidelity tradeoff which arises from the *e*Sampling ADC paradigm in Subsection 6.3.1. Then, we derive the achieved normalized mean-squared error (NMSE) under the considered model in Subsection 6.3.2. The derived NMSE is used to characterize the energy-fidelity tradeoff in Subsection 6.3.3, and to obtain as a special case the maximal amount of energy which can be harvested when sampling a bandlimited signal at a rate satisfying Nyquist condition, i.e., allowing perfect recovery. Finally, we discuss the pros and cons of *e*Sampling ADC in light of our analysis in Subsection 6.3.4.

6.3.1 Problem Formulation

The *e*Sampling ADC detailed in Subsection 6.2.2 harvests energy during hold phase. This implies that more energy can be harvested by increasing the hold time, which in turn increases the sampling period, potentially degrading the ability to reconstruct the signal from its samples. Therefore, to unveil the potential of *e*Sampling ADCs, we first wish to analyze the fundamental tradeoff between the amount of energy harvested in *e*Sampling and the resulting fidelity in signal reconstruction. We are particularly interested in quantifying the maximum amount of energy that could be harvested without compromising the signal reconstruction accuracy.

In the analysis carried out in this section we consider a stochastic input signal $x(t)$ modeled as a zero-mean wide sense stationary (WSS) process, with variance σ_x^2, and PSD $S_x(f)$. The signal $x(t)$ is sampled uniformly with sampling interval T_s, resulting in the discrete-time signal $x(kT_\mathrm{s})$, $k \in \mathcal{Z}$, where $\mathcal{Z}$ is the set of integers. The sampled series is quantized with n bits per sample into the digital sequence $\tilde{x}(kT_\mathrm{s})$. The digital representation is used to recover the analog signal $x(t)$ using a linear reconstruction filter $G(t)$, which is designed to the mean square error between $x(t)$ and the recovered signal $\hat{x}(t)$ as in [100, 125]. The reconstructed signal is

$$\hat{x}(t) = \sum_{k \in \mathcal{Z}} G(t - kT_\mathrm{s}) \tilde{x}(kT_\mathrm{s}). \tag{6.6}$$

The overall system is illustrated in Fig. 6.3.

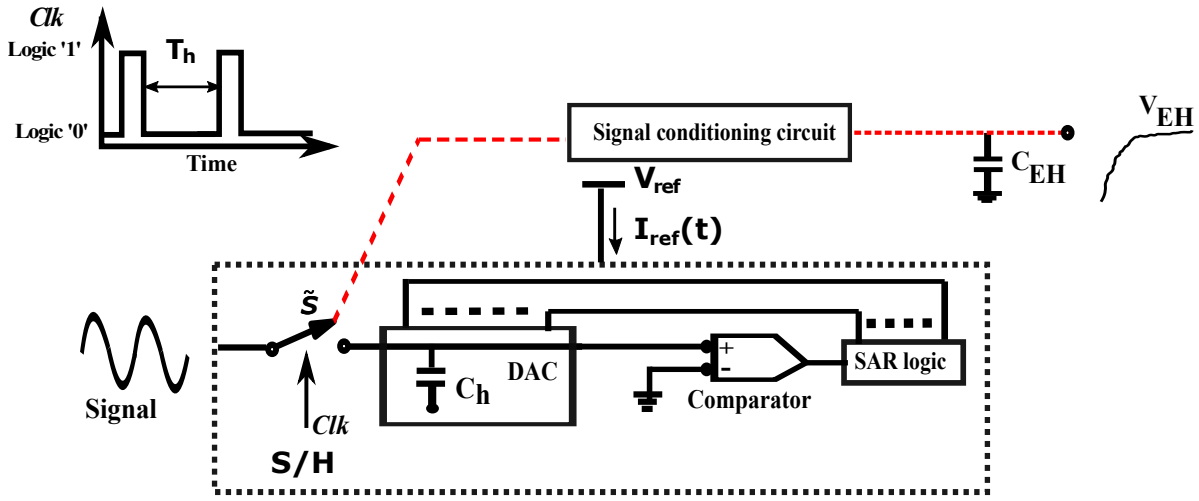

Figure 6.2: Proposed *e*Sampling ADC system model.

The NMSE in reconstructing $x(t)$ from $\hat{x}(t)$ is given by

$$\zeta = \frac{1}{\sigma_x^2 T_{\rm s}} \int_0^{T_{\rm s}} \{|x(t) - \hat{x}(t)|^2\} dt, \tag{6.7}$$

where $\{\cdot\}$ is the stochastic expectation. The amount of expected energy harvested per sampling period is given by

$$E_{\rm h} = \eta \frac{1}{R_{\rm h}} \int_{T_{\rm aq}}^{T_{\rm s}} \{|x(t)|^2\} dt = \frac{\eta}{R_{\rm h}} T_{\rm h} \sigma_x^2, \tag{6.8}$$

where η and $R_{\rm h}$ is the efficiency and the resistance of the energy harvesting circuit, respectively. As mentioned above, the energy harvesting circuit is comprised of passive elements, and does not require an external power source. Therefore, the overall energy consumption per sample using the proposed *e*Sampling ADC can be given as $E_{\rm aq} + E_{\rm hold} - E_{\rm h}$ as illustrated in Fig. 6.3. Recalling that the overall energy consumption is typically dominated by the energy used during hold phase, i.e., $E_{\rm aq} \ll E_{\rm hold}$, and hence the ratio of the amount of energy harvested to the energy consumption per sample can be approximated

as $E_{\text{ratio}} = \frac{E_{\text{h}}}{E_{\text{hold}}}$. The value of E_{hold} is dictated by the power supply voltage V_{ref} and the number of quantization bits n, as well as the SAR architecture and circuit parameters, as we show for our design detailed in Section 6.4.

In the following subsections, we study the fundamental tradeoff between the reconstruction accuracy, modelled as the NMSE, and the portion of the energy consumed in analog-to-digital conversion to that harvested by *e*Sampling, referred to as the *energy-fidelity tradeoff*. To trade energy efficiency for fidelity, we modify the sampling rate for a fixed quantization resolution n and fixed acquisition time T_{aq}. The reconstruction accuracy can be improved by increasing the sampling rate, however *e*Sampling ADC will harvest less energy, and hence the inherent tradeoff between these parameters. In particular, we focus on ADCs operating with relatively high resolution, where energy consumption constitutes a major challenge. The following analysis sheds light on the potential of joint acquisition and energy harvesting. For example, it quantifies the minimal recovery NMSE which allows a fixed n-bit ADC to operate at zero power, i.e., $E_{\text{ratio}} = 0$ dB. Alternatively, it identifies the quantization resolution n for which the *e*Sampling ADC can sample a bandlimited signal at Nyquist condition and operate at zero power, as well as the maximal amount of energy which can be harvested for an allowed level of reconstruction accuracy for both bandlimited and non-bandlimited signals.

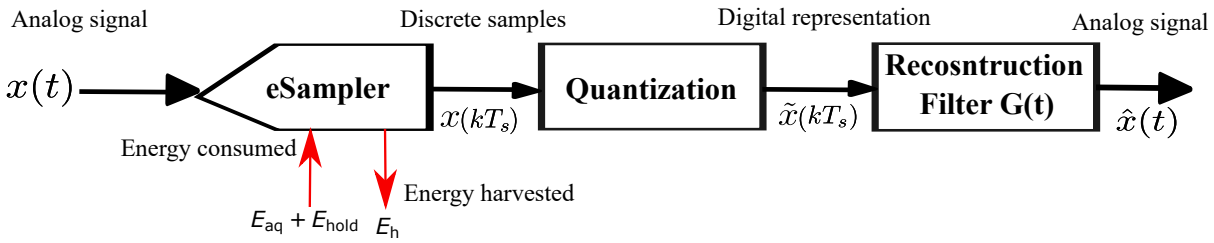

Figure 6.3: Acquisition and reconstruction via *e*Sampling ADC illustration.

6.3.2 Reconstruction NMSE

In general, the NMSE depends on both the sampling rate as well as the quantization resolution [126]. Since we focus on relatively high rate quantization, the NMSE due to quantization is well-approximated by the 6 dB rule-of-thumb [127, Ch. 23], and is thus on the order of $10^{-0.6n}$ [114], resulting in a negligible contribution to the overall NMSE of less than roughly 10^{-5} for $n \geq 8$. Therefore, henceforth the focus is on the the NMSE between $x(t)$ and $\hat{x}(t)$ due to the sampling procedure alone, expressed in the following theorem, derived in [125]:

Theorem 1 *The minimal achievable NMSE in reconstructing a uniformly sampled WSS signal $x(t)$ with sampling frequency $f_s = 1/T_\mathrm{s}$ using a linear reconstruction filter, $G(t)$ is*

$$\zeta(T_\mathrm{s}) = 1 - \frac{1}{\sigma_x^2} \sum_{k \in \mathcal{Z}} \int_{-\frac{f_s}{2}}^{\frac{f_s}{2}} \frac{|S_x(f - k f_s)|^2}{\sum_{k' \in \mathcal{Z}} S_x(f - k' f_s)} df. \tag{6.9}$$

To achieve (6.9), the linear recovery filter $G(t)$ in (6.6) is set according to [100, 125], resulting in the minimal achievable NMSE between $x(t)$ and $\hat{x}(t)$. Theorem 1 generalizes the celebrated Shannon-Nyquist theorem, as stated in

the following corollary:

Corollary 1 *When $x(t)$ is bandlimited and the sampling frequency satisfies Nyquist condition, the resulting NMSE is zero.*

If $x(t)$ is bandlimited, then there exists some finite f_m such that $S_x(f) = 0$ for all $|f| > f_m$. When the sampling rate satisfies Nyquist condition, then $f_s \geq 2f_m$. Consequently, the summands in (6.9) are non-zero only at $k = k' = 0$, and hence

$$\begin{aligned}\zeta(1/f_s) &= 1 - \frac{1}{\sigma_x^2}\int_{-\frac{f_s}{2}}^{\frac{f_s}{2}} \frac{|S_x(f)|^2}{S_x(f)}df \\ &= 1 - \frac{1}{\sigma_x^2}\int_{-f_m}^{f_m} \frac{|S_x(f)|^2}{S_x(f)}df = 0,\end{aligned} \tag{6.10}$$

proving the corollary.

We next give an example of how Theorem 1 is computed:

Example 1 *As an example, consider a bandlimited signal whose spectral support is $[-f_{\rm m}, f_{\rm m}]$ for some $f_{\rm m} > 0$ with flat PSD. The obtained NMSE for such signals computed via Theorem 1 is given by*

$$\zeta(1/f_s) = \begin{cases} 1 - \frac{f_s}{2f_{\rm m}} & f_{\rm s} \leq 2f_{\rm m}, \\ 0 & \text{otherwise.} \end{cases} \tag{6.11}$$

Fig. 6.4 illustrates of the recovery NMSE result in Theorem 1, showing which spectral portions of a signal with a flat PSD as in Example 1 are pre-

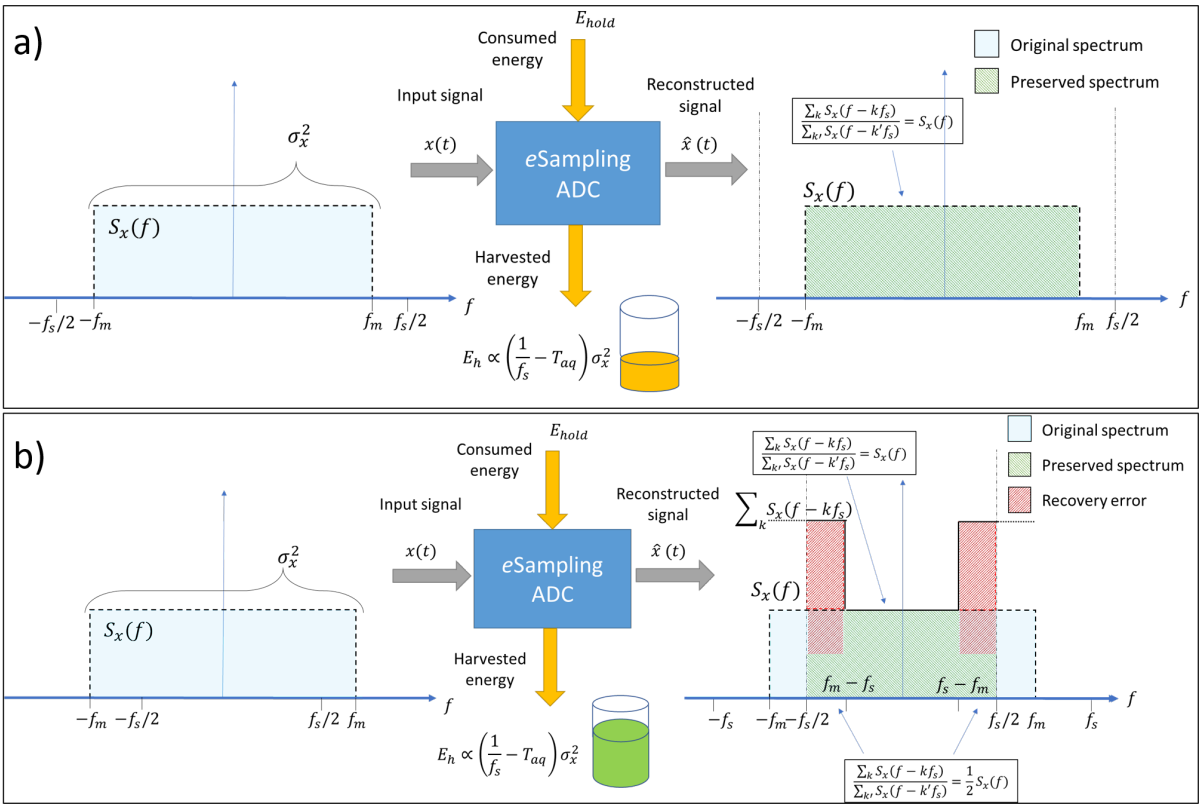

Figure 6.4: Illustration of *e*Sampling of a signal with a flat PSD for: (a) Sampling at Nyquist rate, while harvesting an amount of energy proportional to $T_{\mathrm{h}} = 1/f_s - T_{\mathrm{aq}}$; (b) Sampling at sub-Nyquist rate, thus trading recovery accuracy for harvesting more energy.

served by the NMSE minimizing reconstruction. In particular, Fig. 6.4 demonstrates how the complete spectrum is preserved when sampling above Nyquist rate, while sub-Nyquist sampling yields some recovery error due to aliased components. Fig. 6.4 also depicts the amount of energy harvested from the signal based on (6.8), showing that reduction in the sampling rate allows to harvest more energy in *e*Sampling at the cost of less accurate recovery, leading to the energy-fidelity tradeoff of *e*Sampling analyzed in the sequel.

6.3.3 Energy-Fidelity Tradeoff

In order to express the energy consumed in acquisition, we must first specify the voltage of the power supply V_{ref}. This value should be larger than the amplitude of the input signal with high probability to avoid overloading the ADC. Consequently, in the following we write the value of V_{ref} as some multiple $K > 1$ of the input standard deviation, i.e., the supply voltage is written as $V_{\text{ref}} = K\sigma_x$. This general formulation allows us to relate the reference voltage with the overload probability of the quantizer, since the overload probability satisfies $P(|x(t)| \geq V_{\text{ref}}) \leq K^{-2}$ by Chebyshev's inequality [101]. Therefore, the ratio between the expected energy harvested (6.8) and consumed (6.5) for *e*Sampling of a WSS signal can be written as

$$E_{\text{ratio}} = \frac{\frac{\eta}{R_{\text{h}}}(T_{\text{s}} - T_{\text{aq}})\sigma_x^2}{a_2(n)K^2\sigma_x^2 + a_1(n)K\sigma_x}. \tag{6.12}$$

Using the expressions for the achievable NMSE (6.9) and the energy ratio (6.12), we next characterize the energy-fidelity tradeoff of *e*Sampling. Under this setting, we formulate how the recovery accuracy and the energy ratio behave as the sampling period T_{s} varies. Recalling that the acquisition time T_{aq} is determined by the ADC circuit parameters (6.1), modifying the sampling period is equivalent to tuning the hold time T_{h}. The energy-fidelity tradeoff of *e*Sampling is thus encapsulated in two complementary optimization problems: The first aims at finding the minimal achievable NMSE under a given energy

constraint $\delta > 0$, i.e.,

$$\zeta(\delta) = \min_{T_{\rm s} > T_{\rm aq}} \zeta, \qquad (6.13)$$
$$\text{subject to } E_{\rm ratio} \geq \delta.$$

Setting $\delta = 0$ dB, implies that $E_{\rm hold} = E_{\rm h}$. Therefore, solving (6.13) with $\delta = 0$ dB reveals the minimal NMSE achievable by an *e*Sampling ADC which harvests at least as much energy as it consumes, i.e., when operating at zero power. A positive value of δ (in dB) implies an energy saving ADC which harvests more energy than its consumption per sample, namely, converting the signal only adds power to the system.

An alternative formulation seeks to maximize the energy harvested under a given fidelity constraint $\epsilon > 0$, i.e.,

$$E_{\rm ratio}(\epsilon) = \max_{T_{\rm s} > T_{\rm aq}} E_{\rm ratio}, \qquad (6.14)$$
$$\text{subject to } \zeta \leq \epsilon.$$

For instance, consider a bandlimited signal *e*Sampled at Nyquist rate. In such a case, $E^{\rm opt}_{\rm ratio}(0)$ represents the maximal portion of the consumed energy which can be harvested when seeking ideal recovery.

Problems (6.13)-(6.14) allow to characterize the energy-fidelity tradeoff, stated in the following theorem:

Theorem 2 *Let* $T_{\rm h}(\delta)$ *be given by*

$$T_{\rm h}(\delta) := \frac{\delta R_{\rm h}}{\eta \sigma_x^2} \left(a_2(n) K^2 \sigma_x^2 + a_1(n) K \sigma_x \right).$$

By setting $f_s(\delta) = \frac{1}{T_{aq} + T_{\rm h}(\delta)}$*, the solution to* (6.13) *is*

$$\zeta(\delta) = 1 - \frac{1}{\sigma_x^2} \sum_{k \in \mathcal{Z}} \int_{-\frac{f_s(\delta)}{2}}^{\frac{f_s(\delta)}{2}} \frac{|S_x(f - k f_s(\delta))|^2}{\sum_{k' \in \mathcal{Z}} S_x^H(f - k' f_s(\delta))} df. \tag{6.15a}$$

Similarly, by letting $T_{\rm s}(\epsilon)$ *be the maximal sampling interval satisfying* $\zeta(T_{\rm s}(\epsilon)) = \epsilon$ *in* (6.9)*, then the solution to* (6.14) *is*

$$E_{\rm ratio}(\epsilon) = \frac{\frac{\eta}{R_{\rm h}} (T_{\rm s}(\epsilon) - T_{\rm aq}) \sigma_x^2}{a_2(n) K^2 \sigma_x^2 + a_1(n) K \sigma_x}. \tag{6.15b}$$

The theorem follows by noting that $\zeta(T_{\rm s})$ in (6.9) is monotonically decreasing in $T_{\rm s}$, while $E_{\rm ratio}$ in (6.12) is a monotonically increasing function of $T_{\rm s}$. Consequently, both (6.13) and (6.14) are obtained by identifying the minimal/-maximal value of $T_{\rm s}$ for which the constraint holds with equality, hence proving the theorem.

In the following subsection we discuss some of the properties and insights which arise from the above energy-fidelity tradeoff analysis.

6.3.4 Discussion

The characterization of the energy-fidelity tradeoff in Theorem 2 identifies the achievable energy ratio for a given recovery accuracy and vice versa.

It also reveals the achievable energy ratio when *e*Sampling a bandlimited signal of maximum frequency $f_m \geq 0$ with zero reconstruction error. In particular, combining Corollary 1 and Theorem 2 indicates that this energy ratio is given by

$$E_{\text{ratio}}(0) = \frac{\frac{\eta}{R_{\text{h}}}\left(\frac{1}{2f_{\text{m}}} - T_{\text{aq}}\right)\sigma_x^2}{a_2(n)K^2\sigma_x^2 + a_1(n)K\sigma_x}. \tag{6.16}$$

An example of how Theorem 2 is computed for arbitrary sampling rates is given in the following:

Example 2 *Consider again the bandlimited signal with flat PSD of Example 1. In this case, by (6.11), an NMSE of $\zeta(1/f_{\text{s}}) \leq \epsilon$ is guaranteed by using $f_{\text{s}} \geq 2f_{\text{m}}(1-\epsilon)$. Consequently, by Theorem 2 the energy ratio under fidelty constraint ϵ for such signals is given by*

$$E_{\text{ratio}}(\epsilon) = \frac{\frac{\eta}{R_{\text{h}}}\left(\frac{1}{2f_{\text{m}}(1-\epsilon)} - T_{\text{aq}}\right)\sigma_x^2}{a_2(n)K^2\sigma_x^2 + a_1(n)K\sigma_x}. \tag{6.17}$$

As expected, the achievable energy ratio in Example 2 coincides with (6.16) when perfect recovery is required, i.e., $\epsilon = 0$. The energy ratio characterized in (6.17) is increased by reducing the sampling rate, which in turn increases the reconstruction error, ϵ, as illustrated in Fig. 6.4.

The fundamental balance between these measures follows from the structure of *e*Sampling ADCs, in which increasing the hold time degrades the ability to recover the signal from its samples, while allowing to harvest more energy. This unique property of *e*Sampling can lead to ADCs which harvest more power than

they consume, as we numerically demonstrate in Section 6.5 when using typical parameters of S/H ADC hardware, as well as when evaluating an experimental setup involving a dedicated design of an *e*Sampling ADC circuit.

The amount of energy harvested in *e*Sampling is determined by the sampling rate and the signal energy, as illustrated in Fig. 6.4. Consequently, unlike the recovery NMSE which depends not only on the sampling rate but also on the shape of the PSD $S_x(f)$ (6.9), the energy ratio for a fixed sampling rate is affected only by the overall input energy $\sigma_x^2 = \int S_x(f)df$ (6.12). This follows from the fundamental difference between the two objectives of *e*Sampling, i.e., acquisition and energy harvesting: The purpose of acquisition is to allow the complete signal, whose profile depends on the shape of its PSD, to be recovered from its digital representation. However, energy harvesting aims at extracting energy from the signal without having to maintain sufficiency or to avoid distorting the signal, and is invariant of specific values of its PSD.

Our characterization in the previous subsections focuses on the general family of stationary signals. When the signal obeys some structure, e.g., it is known to reside in a shift-invariant space, ideal recovery can be achieved at low sampling rates using generalized sampling methods [7], allowing to harvest more energy without affecting the recovery NMSE. This indicates that the energy-fidelity tradeoff of *e*Sampling ADCs can be further improved by accounting for structured signals, as commonly encountered in communication [98] and radar [99] systems. We leave the analysis of *e*Sampling of structured signals for future work.

The fact that *e*Sampling gives rise to ADCs which operate with zero power and can even harvest more energy than they consume, makes it an attractive technology for low-power systems, such as IoT devices, sensor networks, as well as wearable and implantable medical units. However, the fact that the proposed *e*Sampling architecture is based on S/H ADCs limits its applicability in some scenarios. For example, S/H ADCs typically operate at sampling rates below 1 GHz, and are not suitable for operating at extremely high sampling rates, where flash ADCs are more commonly used. While we conjecture that the concept of *e*Sampling, namely, the integration of energy harvesting into signal acquisition, can also be combined with alternative ADC technologies other than S/H ADCs, we leave this study for future work.

While our analysis focuses on WSS signals for analytical tractability, the proposed *e*Sampling ADCs applies to a much broader family of acquired analog signals. For example the *e*Sampling ADC circuitry detailed in the following section is experimented in Subsection 6.5.2 when acquiring a sinusoidal signal, demonstrating its ability to accurately reconstruct the signal in a power saving manner. Our proposed analysis is based on linear recovery, being a common reconstruction framework in sampling theory. In particular, the reconstruction of Nyquist rate sampled bandlimited signals, shift-invariant signals, and various other structures studied in the literature, is based on linear filtering [7]. However, the architecture of the *e*Sampling ADC is invariant to the reconstruction mechanism, and alternative recovery schemes would result in a different characterization of the energy-fidelity tradeoff.

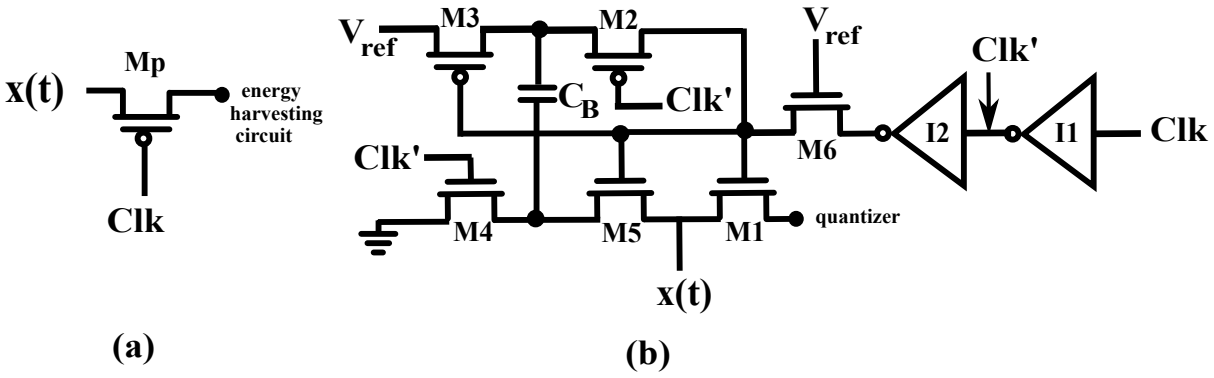

Figure 6.5: Circuit diagram of (a) PMOS transistor switch, (b) NMOS bootstrapped switch.

6.4 *e*Sampling ADC Circuit-level Design

In order to demonstrate the hardware feasibility of the concept of *e*Sampling, in this section we design and develop a prototype for such a device. In particular, we realize the *e*Sampling ADC model shown in Fig. 6.2 using standard 65 nm CMOS technology. In order to design the *e*Sampling ADC based on the high-level architecture illustrated in Fig. 6.2, one has to design its three main sub-blocks: The two-way switch $\tilde{S}$; the quantizer logic; and the energy harvesting circuit. In the following we elaborate on each of these sub-blocks.

6.4.1 Two-way switch

The two-way switch $\tilde{S}$ allows the input signal to be connected to the hold capacitor during acquisition phase and to the energy harvesting circuit during the hold phase. In our design, $\tilde{S}$ is implemented[1] using two one-way switches, one for each operation phase, namely, when one switch is open, the other is closed. Each of these switches is realized using a different topology. The

[1]The term '*implement*' used here implies the design/simulation of the circuit in Cadence Virtuoso platform, in line with the similar usage of this terminology in [110–113, 116].

switch designed to connect the input signal to the energy harvesting circuit is implemented using a PMOS transistor, as illustrated in Fig. 6.5(a). The PMOS transistor turns ON when the clock signal Clk is at logic '0', indicating that hold phase is active. When Clk is at logic '1', it turns OFF and isolates the input signal from the next block. In order to allow both switches of $\tilde{S}$ to utilize the same single clock pulse, the switch designed to connect the input signal with the quantizer is implemented using an NMOS transistor, which turns on when Clk is at '1'.

The on-resistance of a MOS transistor, which determines the value of R_{on} in (6.1), is sensitive to fluctuations in the input signal and may vary accordingly [114]. Such variations in R_{on} may introduce a non-linear distortion at the output of the ADC. To avoid such distortion, we use an NMOS bootstrap switch to connect the input signal to the quantizer, which ensures a constant R_{on}, as proposed in [128]. The design of the NMOS transistor based bootstrapped switch used in this work is illustrated in Fig. 6.5(b). To achieve nearly constant R_{on}, the gate of the transistor $M1$ in Fig. 6.5(b) is bootstrapped using two PMOS transistors $M2$ and $M3$, three NMOS transistors $M4$, $M5$ and $M6$, and one capacitor C_{B}, as shown in [128]. Two CMOS inverters $I1$ and $I2$ are also employed in the structure to generate the required clock signals needed for proper operation of the switch.

The value of the on-resistance R_{on} as well as the hold capacitor C_{h} affect the setting of the acquisition time T_{aq}, which follows from (6.1). To maximize the amount of energy harvested, small values of T_{aq} are preferable, so that more

time could be allocated to harvesting the input signal energy. Reducing R_{on} requires increasing the width of the transistors [114], which in turn increases the device capacitance, and thus reduces the operating speed of the ADC. In addition, wider devices may result in charge injection [129], which degrades the signal-to-noise-distortion ratio (SNDR) of the ADC, and hence the performance of the ADC. Alternatively, employing small values for C_{h} results in mismatch issues and sampling noise, which degrade the ADC conversion accuracy [130, 131]. These drawbacks require the acquisition time T_{aq} to be large enough such that the ADC performance is not compromised, and is in fact the primary reason S/H ADCs are typically limited to operate with sampling rates below 1 GHz, as discussed in Subsection 6.3.4.

6.4.2 Quantizer

The dedicated *e*Sampling ADC circuit design is based on S/H SAR ADC architectures [115, 119, 132] as illustrated in Figs. 6.1-6.2. Such quantizers generally consist of a DAC, a voltage comparator and a SAR logic, which map the voltage of the hold capacitor (also known as the total capacitance of DAC array) into an n-bit value by successively refining the digital representation using a binary search algorithm. In our *e*Sampling ADC circuit we use a single-ended merge capacitor switching (MCS) based SAR ADC. For such devices, the total capacitance of the DAC array is $C_{\text{h}} = 2^{n-1}C_{\text{u}}$, where C_{u} is the unit capacitance of the DAC array, as illustrated in Fig. 6.6.

In particular, during acquisition phase the input signal $x(t)$ is connected to

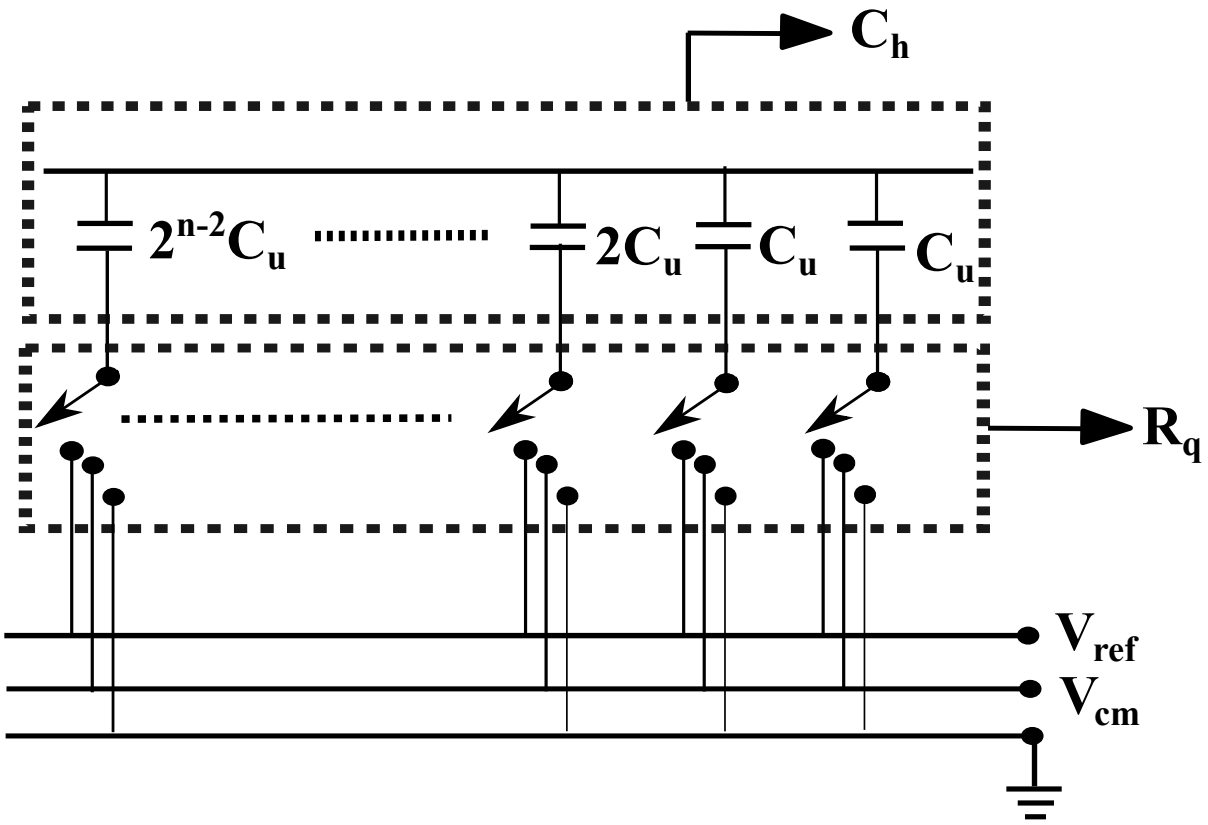

Figure 6.6: DAC capacitor array schematic diagram.

the top plate of the DAC capacitor array, while the bottom plate is connected to the common mode voltage, i.e., $V_{\rm cm} = \frac{V_{\rm ref}}{2}$. Once the acquisition phase is over, the voltage at the top plate of the DAC capacitor array is reduced by common mode voltage, and hence equals to $x(kT_s) - V_{\rm ref}/2$. The top plate of the DAC capacitor array is connected to the positive terminal of the comparator, while the negative terminal of the comparator is grounded, as illustrated in Fig. 6.1(b). The comparator then compares the voltage of its positive terminal with its negative terminal. If the voltage at the positive terminal is higher than the negative terminal, the comparator yields an output to be logic '1', else logic '0'. The output of the comparator is passed to the SAR logic, which resolves the most significant bit (MSB). The decision on the MSB is fed back to the DAC and the

bottom plate of the largest capacitor of DAC capacitor array is switched from $V_{\rm cm}$ to ground (if MSB=1) or $V_{\rm ref}$ (if MSB=0). The overall resistance of the switches is the binary scale switch resistance, $R_{\rm q}$ illustrated in Fig. 6.6. This operation changes the voltage at the top plate of the DAC capacitor array, and a new decision is made by the comparator, which is sent to the SAR logic to resolve the second MSB and so on. The process continues for all n bits.

As discussed in Subsection 6.2.1, the energy consumption of S/H SAR ADCs is effectively determined by its quantization sub-blocks. Therefore in the following, we present the detailed circuitry used for the quantizer along with its energy usage per sample.

The voltage comparator is implemented using a dynamic latch. The energy consumed per sample of a dynamic latch comparator is given by [119]

$$E_{\rm c} = nC_{\rm c}V_{\rm ref}^2 + 2V_{\rm ref}\gamma_{\rm n}, \tag{6.18}$$

where $\gamma_{\rm n} := V_e C_{\rm c}\big(n \ln 1/A_{\rm k} + \frac{n(n+1)}{2}\ln 2 + n\big)$, $C_{\rm c}$ is the capacitive load of the comparator, $A_{\rm k}$ is the gain during regenerative phase, and $V_{\rm e}$ is the ratio of the drain current of the device with its trans-conductance [133]. The SAR logic is realized using two arrays of shift registers that operate in serial-in-parallel-out and parallel-in-parallel-out modes [134]. Each register is implemented using a D flip-flop circuit, and the resulting energy consumption is given by [119]

$$E_{\rm sl} = 16n^2 g C_{\rm s} V_{\rm ref}^2, \tag{6.19}$$

where C_{s} is the input capacitance of the D flip-flop, and $g \in [0,1]$ is the total activity parameter of the SAR logic. Finally, the DAC is based on a binary-weighted capacitive DAC, designed using the MCS scheme [115]. The energy consumption of the MCS DAC is given by [115]

$$E_{\mathrm{DAC}} = \rho_{\mathrm{n}} n C_{\mathrm{u}} V_{\mathrm{ref}}^2, \tag{6.20}$$

where $\rho_{\mathrm{n}} = \sum_{i=1}^{n-1} 2^{n-3-2i}(2^i - 1)$.

To summarize, the total energy consumption during hold phase of our dedicated *e*Sampling ADC circuit design, which dictates the overall energy consumed per sample, is given by

$$\begin{aligned} E_{\mathrm{hold}} &= E_{\mathrm{DAC}} + E_{\mathrm{sl}} + E_{\mathrm{c}} \\ &\overset{(a)}{=} V_{\mathrm{ref}}^2 \left(\rho_{\mathrm{n}} C_{\mathrm{u}} + n C_{\mathrm{c}} + 16 n^2 C_{\mathrm{s}} g\right) + 2 V_{\mathrm{ref}} \gamma_{\mathrm{n}}, \end{aligned} \tag{6.21}$$

where (a) follows from (6.18), (6.19), and (6.20). The energy term in (6.21) obeys the second-order polynomial model of (6.4), used in our analysis of *e*Sampling ADCs in Section 6.3.

6.4.3 Energy Harvesting Circuit

The proposed *e*Sampling ADC harvests the input signal energy during hold phase and stores this energy in a capacitor, C_{EH}. As detailed in Subsection 6.2.2, energy harvesting circuits typically consist of a capacitor, in which the harvested energy is stored, and a signal conditioning circuit, whose purpose is

to facilitate the charging of the capacitor. In our design, we do not include a signal conditioning circuit and forward the input signal directly to C_{EH} during hold time. This simplified design is sufficient for our experimental purposes, where we use synthetic controlled input signals with strictly positive voltage values. However, in order to achieve efficient energy harvesting from a low voltage complex rapidly alternating signals, one should also include signal conditioning devices [121–123], such as a rectifier, voltage regulator and DC-DC converter.

To quantify the maximum amount of energy that can be harvested in an analytically tractable manner, we consider the case where the input signal is approximately constant during the hold phase, i.e., $x(t) \approx x(T_s)$ for each $t \in [T_{\mathrm{aq}}, T_{\mathrm{s}}]$. In addition, we focus on the scenario in which the capacitor is empty at the beginning at the hold phase, basically, the voltage on the capacitor C_{EH}, denoted $V_{\mathrm{EH}}(0)$, satisfies $V_{\mathrm{EH}}(T_{\mathrm{aq}}) = 0$. In this setup, the capacitor voltage at the end of the hold phase, i.e., at time instance $t = T_{\mathrm{s}}$, is given by

$$V_{\mathrm{EH}}(T_{\mathrm{s}}) \approx x(T_s)\left(1 - e^{-\frac{T_{\mathrm{h}}}{R_{\mathrm{h}}C_{\mathrm{EH}}}}\right), \tag{6.22}$$

where, as defined in Subsection 6.3.1, R_{h} is the resistance of the energy harvesting circuit. This resistance is dictated here by the on-resistance of the PMOS transistor in a two-way switch. The amount of energy harvested in such a sam-

pling interval is given by

$$\begin{aligned} E_{\mathrm{h}} &= \frac{1}{2} C_{\mathrm{EH}} V_{\mathrm{EH}}^2(T_{\mathrm{s}}) \\ &\overset{(a)}{\approx} \frac{1}{2} C_{\mathrm{EH}} \left(1 - e^{-\frac{T_{\mathrm{h}}}{R_{\mathrm{h}} C_{\mathrm{EH}}}}\right)^2 x^2(T_s) \\ &\overset{(b)}{\approx} \frac{1}{2T_{\mathrm{h}}} C_{\mathrm{EH}} \left(1 - e^{-\frac{T_{\mathrm{h}}}{R_{\mathrm{h}} C_{\mathrm{EH}}}}\right)^2 \int_{T_{\mathrm{aq}}}^{T_{\mathrm{h}}} |x(t)|^2 dt, \end{aligned} \tag{6.23}$$

where (a) follows from (6.22), and (b) stems from the fact that the input is approximately constant during the hold phase. Comparing (6.23) and (6.8) reveals that the efficiency of this simple energy harvesting circuit can be approximated as

$$\eta \approx \frac{R_{\mathrm{h}} C_{\mathrm{EH}}}{2T_{\mathrm{h}}} \left(1 - e^{-\frac{T_{\mathrm{h}}}{R_{\mathrm{h}} C_{\mathrm{EH}}}}\right)^2. \tag{6.24}$$

The expression for the energy harvesting efficiency in (6.24) can be used to provide guidelines for determining the capacitance C_{EH} used in the circuit. In particular, it can be shown that (6.24) is maximized when $C_{\mathrm{EH}} \approx 0.796 \frac{T_{\mathrm{h}}}{R_{\mathrm{h}}}$. However, the derivation of (6.24) is carried out assuming that the capacitor is empty at the beginning of the hold phase. This implies that its stored energy is transferred to some external storage device, e.g., battery, after each sample. In practice, energy transfer typically takes much longer than a single sampling interval, and thus it is preferable to carry out such a transfer only once every multiple samples. This is achieved by using a capacitor with a larger value of C_{EH}, which allows to store more energy and provides a nearly constant voltage at the load, but requires more time to charge. In particular, in our experimental

setup detailed in Subsection 6.5.2, we set $C_{\mathrm{EH}} = 42.2\frac{T_{\mathrm{h}}}{R_{\mathrm{h}}}$, which results in the capacitor taking approximately 340 samples to charge up. Under such a setting, the period dedicated to transferring its energy once it is fully charged, during which energy harvesting is inactive, has only a minor impact on the overall harvested energy.

6.5 Experimental study

In this section we evaluate the proposed *e*Sampling ADC in an experimental study. We first numerically evaluate the the energy-fidelity tradeoff characterized in Section 6.3, after which we present experimental results obtained with the *e*Sampling ADC circuit simulated on Cadence Virtuoso platform detailed in Section 6.4.

6.5.1 Numerical Simulations

We begin by numerically evaluating the energy-fidelity tradeoff of *e*Sampling ADCs, characterized in Theorem 2, for various ADC configurations. We consider three models for the analog input signals with the following PSDs:

- *Flat PSD*: A bandlimited signal with $S_x(f) = \frac{\sigma_x^2}{2f_{\mathrm{m}}}$ for $f \in [-f_{\mathrm{m}}, f_{\mathrm{m}}]$, $f_{\mathrm{m}} > 0$, and $S_x(f) = 0$ otherwise.
- *Unimodal PSD*: $S_x(f) = \alpha e^{-\frac{f^2}{2\sigma^2}}$, where $\alpha = \frac{\sigma_x^2}{\sqrt{2\pi\sigma^2}}$ such that $\int_{-\infty}^{\infty} S_x(f)df = \sigma_x^2$. The parameter σ^2 controls the PSD width, and the signal is approxi-

mately bandlimited with frequency $f_m = 3\sigma$.

- *Multimodal PSD*: $S_x(f) = \frac{\alpha}{2}(e^{-\frac{(f-f_t)^2}{2\sigma^2}} + e^{-\frac{(f+f_t)^2}{2\sigma^2}})$, where $f_\mathrm{t} = f_m$ MHz. The resulting signal is approximately bandlimited $f_m = 6\sigma$.

We set $K^2 = 20$, guaranteeing a probability of over 95% that $|x(t)| \leq V_\mathrm{ref}$, and hence the ADC accuracy is not compromised by quantizer overloading. The design parameters can be selected from the range provided in [119, 133, 135]. However, to be consistent with our circuit level design, we have considered the design parameters obtained through our own design simulated on Cadence virtuso platform, i.e., $f_m = 19.8$ MHz, $T_\mathrm{aq} = 2.5$ ns, $C_\mathrm{u} = 10$ fF, $C_\mathrm{c} = 5$ fF, $C_\mathrm{s} = 0.7$ fF, $R_\mathrm{h} = 23.75\ \Omega$, $A_\mathrm{k} = 1.8$, $V_\mathrm{e} = 0.05$ V, $\alpha_\tau = 5$, $V_\mathrm{ref} = 0.8$ V and $g = 0.4$. We set the efficiency of the energy harvesting system η to be 0.7, which is in line with similar values reported for energy harvesting circuits in [136–138]. Finally, the signal power σ_x^2 is accordingly set to $\frac{V_\mathrm{ref}^2}{K^2}$.

Figs. 6.7, 6.8 and 6.9 depict the resulting energy-fidelity tradeoff, i.e., the NMSE against the energy ratio E_ratio (in dB) for an input with a flat PSD, unimodal PSD and a multimodal one, respectively. In these figures, different tradeoff values for each configuration are achieved by varying the sampling rate. All simulated *e*Samplers utilize relatively high resolution quantization, i.e., $n \geq 8$, resulting in negligible distortion due to quantization, and thus the main source of error stems from the sampling operation, as treated in our analysis in Section 6.3. It is emphasized that for a given sampling rate, *e*Sampling ADCs implement the same acquisition mapping as conventional S/H ADCs, and thus

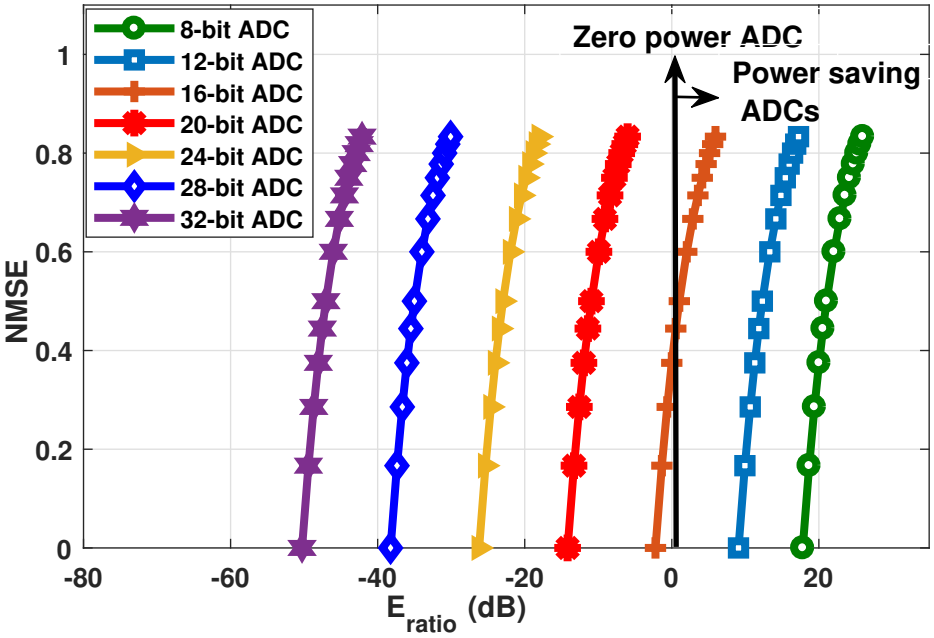

Figure 6.7: NMSE (ζ) versus E_{ratio}, flat PSD.

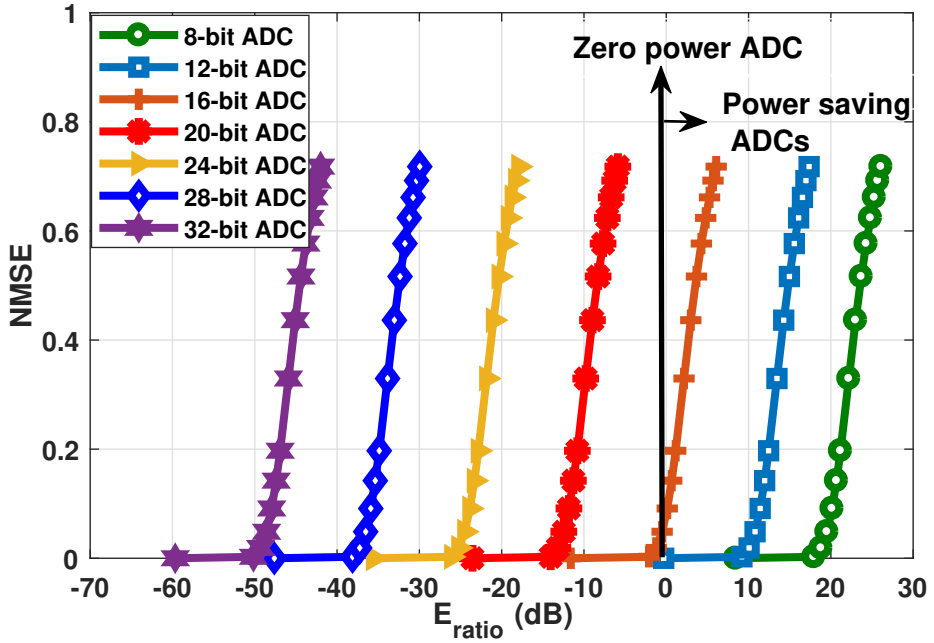

Figure 6.8: NMSE (ζ) versus E_{ratio}, unimodal PSD.

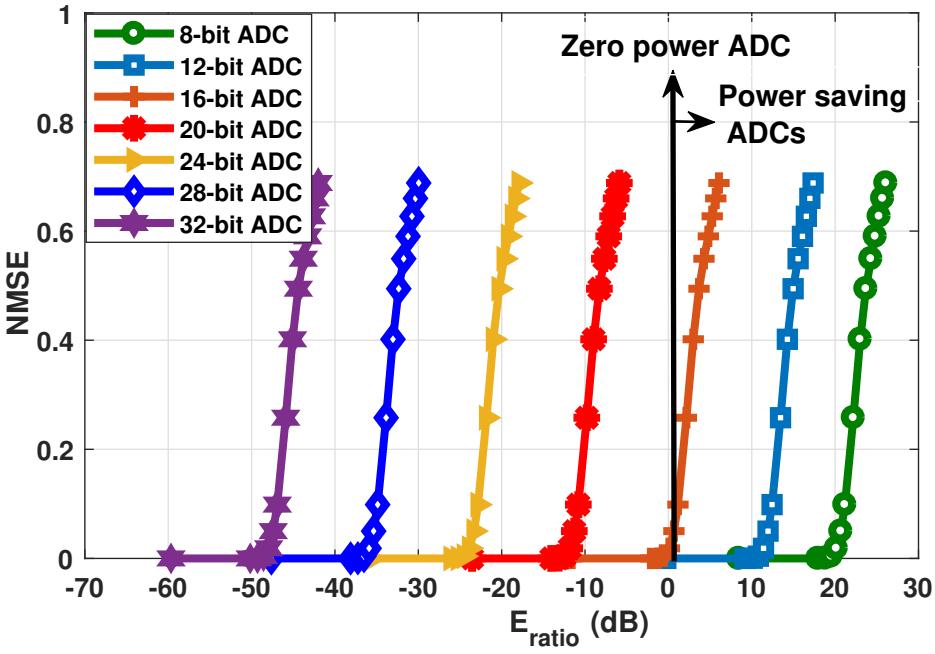

Figure 6.9: NMSE (ζ) versus E_{ratio}, multimodal PSD.

their the ability to harvest energy using *e*Sampling ADCs does not come at the expense of conversion accuracy. However, *e*Sampling provides the possibility to increase the amount of energy harvested by increasing the sampling interval, which in turn may degrade the ability to recover the analog signal.

The results shown in Fig. 6.7 demonstrate that an *e*Sampling ADC with up 12 bits, which acquires an analog signal with a flat PSD, can harvest more power than it consumes while sampling at Nyquist condition, and hence achieving zero-approaching reconstruction error. However, for the ADC to operate at zero power with higher resolution quantization, one has to sample below the Nyquist rate and hence compromise with reconstruction error. The corresponding energy-fidelity curves for the non-purely-bandlimited signals are illustrated in Figs. 6.8 and 6.9. These results demonstrate that *e*Sampling ADCs can operate with zero power for up to $n = 16$ bits of quantization resolution, while

achieving approximately ideal reconstruction by using sampling rate not smaller than f_{m}, which here is only an approximate maximal frequency.

As noted in Section 6.3, both the amount of energy harvested from a stationary signal as well as that consumed in *e*Sampling do not depend on the spectral profile of the signal, but on the sampling rate and the signal variance σ_x^2. Here, the amount of energy harvested (6.8) when *e*Sampling at $f_{\mathrm{s}} = 2f_{\mathrm{m}}$ is numerically evaluated as 0.35 pJ, while the corresponding amount of energy consumed (6.21) when using $n = 8$ bit quantizers is 21.2 pJ.

This implies that the *e*Sampling ADC is able to harvest much more energy from the signal than it consumes in converting it into a digital representation, as the energy ratio indicates an energy gain of 17.8 dB. In particular, it is observed that *e*Sampling ADCs operating with less than 12 bits are capable of saving power. However, this mode of operation comes at the cost of increased NMSE for higher values of n. The numerical results presented in this subsection indicate that the power consumption of high resolution ADCs can be notably reduced and even mitigated by properly combining acquisition and energy harvesting via *e*Sampling. In the next subsection we demonstrate that these results do not follow only from a numerical evaluation of our theoretical results, but also reflect the performance in terms of recovery accuracy and energy efficiency of an dedicated *e*Sampling ADC circuit design.

6.5.2 Circuit-level Experiment

To validate that the energy saving potential of *e*Sampling ADC observed in the previous subsection also reflects in a real world environment, we next evaluate the *e*Sampler circuit design. To that aim, a schematic of *e*Sampling SAR ADC has been created in Cadence Virtuoso platform based on the circuit-level design detailed in Section 6.4. The proposed *e*Sampling ADC operates at a sampling frequency of 40 MHz with an $n = 8$ bit quantizer. For our experimental purpose, we use a sinusoidal signal, being a common benchmark for evaluating the accuracy of ADC circuits [139, Ch. 2]. The maximum frequency of the input signal is 19.8 MHz, thus the sampling rate satisfies the Nyquist condition. The amplitude of the signal varies from 0 to V_{ref}. Here, we use an energy harvesting capacitor of $C_{\text{EH}} = 40$ nF, while the remaining design parameters are the same those utilized in our numerical evaluation in the previous subsection.

We first assert that the *e*Sampling ADC is indeed capable of accurately reconstructing the signal sampled at the Nyquist rate. To that aim, we depict the fast Fourier transform (FFT) of the reconstructed signal, computed using a 1024-point FFT, in Fig. 6.10. As expected, the FFT noise floor is determined by the SNDR due to quantization, computed by the 6 dB rule of thumb as approximately 48 dB, with the additional FFT processing gain of $10 \log_{10}(1024/2) \approx 27$ dB [139, Ch. 2]. In particular, the gap between the noise floor observed in Fig. 6.10 and the energy of the signal at its central frequency of 19.8 MHz, is roughly 75.52 dB, settling with the theoretical performance of ADCs satisfying

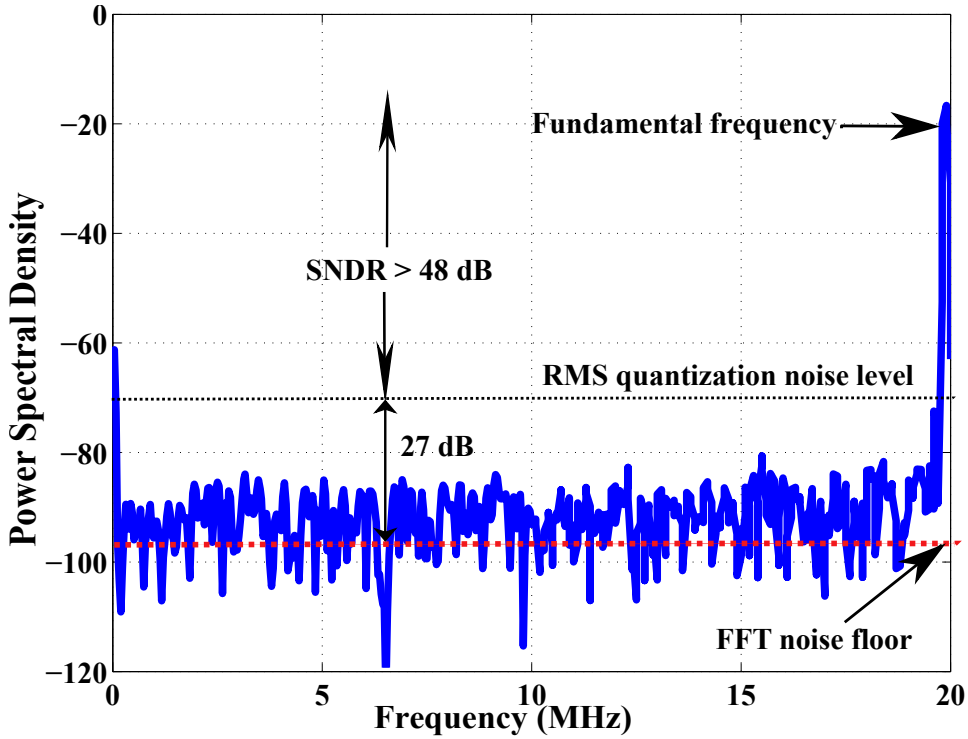

Figure 6.10: FFT plot of reconstructed signal for 8 bit *e*Sampling ADC.

Nyquist condition, and indicating that the designed *e*Sampling ADC accurately reconstructs the observed analog signal.

Next, we focus on the energy harvesting circuit of the designed *e*Sampler, in order to identify how many sampling rounds are required for the capacitor to charge up. To that aim, we plot in Fig. 6.11 the voltage on the energy harvesting capacitor over time. Observing Fig. 6.11, we note that for the given input signal, the capacitor reaches a steady level of $V_{\text{EH}} = 481.152$ mV after 8.432 μs, which correspond to 337 samples at 40 MHz. Based on Fig. 6.11, we design the *e*Sampling ADC to transfer the energy stored in its energy harvesting capacitor once every 337 samples. We dedicate approximately 1.5 μs for each transfer, during which the energy harvesting circuit is inactive, resulting in each cycle of harvesting and transferring taking approximately 500 samples. Consequently,

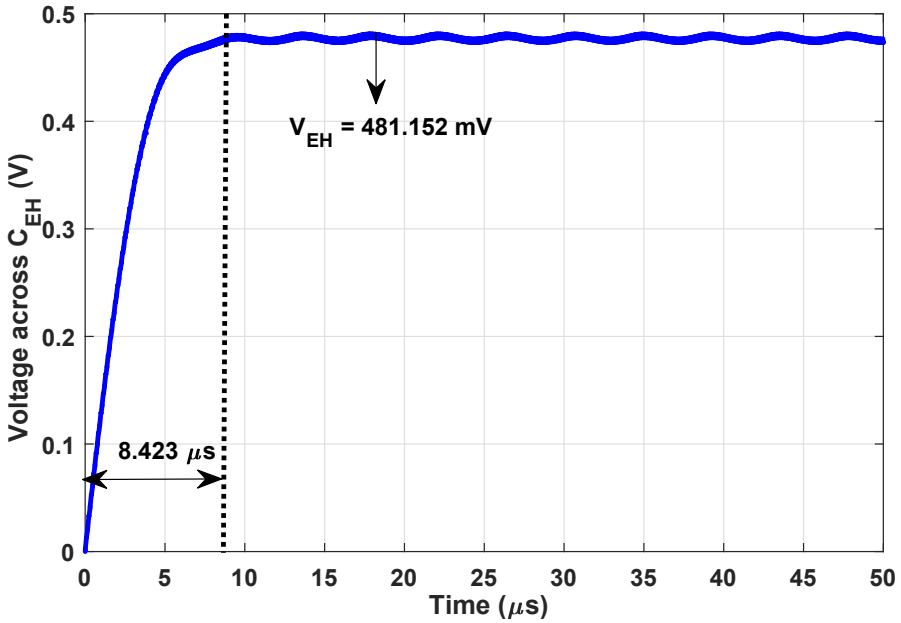

Figure 6.11: Voltage obtained across C_{EH} for 8 bit *e*Sampling ADC.

the effective amount of energy harvested per sample of the *e*Sampling ADC is given by

$$E_{\mathrm{h}} = \frac{1}{2 \cdot 500} C_{\mathrm{EH}} V_{\mathrm{EH}}^2 (337 \cdot T_{\mathrm{s}}) = 9.26pJ. \tag{6.25}$$

The amount of energy harvested per sample, evaluated in (6.25) based on the experiment in Fig. 6.11, does not represent the overall energy balance of the *e*Sampling ADC, as it accounts only for the amount of energy harvested. Therefore, to demonstrate that the *e*Sampling ADC circuit design not only accurately recovers the signal and harvests energy, but also saves more energy than it consumes, we next evaluate both the energy harvested and the energy consumed by the ADC circuit. The average energy consumption of our designed circuit is computed by evaluating the current drawn from its reference source V_{ref}, denoted $I_{\mathrm{ref}}(t)$, and thus the energy consumed at each time instance can be

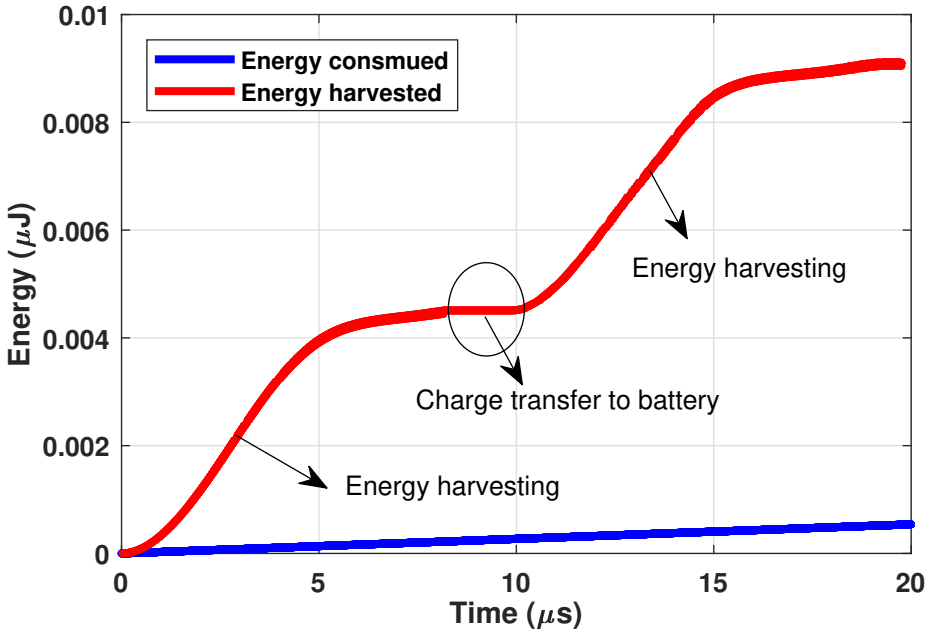

Figure 6.12: Total energy harvested and energy consumed versus time for an 8 bit *e*Sampling ADC.

obtained by

$$E_{\text{cons}}(t) = V_{\text{ref}} \int_0^t I_{\text{ref}}(\tau) d\tau. \tag{6.26}$$

The resulting growth of both the energy consumed and the energy harvested are depicted in Fig. 6.12. Observing Fig. 6.12, we note that the *e*Sampling ADC harvests much more energy than it consumes, while still being able to accurately reconstruct its input signal as demonstrated in Fig. 6.10. In particular, the consumed energy is shown to grow in an approximately linear manner, with an average energy consumption of 0.56 pJ per sample. The maximal amount of energy which can be obtained is dictated by the external battery, to which the harvested power is periodically transferred. Comparing this to (6.25) reveals that the true energy ratio of the *e*Sampling ADC, which periodically transfers its harvested energy to an external battery, is approximately 12.1 dB, which is within a relatively small gap from the theoretical results observed in Subsec-

tion 6.5.1. This gap can be further reduced by using more advanced energy harvesting circuitry, compared to the simplistic design detailed in Subsection 6.2.2. In particular, using more advanced harvesting architecture is expected to improve the efficiency η, allowing to achieve improved energy-fidelity tradeoffs compared to those observed here. Nonetheless, despite its relatively simple architecture, the *e*Sampling ADC circuit design is still able to achieve accurate reconstruction while harvesting substantially more energy than it consumes.

6.6 Real time Validation of *e*Sampling

In this section, we have discussed the hardware setup of *e*Sampling for a sensing application. The work has been demonstrated for both environment as well as health monitoring application. Section 6.6.1 discusses the circuit of the setup and Section 6.6.2 discusses the experimental results.

6.6.1 Hardware setup

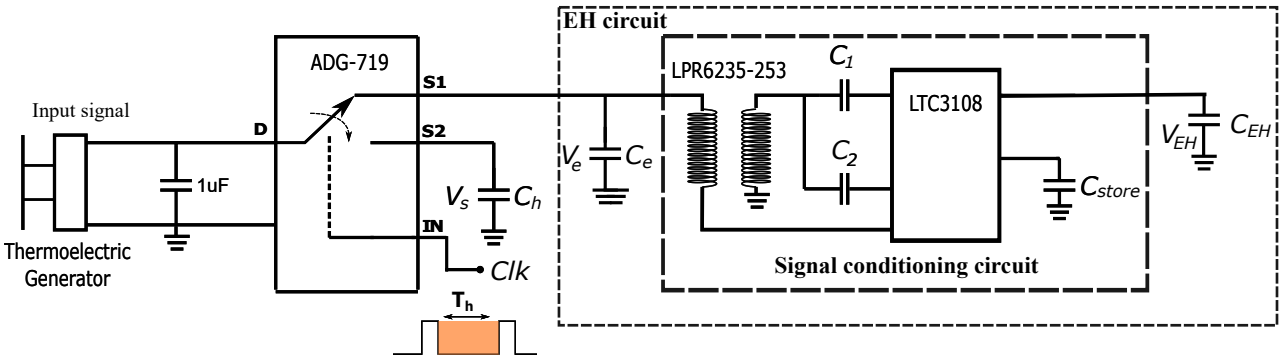

Figure 6.13: Hardware Prototype

To demonstrate the proposed *e*Sampling framework in real world environ-

ment, a hardware set up similar to Fig. 6.2 has been built. The hardware prototype has been shown in Fig. 6.13. The input analog signal is obtained via sensing of the external temperature using a sensing element i.e., thermal electric generator (TEG). TEG can produce an output voltage from 10 mV to 50 mV per °C change in temperature [140]. The switch $\tilde{S}$ have been implemented using single pole double throw (SPDT) ADG791 monolithic CMOS switch. A Clk signal based upon T_{s} and $T_{\mathrm{aq}} = 0.1T_{\mathrm{s}}$ has been generated externally and applied to ADG719 through its terminal IN as illustrated in Fig. 6.13. The switch will connect the input signal, D to one output terminal for duration of 10% of the total sampling period (T_{s}) and to another output terminal with duration of 90% of T_{s}, respectively. The output terminals obtaining 10% and 90% time of the total sampling period has been connected to C_{h} for acquiring data samples, through $S2$ and C_{EH} for storing energy through $S1$, respectively. The voltage received at the input of the energy harvesting circuit, denoted as V_{e} will be passed to an signal conditioning circuit, i.e., LPR6235-253 step-up converter and LTC3108, which will boost the voltage signal to 5V. Hence, the maximum voltage received at energy storage capacitor i.e., V_{EH} is 5V.

6.6.2 Experimental Results

The pictorial view of the hardware prototype has been shown in Fig. 6.14. The value for C_{h}, C_{EH} and V_{EH} is 1 μF, 10 μF and 5 V, respectively. Further, the value of C_1, C_2 and C_{store} is 330 pF, 1 nF and 0.1 F, respectively. The experiment has been performed on two different sets of input signals; one is generated

from the controlled environment and another from the human palm. In subsequent sub-sections, we will be discussing the different experiments performed on the designed setup.

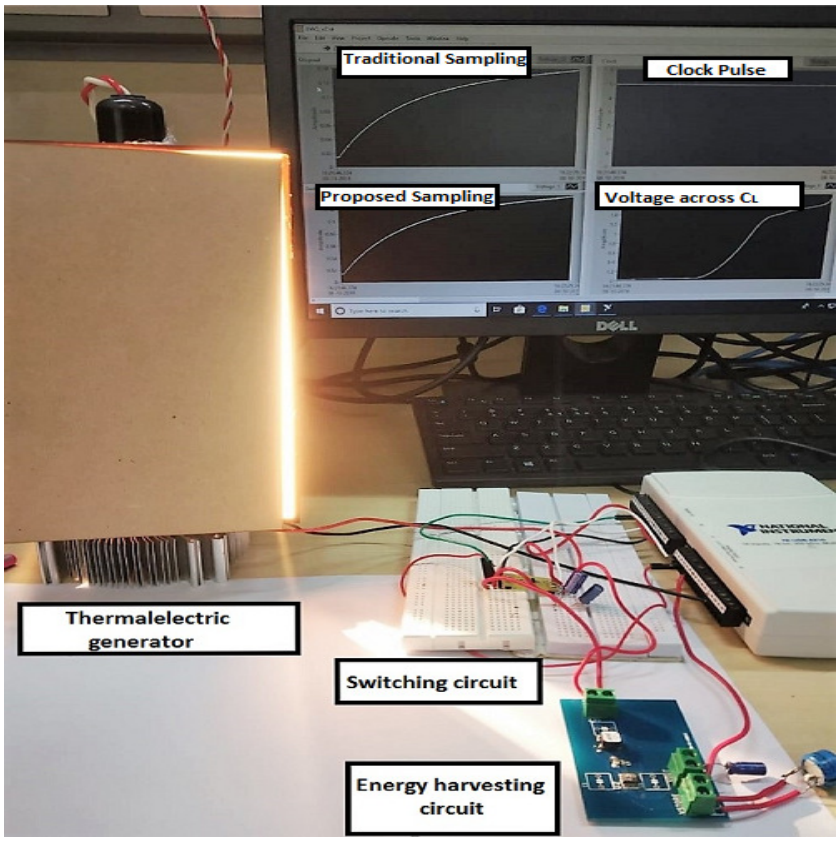

Figure 6.14: Pictorial view of Hardware Prototype

6.6.2.1 Controlled Environment

For this experiment, the input analog signal generated from TEG is in a controlled environment. The samples obtained at C_{h} has been used to reconstruct the analog signal using NI DAQ USB-6210, and Fig. 6.15 compares the reconstructed signal obtained with the traditional sampling process and the proposed *e*Sampling process for sampling frequency of 1 KHz. From the figure, it can be observed that the reconstructed signal with both process is similar, and hence

harvesting the energy along with sampling using *e*Sampling is not degrading the performance of conventional sampling process of an ADC.

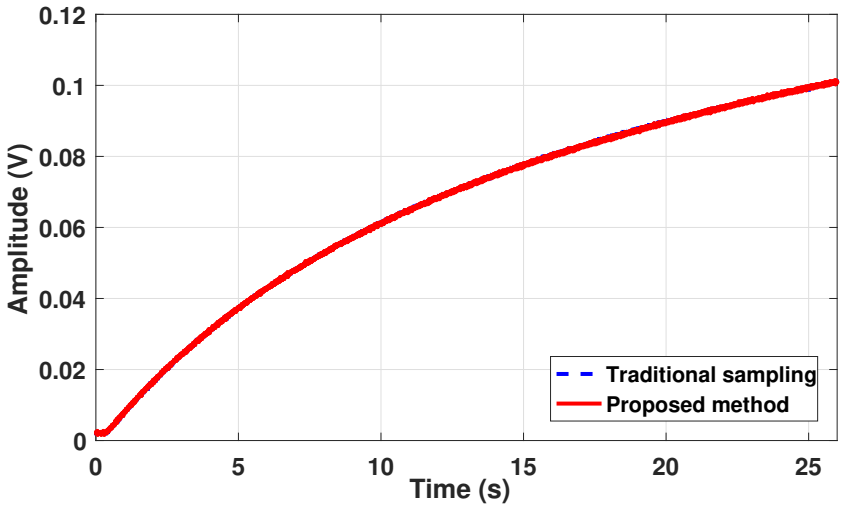

Figure 6.15: Reconstructed signal obtained with traditional sampling and the proposed *e*Sampling method for controlled environment

For the fixed value of C_{EH} and V_{EH}, the amount of energy harvested will always same (6.23). However, the amount time required by V_{EH} to reach 5V will be different, and hence the amount of energy harvested per time will vary and is dependent on various parameters such as C_{e}, C_{EH}, f_{s} and T_{aq}. For fixed f_{s} and T_{aq}, the size of the C_{e} plays an important role in harvesting maximum input signal energy. This is due to the fact that the signal at the input of the EH circuit (obtained from the output terminal **S1** of ADG719 switch) is discontinuous, as shown in fig. 6.13. The frequency of discontinuity is the same as the sampling frequency of the system. To harvest maximum power from the signal obtained at **S1** terminal, an optimum value of C_{e} must be chosen. This is obvious as the charge stored in C_{e} will be transferred to the succeeding blocks of the circuit. In other words, if C_{e} is not optimum, the maximum power can't be harvested from the input signal.

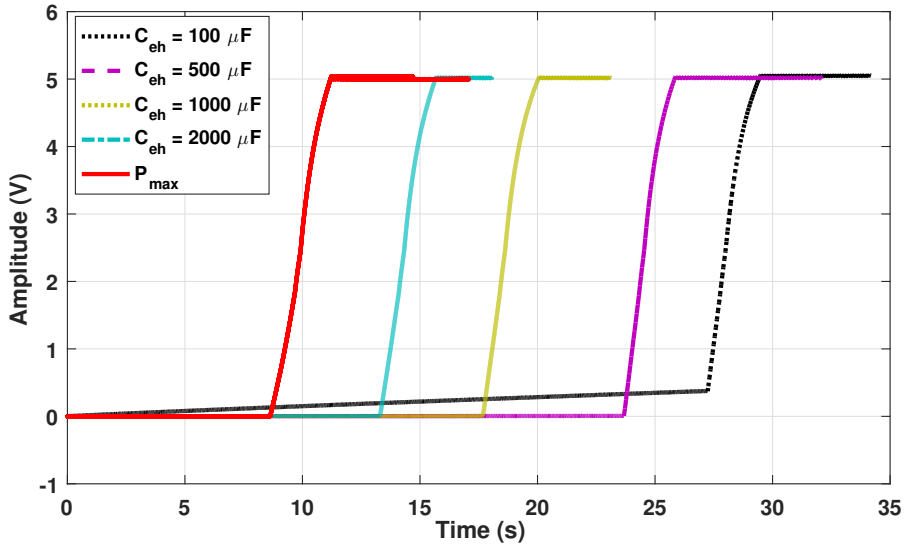

Figure 6.16: Voltage across C_{EH} obtained from controlled environment with different C_{e}.

In order to store maximum charge at low frequency, a large C_{e} should be chosen because more time is available (T_{h}) to charge C_{e}. However, at high frequency, the T_{h} is small, and hence a large C_{e} will take more time and can't charge to the peak value of the input signal. Therefore, comparatively a small value capacitor should be chosen for high sampling frequency. To validate the

Table 6.1: Performance metric with different C_{e} at $f_{\mathrm{s}} = 1$ kHz

C_{e} (μF)	$t_{\mathrm{C_{EH}}}$ (s)	$\frac{1}{2}\frac{C_{\mathrm{EH}}V_{\mathrm{EH}}^2}{t_{\mathrm{C_{EH}}}}$ (μW)	η (%)
100	29.42	4.248	38.03
500	25.829	4.8395	43.33
1000	20.035	6.2391	55.86
2000	15.66	7.9821	71.47

above argument that the amount of energy harvested per time can be increased by optimally choosing the C_{e}, the voltage obtained at C_{EH} has been plotted for different values of C_{e} in fig. 6.16. The observations have been summarized in Table 6.1. It has been observed that the amount of time required by C_{EH} to reach $V_{\mathrm{EH}} = 5$V, denoted as $t_{\mathrm{C_{EH}}}$ has been reduced significantly by increasing

C_{e}. This is because, at $f_s = 1$ kHz, more charging time is available, and hence by increasing C_{e}, more charge could be stored in the capacitor, which will be passed to the succeeding booster circuit (LPR6235-253 step-up converter and LTC3108). As soon the booster circuit will receive the required charge, it will reach to $V_{\mathrm{EH}} = 5$ V. At $C_{eh} = 2000$ μF, LTC3108 provides $V_{\mathrm{EH}} = 5$ V in 15.66 seconds, and hence the achieved η is 71.47%.

6.6.2.2 Human Palm

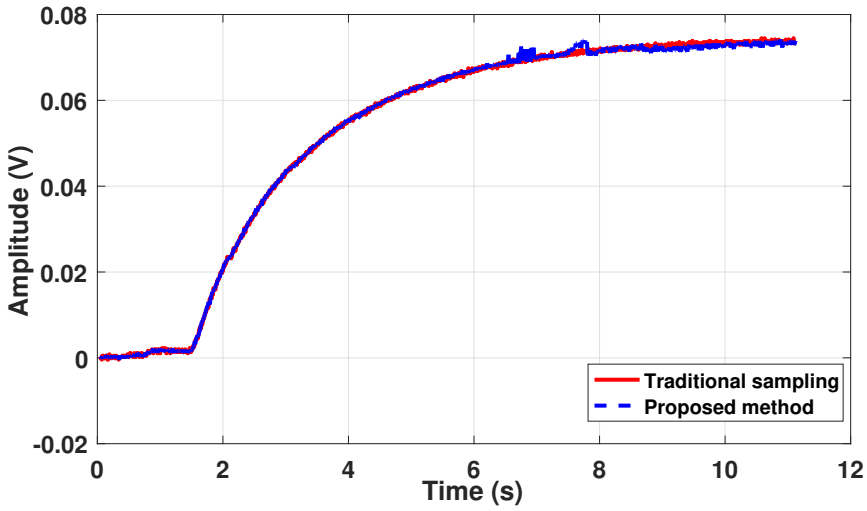

Figure 6.17: Reconstructed signal obtained with traditional sampling process and with the proposed method from human palm.

In order to harvest energy during data acquisition for human monitoring application, the eSampling has been experimented by generating the input signal from the heat produced through the human palm. Further, to be consistent with the above setup, the selected f_{s} is 1 kHz, which is enough to sample the considered data. Also, $T_{aq} = 1$ ms and $T_{\mathrm{h}} = 9$ ms. The input signal is sampled with traditional sampling process and also with the *e*Sampling method at C_{h}. The samples obtained at C_{h} has been used to reconstruct the analog signal using NI

DAQ USB-6210. The reconstructed signal using both processes has been plotted in Fig. 6.17. The signal obtained at the output of EH circuit has been shown in Fig. 6.18. The time taken by V_{EH} to reach up to 5 V is $t_{\mathrm{C_{EH}}} = 11.12$ s, and hence the energy harvested per $t_{\mathrm{C_{EH}}}$ is 11.24 μW.

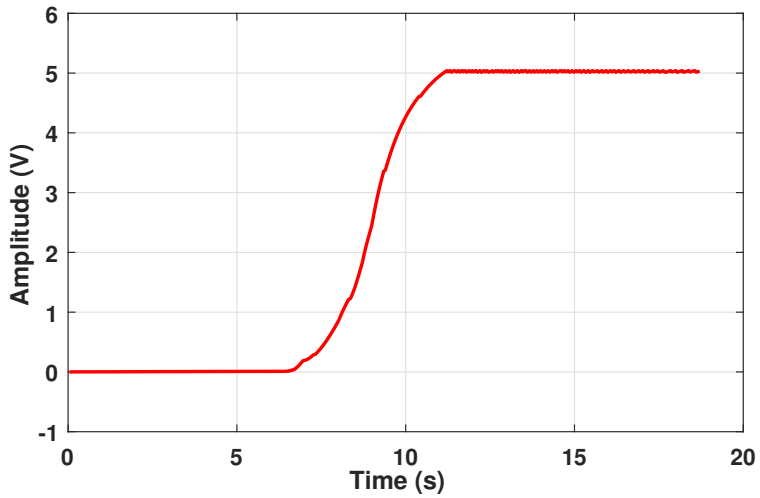

Figure 6.18: Voltage across C_{EH} obtained from human palm.

6.7 Discussion

In this chapter, we proposed the *e*Sampling ADC architecture, which modifies the traditional sampling process of a S/H ADC to harvest energy from the discarded portion of the input signal. We analyzed the amount of energy which can be harvested from stationary signals and characterized the underlying fundamental tradeoff between energy harvested and reconstruction fidelity which arises from the joint acquisition and energy harvesting paradigm. Then, we presented a circuit-level design of an *e*Sampling ADC using CMOS 65 nm technology. Our numerical results demonstrate the potential of *e*Sampling in realizing ADCs operating with high resolution and near ideal reconstruction accuracy

while harvesting the amount of energy which approaches and can even surpass that consumed in ADC operation. Similar results were observed in an experimental study dedicated to design *e*Sampling ADC circuit, indicating potential of self-powered ADCs.We have numerically demonstrated that an *e*Sampling ADC with up to 12 bits can harvest more power than it consumes, while sampling at Nyquist condition. The result has been validated on a circuit-level design of an *e*Sampling 8-bit ADC, which is shown to harvest more power than it consumes while allowing to recover the analog signal in a nearly perfect manner. Finally, we have provided a proof-of-concept, by designing the hardware of *e*Sampling, which is demonstrated at sensing element for both environment and health monitoring application.

Chapter 7

Integrated data and energy gathering using *e*Sampling for correlated stochastic signals

7.1 Introduction

Physical signals are analog in nature, taking values in continuous sets over a CT interval. Analog-to-digital converter (ADC) allows the discrete-time (DT) representation of the analog signals using the sampling process, followed by its digital representation using the quantization process. It is possible to reconstruct the analog signal from its digital representation by utilizing the fundamental Shannon-Nyquist paradigm [141] with high quantization resolution, if the signal is uniformly sampled with a sampling rate of at least twice the signal bandwidth. However, the power dissipation of ADC grows with the sampling rate and the quantization resolution, and hence the amount of available power

limits the ability to accurately represent the acquired signal [93]. The recent developments in signal processing allow to reconstruct the signal at lower quantization resolution [142–149] as well as lower sampling rate [5–9, 15–19, 150] by exploiting the a-prior knowledge, and thus overcome the power dissipation to some extent.

The low resolution hardware-limited quantization has been proposed in literature for various applications such as multiple input multiple-output (MIMO) communication systems [142, 143] channel estimation [144, 145], subspace estimation [146, 147], and direction of arrival (DOA) estimation [148, 149]. Additionally, in scenarios where the signal is acquired for some task, i.e., to recover some underlying information, not the entire signal, task-based quantizers have been also proposed, which can recover the desired information from the output of low resolution ADCs [100–104, 125, 151–153].

The area of compressed sensing gives rise to sub-Nyquist sampling [5, 6], which exploits the underlying structure of the analog signal to allow reconstruction from its low rate sampled version [7–9]. The effect of sub-Nyquist sampling has been studied in various applications, such as channel capacity [15–17], channel estimation [150], source coding [18, 19]. Unlike these works, where a single scalar signal is sampled and reconstructed, there exist multiple applications such as autonomous vehicles, radar, and communication receivers, where multiple signals are acquired simultaneously. Thus, results in a correlation between the observed analog signals, and hence introducing additional information which can be utilized to obtain accurate reconstruction at lower sampling

rates. The sampling of multiple deterministic signals was studied in the recent works [151, 154], which modeled correlation as the ability to represent each of the observed signals by a linear ensemble of a smaller amount of signals. Conditions for perfect recovery of deterministic multidimensional signals from their projections were studied in [152]. Moreover, sub-Nyquist sampling of the random signal has also been proposed [153], which focused on linear reconstruction. However, [125] proposed a multi-rate interpolation scheme. In previous work [100], we have provided an understanding of how general correlation contributes to the ability to reconstruct a set of acquired signals when sampling below the Nyquist rate.

It is to be noted that in above mentioned works, sampling rate and quantization resolution have been reduced, which result in a reduction in the power dissipation of the ADC. However, in previous chapter 6, a method named as *e*Sampling has been proposed [155], which shows that even by sampling at Nyquist rate and quantizing at high resolution, we can harvest energy from the input analog signal. This work extends the structure of sample-and-hold (S/H) ADC without altering its conversion procedure, while harvesting energy from the analog signal during the time periods where the signal is not being tracked [155]. In S/H architectures, the circuit used to sample the input analog signal consists of two phases in each sampling period, *acquisition phase* and *hold phase*. In the acquisition phase, the S/H circuit tracks the input analog signal. The sampled value captured in the acquisition phase is then converted into digital form, i.e., a sequence of bits, during hold phase. Therefore, during the

sampling process of S/H ADCs, the input signal is processed only for a fraction of the overall sampling period (acquisition phase) and is neglected/discarded for the remaining time interval (hold phase). The fact that the signal is not accessed in a dominant portion of the sampling period motivates the extension of S/H ADCs to continuously utilize the analog signal in order to mitigate power consumption. Additionally, the amount of energy harvested can be increased by reducing the sampling rate, however reducing the sampling rate also impacts the reconstruction accuracy. This work focused on a single input signal. However, by exploiting the joint acquisition in multiple correlated signals, the sampling frequency can be reduced without compromising the reconstruction accuracy, and hence the amount of energy harvested can be increased. Additionally, the joint sampling system can also reduce the hardware cost and energy consumption by reducing the number of required ADCs. To meet this goal, in this paper, we have extended our previous work for joint acquisition and reconstruction of multiple correlated sources [100], in context of maximizing the energy ratio, i.e., the amount of energy harvested and the amount of energy consumed by exploiting *e*Sampling structure.

Here we study a joint framework of sampling, energy harvesting and the reconstruction of the correlated CT sources. By focusing on stochastic signals, we adopt the standard notion of correlation, namely, the joint second-order statistical moments of these signals, and in particular, their cross PSD. We model joint *e*sampling and reconstruction as multivariate linear operations with intermediate uniform sampling. Under this model, we characterize the achievable

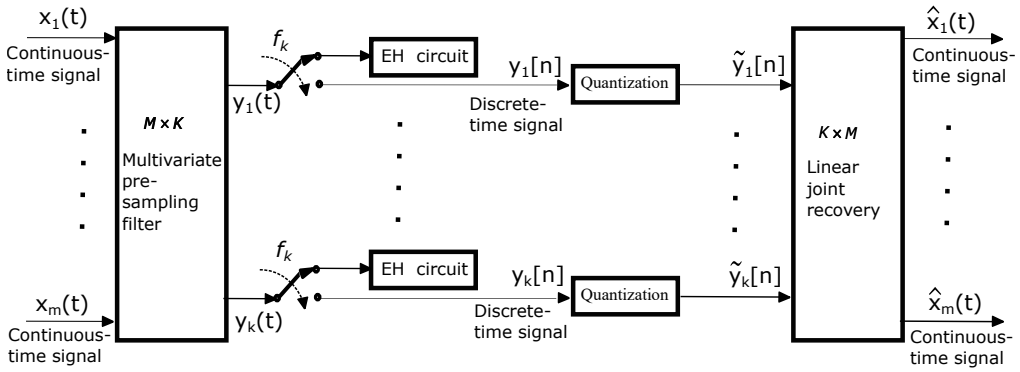

Figure 7.1: System model

NMSE, maximum harvested energy from the observed analog signals, and the corresponding configuration of the sampling system for arbitrary sampling rates, without restricting our attention to bandlimited signals. The proposed system mitigates the error induced by sub-Nyquist sampling by preserving the dominant eigenmodes among all aliased components and hence allow us to harvest more energy while maintaining the reconstruction accuracy. The resulting characterization of the achievable recovery accuracy is used to derive sufficient conditions for error-free recovery.

The rest of this chapter is organized as follows: Section 7.2 presents the system model and problem formulation. Section 7.3 derives the joint *e*sampling system, which optimizes the reconstruction accuracy and the amount of energy harvested. Numerical examples are discussed in Section 7.4.

7.2 System model

In this section, we study the joint *e*Sampling and reconstruction of M CT zero-mean jointly wide-sense stationary (WSS) random signals $\{x_m(t)\}_{m=1}^{M}$, $t \in \mathcal{R}$,

using K samplers and K quantizers such that $K < M$ as depicted in Fig. 7.1. Here, acquisition is carried out in a joint manner, where the input to each of the K uniform samplers is a linear combination of the outputs of M scalar filters, i.e., for each $k \in \{1, \ldots, K\} \triangleq \mathcal{K}$, the input to the kth sampler can be written as

$$y_k(t) = \sum_{m=1}^{M} (h_{k,m} \star x_m)(t) \tag{7.1}$$

for some set of scalar filters $\{h_{k,m}(t)\}$. This joint filtering is modeled as an $K \times M$ multivariate filter with frequency response $\boldsymbol{H}(f)$, $f \in \mathcal{R}$, where $(\boldsymbol{H}(f))_{k,m}$ is the Fourier transform of $h_{k,m}(t)$ for each $k \in \mathcal{K}$, $m \in \{1, \ldots, M\} \triangleq \mathcal{M}$. The outputs of this filter are *e*sampled at a uniform sampling rate f_s to form the DT signals $\{y_k[n]\}_{k=1}^{K}$, $n \in \mathcal{Z}$. We use $T_s = \frac{1}{f_s}$ to denote the sampling period. Further, the total sampling rate is $f_s^{\text{tot}} \triangleq K \cdot f_s$. In our previous work, we have designed an *e*Sampler, which allows to harvest the energy during the sampling process [155]. The sampling period of the sampling process is divided into two phases, acquisition phase, represented as T_{aq} and the hold phase, given by $T_s - T_{aq}$. The acquisition phase tracks the input analog signal to provide the discrete sample, however the hold phase allows the ADC to provide the digital representation, corresponding to the discrete sample. It is to be noted that during hold phase, the input analog signal is not tracked, and hence not utilized. Therefore, *e*Sampler extends the conventional architecture of S/H ADC to harvest the energy during hold phase, without altering the conventional conversion procedure [155]. Utilizing the concept of *e*Sampling, the total amount of energy harvested per sampling period in joint sampling system depicted in Fig. 7.1 is

given by [155]

$$\mathcal{E} = \eta(T_s - T_{aq}) \sum_{k=1}^{K} E\{|y_k(t)|^2\}, \tag{7.2}$$

where $\eta \in [0, 1]$ is the efficiency of the energy harvesting system. The amount of energy consumed in the system as illustrated in Fig. 7.1 is dependent on the analog circuits used in the system, i.e., filter $\boldsymbol{H}$, samplers and the quantizers. It is to be noted that, we have neglected the amount of energy consumed by the analog filter, as it is entirely design dependent, which is not the scope of this work. However, the total energy consumed during sampling and quantization can be modelled as second-order polynomial function of the supply voltage, V_{ref}, and is given by [155]

$$E_{\text{cons}} = K(a_1(n)V_{\text{ref}} + a_2(n)V_{\text{ref}}^2). \tag{7.3}$$

The coefficients $a_1(n)$ and $a_2(n)$ in (7.3) are positive constants determined by the number of bits n and the quantization circuit parameters, and can grow dramatically with n. Furthermore, the amount of energy consumed $E\text{cons}$ also increases linearly with the number of samplers or quantizers, i.e., K (7.3). This makes energy consumption a major bottleneck, motivating the proposed joint *e*Sampling and reconstruction, which increases the amount of energy harvested and reduces the amount of energy consumed, while maintaining the reconstruction accuracy. It is to be noted that, the V_{ref} used in (7.3) can be written as a combination of a scalar $K_p > 1$, the output signal power of the multivariate filter and K, i.e., $V_{\text{ref}}^2 = \frac{K_p^2}{K}\text{Tr}\left(E\left\{|y(t)|^2\right\}\right)$, where $y(t)$ is the output of the filter $h(t)$ [155]. This general formulation allows us to relate the reference voltage

with the overload probability of the quantizer, since the overload probability satisfies $P(|y_k(t)| \geq V_{\text{ref}}) \leq K_p^{-2}$ by Chebyshev's inequality [101]. Therefore, the ratio between the energy harvested (7.2) and consumed (7.3) for joint *e*Sampling of multiple WSS signals can be written as

$$\xi = \frac{\eta(T_s - T_{aq})\text{Tr}\left(E\left\{|y(t)|^2\right\}\right)}{a_1(n)K_p\sqrt{K\text{Tr}\left(E\left\{|y(t)|^2\right\}\right)} + a_2(n)K_p^2\text{Tr}\left(E\left\{|y(t)|^2\right\}\right)} \tag{7.4}$$

The CT signals $\{x_m(t)\}_{m=1}^M$ are jointly reconstructed from their sampled versions $\{y_k[n]\}_{k=1}^K$, yielding the recovered signals $\{\hat{x}_m(t)\}_{m=1}^M$. We focus on *shift-invariant linear joint recovery* [125], namely, the recovered signals can be written as

$$\hat{x}_m(t) = \sum_{k=1}^{K}\sum_{n\in\mathcal{Z}} g_{m,k}\left(t - nT_s\right)\cdot y_k[n], \quad m \in \mathcal{M}, \tag{7.5}$$

where $\{g_{m,k}(t)\}$ are a set of CT functions. Let $\boldsymbol{G}(f)$ be an $M \times K$ matrix such that $(\boldsymbol{G}(f))_{m,k}$ is the Fourier transform of $g_{m,k}(t)$, $m \in \mathcal{M}$, $k \in \mathcal{K}$. Note that when recovering $x_m(t)$, the system can utilize samples from all $\{x_m(t)\}_{m=1}^M$, thus exploiting possible correlation between the signals. Since the recovered signals $\{\hat{x}_m(t)\}_{m=1}^M$ are jointly *wide-sense cyclostationary* [125], the recovery accuracy is measured via the *TNMSE*, defined as

$$\zeta \triangleq \frac{1}{T_s}\frac{\sum_{m=1}^{M}\int_0^{T_s} E\left\{|x_m(t) - \hat{x}_m(t)|^2\right\}dt}{\sum_{m=1}^{M} E\left\{|x_m(t)|^2\right\}}. \tag{7.6}$$

Our goal is to determine the achievable TNMSE i.e., ζ (7.6) and the maximum harvested energy, i.e., $\mathcal{E}$ (7.2) for the system illustrated in Fig. 7.1, and to

characterize the optimal analog filters $\boldsymbol{H}(f)$ and reconstruction functions $\boldsymbol{G}(f)$. The motivation for this model stems from its ability to *jointly combine* the signals in acquisition and reconstruction, allowing the resulting system to exploit spatial correlation in order to improve the recovery accuracy at lower sampling rate, and hence improves the energy ratio by increasing the harvested energy and decreasing the energy consumption.

The system model bears similarity to that considered in [156]. However, while [156] studied conditions under which the reconstruction functions $\boldsymbol{G}(f)$ can achieve error-free recovery for fixed $\boldsymbol{H}(f)$ for uncorrelated bandlimited sources with f_s^{tot} being larger than M times the Nyquist rate, we consider the design of the overall joint sampling system such that the TNMSE is minimized, even when error-free recovery cannot be achieved. In particular, perfect reconstruction is clearly achievable when $M = K$, the signals $\{x_m(t)\}_{m=1}^M$ are bandlimited, and the sampling rate f_s satisfies Nyquist criterion. Hence, in the following, we are more interested in the sub-Nyquist regime, i.e., either the signals are not bandlimited, or sampling is carried out below the Nyquist rate. Under this regime, we study how the correlation between the signals can be exploited to facilitate their joint recovery.

7.3 Joint *e*Sampling and Reconstruction

In this section we study the achievable TNMSE and the amount of harvested energy for the system presented in Section 7.2. We first characterize the analog

filters and reconstruction functions which minimize the TNMSE for a given sampling rate f_s in Subsection 7.3.1. Then, we identify conditions for error-free recovery in Subsection 7.3.2. Finally, in Subsection 7.3.3 we determine the maximum amount of energy harvested, while maintaining the TNMSE derived in Subsection 7.3.1.

7.3.1 Minimizing TNMSE

To characterize the achievable TNMSE, we define the multivariate processes $\mathbf{x}(t) \triangleq \big[x_1(t),\ldots,x_M(t)\big]^T$ and $\mathbf{y}[n] \triangleq \big[y_1[n],\ldots,y_K[n]\big]^T$. Let $\boldsymbol{S}_{\mathbf{x}}(f)$ denote the $M \times M$ PSD of the multivariate WSS process $\mathbf{x}(t)$, i.e.,

$$\boldsymbol{S}_{\mathbf{x}}(f) \triangleq \int_{-\infty}^{\infty} E\{\mathbf{x}(t+\tau)\mathbf{x}^H(t)\}e^{-j2\pi f\tau}d\tau. \tag{7.7}$$

Using these notations, we characterize the achievable TNMSE for a given $\boldsymbol{H}(f)$ and f_s in the following lemma:

Lemma 1 *For a fixed $\boldsymbol{H}(f)$ and f_s, the reconstruction functions $\boldsymbol{G}_{\mathrm{o}}(f)$ which minimize (7.6) satisfy*

$$\boldsymbol{G}_{\mathrm{o}}(f)\boldsymbol{Q}_{\boldsymbol{H}}(f) = \boldsymbol{S}_{\mathbf{x}}(f)\boldsymbol{H}^H(f), \tag{7.8a}$$

where $\boldsymbol{Q}_{\boldsymbol{H}}(f)$ is the $K \times K$ matrix

$$\boldsymbol{Q}_{\boldsymbol{H}}(f) \triangleq \sum_{l\in\mathcal{Z}} \boldsymbol{H}\big(f-lf_s\big)\boldsymbol{S}_{\mathbf{x}}\big(f-lf_s\big)\boldsymbol{H}^H\big(f-lf_s\big). \tag{7.8b}$$

The resulting TNMSE is given by

$$\zeta_{\boldsymbol{H}}\left(f_s\right)=\frac{\int_{-\infty}^{\infty}\mathrm{Tr}\left(\boldsymbol{S}_{\mathbf{x}}(f)-\boldsymbol{S}_{\mathbf{x}}(f)\boldsymbol{H}^H(f)\boldsymbol{G}_{\mathrm{o}}^H(f)\right)df}{\int_{-\infty}^{\infty}\mathrm{Tr}\left(\boldsymbol{S}_{\mathbf{x}}(f)\right)}. \tag{7.8c}$$

It follows from (7.8a) that when $\boldsymbol{Q}_{\boldsymbol{H}}(f)$ is invertible for each frequency $f \in [-f_s/2, f_s/2) \triangleq \mathcal{F}_K$ for which $\boldsymbol{S}_{\mathbf{x}}(f) \neq \mathbf{0}$, the reconstruction filters which minimize (7.6) can be obtained in closed form as $\boldsymbol{G}_{\mathrm{o}}(f) = \boldsymbol{S}_{\mathbf{x}}(f)\boldsymbol{H}^H(f)\boldsymbol{Q}_{\boldsymbol{H}}^{-1}(f)$. Since $\boldsymbol{Q}_{\boldsymbol{H}}(f)$ is periodic with period f_s, this condition is equivalent to $\boldsymbol{Q}_{\boldsymbol{H}}(f)$ being non-singular whenever $\boldsymbol{S}_{\mathbf{x}}\left(f_{\mathrm{mod}f_s}\right) \neq \mathbf{0}$.

We are now ready to derive the achievable TNMSE and the corresponding sampling system. Let $\lambda_i(f)$ and $\mathbf{u}_i(f)$ be the ith largest eigenvalue of $\boldsymbol{S}_{\mathbf{x}}(f)$ and its corresponding eigenvector, respectively, and define $\mathcal{S}(f) \triangleq \{\lambda_i(f - lf_s)\}_{i\in\mathcal{M};l\in\mathcal{Z}}$. For each $f \in \mathcal{F}_K$, the set $\mathcal{S}(f)$ contains the eigenvalues of all the multivariate spectral components aliased to the frequency f after uniform sampling with rate f_s. Additionally, for any $f \in \mathcal{F}_K$ we use $\{\tilde{\lambda}_j(f)\}_{j\in\mathcal{N}}$ to denote the elements of the set $\mathcal{S}(f)$ arranged in a descending manner, and $\{\tilde{\mathbf{u}}_j(f)\}_{j\in\mathcal{N}}$ to denote their corresponding eigenvectors. In particular, if for some $f \in \mathcal{F}_K$, it holds that $\lambda_{i_j}(f - l_j f_s)$ is the jth largest element of $\mathcal{S}(f)$, then $\tilde{\lambda}_j(f) = \lambda_{i_j}(f - l_j f_s)$ and $\tilde{\mathbf{u}}_j(f) = \mathbf{u}_{i_j}(f - l_j f_s)$. The achievable TNMSE and the corresponding joint sampling system are stated in the following theorem:

Theorem 3 *For a fixed sampling rate f_s and number of uniform samplers K, let $\tilde{\boldsymbol{H}}(f)$ be an $M \times K$ matrix whose jth column is $\tilde{\mathbf{u}}_j\left(f_{\mathrm{mod}f_s}\right)$ if there exists some $i \in \mathcal{M}$ such that $\lambda_i(f) = \tilde{\lambda}_j\left(f_{\mathrm{mod}f_s}\right)$, and zero otherwise. Among all filters*

$\boldsymbol{H}(f)$ for which $\boldsymbol{Q}_{\boldsymbol{H}}(f)$ is non-singular when $\boldsymbol{S}_{\mathbf{x}}\left(f_{\mathrm{mod} f_s}\right) \neq \mathbf{0}$, the analog filters which minimize the TNMSE are given by

$$\boldsymbol{H}_{\mathrm{o}}(f) = \boldsymbol{D}(f)\tilde{\boldsymbol{H}}^{H}(f), \tag{7.9a}$$

where $\boldsymbol{D}(f)$ is some non-singular $K \times K$ matrix periodic in f with period f_s. The reconstruction filters are given by

$$\boldsymbol{G}_{\mathrm{o}}(f) = \tilde{\boldsymbol{H}}(f)\boldsymbol{D}^{-1}(f). \tag{7.9b}$$

The resulting TNMSE can be written as

$$\zeta_{\mathrm{o}}\left(f_s\right) = 1 - \frac{\int_{-f_s/2}^{f_s/2} \sum_{j=1}^{K} \tilde{\lambda}_j(f) df}{\int_{-\infty}^{\infty} \mathrm{Tr}\left(\boldsymbol{S}_{\mathbf{x}}(f)\right) df}. \tag{7.9c}$$

It is emphasized that while $\boldsymbol{H}_{\mathrm{o}}(f)$ in (7.9a) minimizes the TNMSE among the analog filters for which $\boldsymbol{Q}_{\boldsymbol{H}}(f)$ is non-singular when $\boldsymbol{S}_{\mathbf{x}}\left(f_{\mathrm{mod} f_s}\right) \neq \mathbf{0}$, the resulting $\zeta_{\mathrm{o}}\left(f_s\right)$ is still obtained by the proposed system when $\boldsymbol{Q}_{\boldsymbol{H}}(f)$ which stems from $\boldsymbol{H}_{\mathrm{o}}(f)$ does not satisfy this condition.

The sampling system proposed in Theorem 3 operates in the following manner: Prior to sampling, the matrix $\tilde{\boldsymbol{H}}^{H}(f)$ preserves at each frequency $f \in \mathcal{F}_K$ the K eigenmodes corresponding the largest eigenvalues among frequency components which are aliased to that frequency after uniform sampling. By doing so, only a single aliased component is preserved at each spatial dimension, and the spectral overlapping induced by sampling is effectively canceled. At re-

construction, each of the preserved eignemodes is recovered, and the resulting estimation error is due to the weaker eigenmodes nullified by the system. The non-singular periodic matrix $\boldsymbol{D}(f)$ in Theorem 3 does not affect the overall TNMSE as it operates in the same manner on each aliased component of the PSD and can thus be compensated for in reconstruction.

To further clarify the structure of $\tilde{\boldsymbol{H}}(f)$, we consider the following example:

Example 3 *Consider a set of correlated inputs with multivariate PSD $\boldsymbol{S}_{\mathbf{x}}(f)$ sampled using $K = 4$ uniform samplers at sampling rate f_s. For some fixed $f_0 \in \mathcal{F}_K$, the four largest eigenvalues of the set $\mathcal{S}(f_0)$ are $\lambda_1(f_0)$, $\lambda_2(f_0)$, $\lambda_1(f_0 - f_s)$, and $\lambda_1(f_0 + f_s)$. Consequently, the matrix $\tilde{\boldsymbol{H}}(f)$, which dictates the structure of the $\boldsymbol{H}_{\mathrm{o}}(f)$ and $\boldsymbol{G}_{\mathrm{o}}(f)$, satisfies*

$$\begin{aligned}
\tilde{\boldsymbol{H}}(f_0) &= \begin{bmatrix} \mathbf{u}_1(f_0) & \mathbf{u}_2(f_0) & \mathbf{0} & \mathbf{0} \end{bmatrix}, \\
\tilde{\boldsymbol{H}}(f_0 - f_s) &= \begin{bmatrix} \mathbf{0} & \mathbf{0} & \mathbf{u}_1(f_0 - f_s) & \mathbf{0} \end{bmatrix}, \\
\tilde{\boldsymbol{H}}(f_0 + f_s) &= \begin{bmatrix} \mathbf{0} & \mathbf{0} & \mathbf{0} & \mathbf{u}_1(f_0 + f_s) \end{bmatrix},
\end{aligned}$$

while $\tilde{\boldsymbol{H}}(f_0 - kf_s) = \mathbf{0}$ for each integer $|k| > 1$.

Example 3 illustrates how, prior to sampling, the pre-sampling matrix perseveres only K dominant eigenmodes of the multivariate PSD among all frequencies aliased to f_0 after sampling. In the special case of $M = K = 1$, this reduces to saving the largest value among all aliased components at each frequency, which is the sampling mechanism of [157, Thm. 4]. However, for

$M > 1$, this standard mechanism is substantially outperformed by the joint sampling system of Theorem 3.

7.3.2 Conditions for Error-Free Reconstruction

We next use (7.9c) to identify when can one obtain error-free reconstruction (in the sense of zero TNMSE). A sufficient condition is stated in the following corollary:

Corollary 2 *The joint sampling system of Fig. 7.1 with K uniform samplers at rate f_s achieves zero TNMSE whenever at most K elements of $\mathcal{S}(f)$ are non zero for each $f \in \mathcal{R}$.*

A trivial special case of Corollary 2 is obtained by considering Nyquist sampling, i.e., $\boldsymbol{S}_{\mathbf{x}}(f) = \mathbf{0}$ for each $f \notin \mathcal{F}_K$. In this case, the set $\mathcal{S}(f)$ contains at most M non-zero elements. Thus, by Corollary 2, zero TNMSE reconstruction is achievable when the number of uniform samplers is equal to the number of inputs, $M = K$, settling with the conventional sampling theorem. Furthermore, when the input signals are linearly deterministically dependent, which is the setup considered in [151, 154], then $r \triangleq \max_{f \in \mathcal{R}} \left(\operatorname{rank} \left(\boldsymbol{S}_{\mathbf{x}}(f) \right) \right) < M$. In this case, as expected, Corollary 2 states that zero TNMSE can be achieved with Nyquist sampling using $K = r$ uniform samplers, since the input signals can be perfectly reconstructed from their lower dimensional projection.

7.3.3 Maximizing Energy harvested for Joint *e*Sampling system

While maintaining the achievable TNMSE obtained through Theorem 3, the amount of energy harvested from the observed analog signals in the joint *e*Sampling system, illustrated in Fig. 7.1, given in (7.2) can be re-written as

$$\mathcal{E}(f_s) = \eta(T_s - T_{aq}) \int_{-\infty}^{\infty} \mathrm{Tr}(\boldsymbol{H}_{\mathrm{o}}(f)\boldsymbol{S}_{\mathbf{x}}(f)\boldsymbol{H}_{\mathrm{o}}^{H}(f))df. \tag{7.10}$$

This energy harvested, which maintains the achievable TNMSE and also conditioned on the fact that the analog filter must not contribute towards energy harvesting can be maximized by the solution to the following optimization problem:

$$\begin{aligned} \mathcal{E}_{\mathrm{o}}(f_s) = \eta(T_s - T_{aq}) \max_{\boldsymbol{D}(f)} & \int_{-\infty}^{\infty} \mathrm{Tr}(\boldsymbol{H}_{\mathrm{o}}(f)\boldsymbol{S}_{\mathbf{x}}(f)\boldsymbol{H}_{\mathrm{o}}^{H}(f))df \\ \text{s.t.} \quad & \boldsymbol{D}(f) = \boldsymbol{D}(f + f_s), \quad \forall f \in \mathcal{R} \\ & \mathrm{rank}\,(\boldsymbol{D}(f)) = K, \quad \forall f \in (-f_s/2, f_s/2). \\ & \int_{-\infty}^{\infty} \mathrm{Tr}(\boldsymbol{H}_{\mathrm{o}}(f)\boldsymbol{S}_{\mathbf{x}}(f)\boldsymbol{H}_{\mathrm{o}}^{H}(f))df \leq \int_{-\infty}^{\infty} \mathrm{Tr}(\boldsymbol{S}_{\mathbf{x}}(f))df. \end{aligned} \tag{7.11}$$

Theorem 4 *For a fixed sampling rate f_s and number of samplers K, the maximum amount of energy harvested from M input signals, while satisfying the criteria of minimum achievable TNMSE provided in Theorem 3 is given by*

$$\begin{aligned} \mathcal{E}_{\mathrm{o}}(f_s) =& \eta(T_s - T_{aq}) \\ & \int_{-f_s/2}^{f_s/2} \tilde{\lambda}_{\max}(f)(1 - K\epsilon) + \epsilon \sum_{k} \tilde{\lambda}_k(f)df \end{aligned} \tag{7.12}$$

As ϵ is small, this can be approximated as

$$\mathcal{E}_{\mathrm{o}}(f_s) = \eta(T_s - T_{aq}) \int_{-f_s/2}^{f_s/2} \tilde{\lambda}_{\max}(f) df \tag{7.13}$$

Proof: See Appendix 7.5.1.

Corollary 3 *Theorem 4 also implies, the ratio between the amount of energy harvested and consumed (7.4) for the system illustrated in Fig. 7.1 can be written as*

$$\xi_{\mathrm{o}} = \frac{\eta(T_s - T_{aq}) \int_{-f_s/2}^{f_s/2} \sqrt{\tilde{\lambda}_{\max}(f)} df}{a_1(n) K_p \sqrt{K} + a_2(n) K_p^2 \int_{-f_s/2}^{f_s/2} \sqrt{\tilde{\lambda}_{\max}(f)} df}. \tag{7.14}$$

7.4 Numerical Study

In this section we numerically evaluate the performance of the joint *e*sampling system studied in Section 7.3. We computed the achievable time-averaged NMSE of the joint *e*sampling system derived in Theorem 3 with respect to the energy ratio, ξ shown in Corollary 3 by varying f_s^{tot} from 1 MHz to 40 MHz. The scalar analog filters are set according to [157, Thm. 4]. The value of coefficients $a_1(n)$ and $a_2(n)$ are set according to [155, (27)] by considering the value for all the capacitance to be 200 fF. We set the efficiency of the energy harvesting system η to 0.5, which is in line with similar values reported for energy harvesting circuits in [136–138]. Also, we use $K_p = 10$, guaranteeing a probability of over 99% for all samplers that $|y_k(t)| \leq V_{\mathrm{ref}}\ \forall\ k$, and hence the

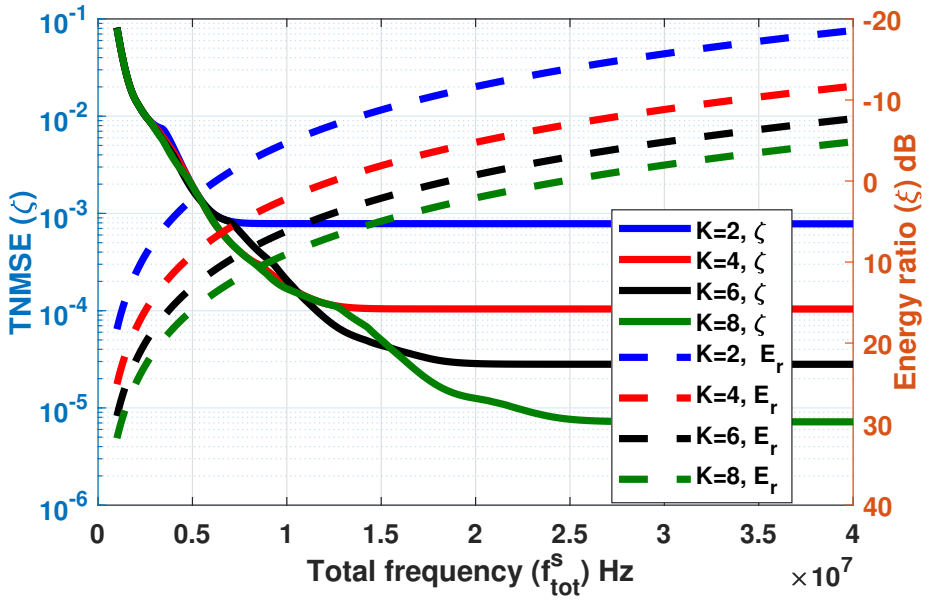

Figure 7.2: Time-averaged sum TNMSE and E_r versus f_s^{tot}, unimodal PSD.

accuracy is not compromised by quantizer overloading. Additionally, the acquisition time T_{aq} is set to be the 10% of the T_s [155]. Furthermore, we consider a set of $M = 10$ non-bandlimited jointly WSS signals $\{x_k(t)\}_{k=1}^{M}$. To formulate the multivariate PSD $\boldsymbol{S}_{\mathbf{x}}(f)$, we define an $M \times M$ matrix $\boldsymbol{P}(f)$, and set $\boldsymbol{S}_{\mathbf{x}}(f) = \boldsymbol{P}(f)\boldsymbol{P}(f)^H$. We have considered following setting for $\boldsymbol{P}(f)$

- *Unimodal PSD*: Here we set $(\boldsymbol{P}(f))_{k,l} = \sqrt{a_{k,l}}e^{-a_{k,l}f^2}$ where $a_{k,l} \triangleq \alpha \cdot \min(k,l)$ and $\alpha = 10^{-6}$. It is noted that the parameter $a_{k,l}$ and particularly the value of α, affects the shape of the PSD.

- *Multimodal PSD*: Under this setting, $(\boldsymbol{P}(f))_{k,l} = \sqrt{a_{k,l}}e^{-a_{k,l}(f-f_{k,l})^2}$ where $a_{k,l}$ is defined above and $f_{k,l} \triangleq (1 + 0.2 \cdot \min(k,l))10^6$.

Fig. 7.2 computes the TNMSE (ζ) and energy ratio (E_r) against different values of the total sampling frequency (f_s^{tot}) for 16-bit ADC with unimodal PSD. The results have been computed for $K = 2, 4, 6$ and 8. From graph,

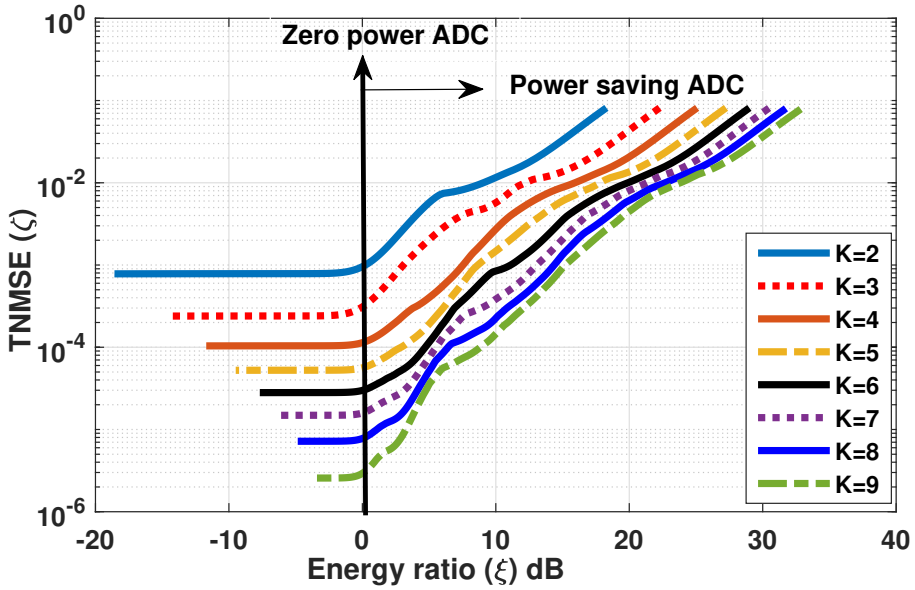

Figure 7.3: Time-averaged sum TNMSE versus f_s^{tot}, unimodal PSD.

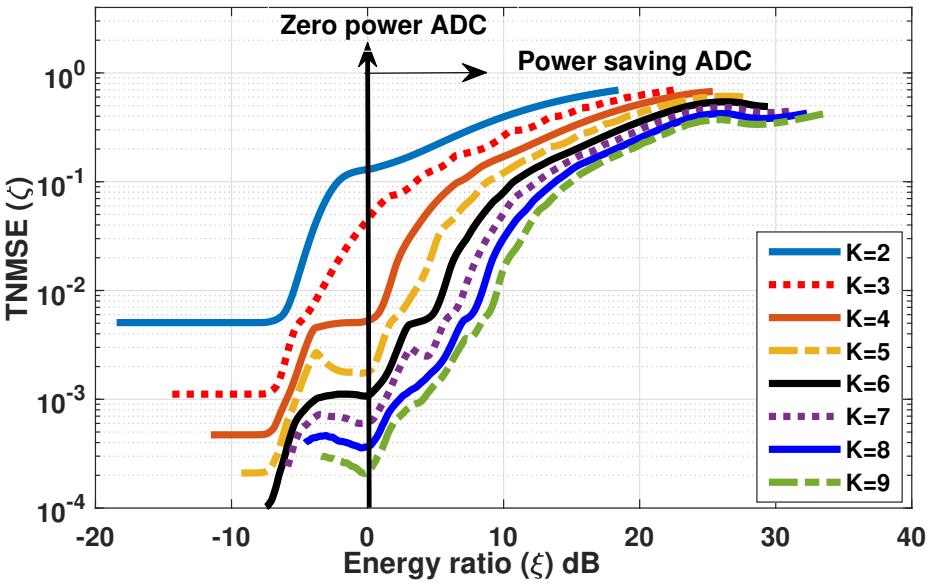

Figure 7.4: Time-averaged sum TNMSE versus f_s^{tot}, multimodal PSD.

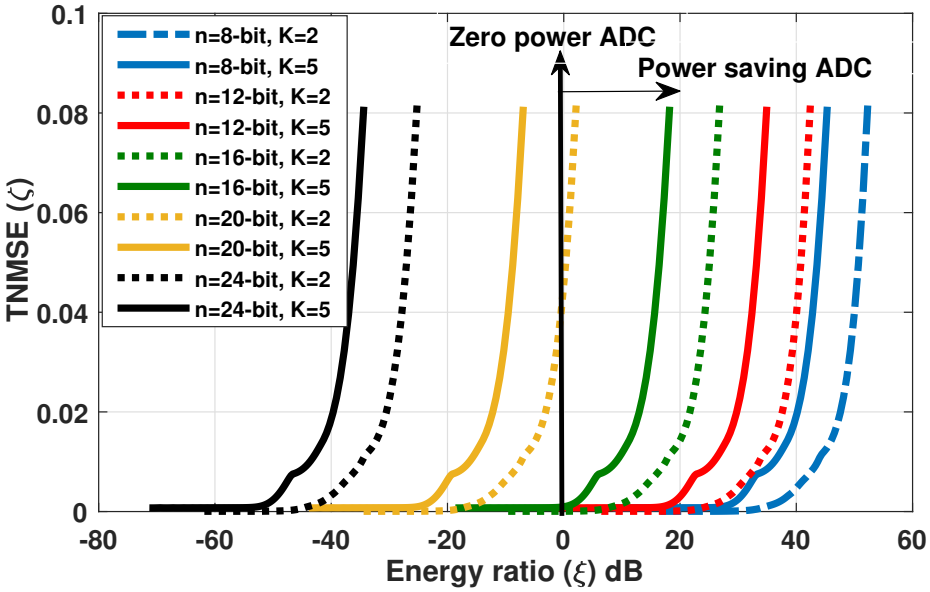

Figure 7.5: Time-averaged sum TNMSE versus f_s^{tot}, unimodal PSD.

we can observe increasing the sampling frequency reduces the TNMSE and also reduces the energy gain. To bring more insights, in Fig. 7.3 and 7.4, the TNMSE has been computed against ξ, for different value of K varying from 2 to 9, while considering 16-bit ADC. From Fig. 7.3, it is to be observed that TNMSE of around 10^{-3} and 10^{-4} has been obtained for unimodal PSD at $K = 2$ and $K = 4$, respectively, while the system is operating at zero power since the amount of energy harvested is same as the amount of energy consumed. Similarly, a multimodal PSD can achieve TNMSE of less than 10^{-2} and of around 10^{-3}, for $K = 4$ and $K = 6$, respectively for zero power ADC. We can also harvest more energy than consumed to obtain power saving ADCs, however, it leads to increment in TNMSE. Similarly, to improve reconstruction accuracy, we need to compromise the energy, and hence there is a trade-off.

In Fig. 7.5, we have computed the TNMSE against ξ, by varying f_s^{tot} for different n bits and also for $K = 2, 5$ by considering unimodal PSD. It can be

observed that for $n \leq 16$ bits, we can operate the ADC at zero power, while achieving minimal TNMSE.

7.5 Appendix

7.5.1 Proof of Theorem 4

The objective function given in (7.11), i.e., $\int_{-\infty}^{\infty} \text{Tr}(\boldsymbol{H}_{\text{o}}(f)\boldsymbol{S}_{\mathbf{x}}(f)\boldsymbol{H}_{\text{o}}^{H}(f))df$ can be re-written as

$$
\begin{aligned}
&= \text{Tr}\left(\int_{-\infty}^{\infty} \boldsymbol{H}_{\text{o}}(f)\boldsymbol{S}_{\mathbf{x}}(f)\boldsymbol{H}_{\text{o}}^{H}(f)df\right) \\
&= \text{Tr}\left(\sum_{k=-\infty}^{\infty}\int_{-f_s/2}^{f_s/2} \boldsymbol{H}_{\text{o}}(f-kf_s)\boldsymbol{S}_{\mathbf{x}}(f-kf_s)\right. \\
&\qquad\qquad \left.\boldsymbol{H}_{\text{o}}^{H}(f-kf_s)df\right) \\
&\overset{(a)}{=} \text{Tr}\left(\int_{-f_s/2}^{f_s/2}\sum_{k=-\infty}^{\infty} \boldsymbol{D}(f-kf_s)\tilde{\boldsymbol{H}}(f-kf_s)\boldsymbol{S}_{\mathbf{x}}(f-kf_s)\right. \\
&\qquad\qquad \left.\tilde{\boldsymbol{H}}^{H}(f-kf_s)\boldsymbol{D}^{H}(f-kf_s)df\right) \\
&\overset{(b)}{=} \text{Tr}\left(\int_{-f_s/2}^{f_s/2} \boldsymbol{D}(f)\left(\sum_{k=-\infty}^{\infty} \tilde{\boldsymbol{H}}(f-kf_s)\boldsymbol{S}_{\mathbf{x}}(f-kf_s)\right.\right. \\
&\qquad\qquad \left.\left.\tilde{\boldsymbol{H}}^{H}(f-kf_s)\right)\boldsymbol{D}^{H}(f)df\right) \\
&\overset{(c)}{=} \text{Tr}\left(\int_{-f_s/2}^{f_s/2} \boldsymbol{D}(f)\tilde{\boldsymbol{\Lambda}}(f)\boldsymbol{D}^{H}(f)df\right) \\
&= \int_{-f_s/2}^{f_s/2} \text{Tr}\left(\boldsymbol{D}(f)\tilde{\boldsymbol{\Lambda}}(f)\boldsymbol{D}^{H}(f)\right)df, \qquad (7.5.1.1)
\end{aligned}
$$

where $\tilde{\mathbf{\Lambda}}(f)$ is a $K \times K$ diagonal matrix whose jth diagonal entry is $\tilde{\lambda}_j(f)$ defined in Theorem 3. Here, (a) follows from (7.9a); (b) follows from the f_s-periodicity of $\boldsymbol{D}(f)$; and (c) stems from the definition of $\tilde{\boldsymbol{H}}(f)$. Furthermore, the constraint $\int_{-\infty}^{\infty} \mathrm{Tr}(\boldsymbol{H}_{\mathrm{o}}(f)\boldsymbol{S}_{\mathbf{x}}(f)\boldsymbol{H}_{\mathrm{o}}^{H}(f))df \leq \int_{-\infty}^{\infty} \mathrm{Tr}(\boldsymbol{S}_{\mathbf{x}}(f))df$ given in (7.11) can be understood as follows:

For all $\boldsymbol{H}$, at k^{th} sampler,

$$y_k(t) = \sum_{m=1}^{M} (h_{k,m} \star x_m)(t) \tag{7.5.1.2}$$

The amount of power received at k^{th} sampler is given by

$$|y_k(t)|^2 = \left| \sum_{m=1}^{M} (h_{k,m} \star x_m)(t) \right|^2 \tag{7.5.1.3}$$

Furthermore,

$$\begin{aligned} |Y_k(f)|^2 &\overset{(a)}{=} \left| \sum_{m=1}^{M} (H_{k,m}(f) X_m(f)) \right|^2 \\ &\overset{(b)}{\leq} \sum_{m=1}^{M} |H_{k,m}|^2(f) \sum_{m=1}^{M} |X_m|^2(f). \end{aligned} \tag{7.5.1.4}$$

Here, (a) is frequency domain representation of (7.5.1.3) and (b) follows from Cauchy–Schwartz inequality. Additionally, the total amount of energy harvested from all the K samplers will be given by

$$\sum_{k=1}^{K} |Y_k(f)|^2 \leq \left(\sum_{k=1}^{K} \sum_{m=1}^{M} |H_{k,m}|^2(f) \right) \left(\sum_{m=1}^{M} |X_m|^2(f) \right). \tag{7.5.1.5}$$

This implies

$$\frac{\sum_{k=1}^{K}|Y_k(f)|^2}{\left(\sum_{m=1}^{M}|X_m|^2(f)\right)} \leq \left(\sum_{k=1}^{K}\sum_{m=1}^{M}|H_{k,m}|^2(f)\right). \tag{7.5.1.6}$$

Additionally, to design any generic energy conservative filter, following should be satisfied

$$\frac{\sum_{k=1}^{K}|Y_k(f)|^2}{\left(\sum_{m=1}^{M}|X_m|^2(f)\right)} \leq 1. \tag{7.5.1.7}$$

In order to meet the conditions obtained in (7.5.1.7) and (7.5.1.6), we can conclude the following

$$\left(\sum_{k=1}^{K}\sum_{m=1}^{M}|H_{k,m}|^2(f)\right) \leq 1. \tag{7.5.1.8}$$

This implies $||\boldsymbol{H}(f)||_F^2 \leq 1$, and hence $\text{Tr}(\boldsymbol{H}(f)\boldsymbol{H}^H(f)) \leq 1$. Since $\text{Tr}(\boldsymbol{D}(f)\boldsymbol{D}^H(f)) \leq \text{Tr}(\boldsymbol{H}(f)\boldsymbol{H}^H(f))$, the constraint will become $\text{Tr}(\boldsymbol{D}(f)\boldsymbol{D}^H(f)) \leq 1$. And hence, using (7.5.1.1), the optimization framework (7.11) can be re-written as

$$\begin{aligned} &\max_{\boldsymbol{D}(f)} \int_{-f_s/2}^{f_s/2} \text{Tr}(\boldsymbol{D}(f)\tilde{\boldsymbol{\Lambda}}(f)\boldsymbol{D}^H(f))df \\ \text{s.t.} \quad &\text{rank}\left(\boldsymbol{D}(f)\right) = K, \quad \forall f \in (-f_s/2, f_s/2) \\ &\text{Tr}(\boldsymbol{D}(f)\boldsymbol{D}^H(f)) \leq 1. \end{aligned} \tag{7.5.1.9}$$

Note that the constraint on $\boldsymbol{D}(f)$ to be periodic is no longer needed as it is already encapsulated in how the objective is formulated. It should be noted that

(7.5.1.9) can be solved for each frequency separately. Namely, we need to solve

$$\begin{aligned} &\max_{\boldsymbol{D}(f)} \text{Tr}(\boldsymbol{D}(f)\tilde{\boldsymbol{\Lambda}}(f)\boldsymbol{D}^H(f)) \\ wd\text{s.t.} \quad &\text{rank}\,(\boldsymbol{D}(f)) = K, \\ &\text{Tr}(\boldsymbol{D}(f)\boldsymbol{D}^H(f)) \leq 1, \end{aligned} \tag{7.5.1.10}$$

for each $f \in (-f_s/2, f_s/2)$. In particular, the objective in (7.5.1.10) can be written as $\text{Tr}(\boldsymbol{D}^H(f)\boldsymbol{D}(f)\tilde{\boldsymbol{\Lambda}}(f))$. Since this is the trace of the product of Hermitian positive semi definite matrices and as $\tilde{\boldsymbol{\Lambda}}(f)$ is diagonal with decreasing elements along its main diagonal, it follows that the objective is maximized when $\boldsymbol{D}^H(f)\boldsymbol{D}(f)$ is diagonal with decreasing elements along its main diagonal [158]. By letting $d_k^2(f)$ be those diagonal elements, the problem boils down to

$$\begin{aligned} &\max_{\{d_k^2(f)>0\}} \sum_k d_k^2(f)\tilde{\lambda}_k(f) \\ &\text{s.t.} \sum_k d_k^2(f) \leq 1. \end{aligned} \tag{7.5.1.11}$$

Defining, $x_k(f) = d_k^2(f) - \epsilon$, (7.5.1.11) will become a simple linear problem as follows

$$\begin{aligned} &\max_{x_k(f)} \sum_k x_k(f)\tilde{\lambda}_k(f) + \epsilon\tilde{\lambda}_k(f) \\ &\text{s.t.} \sum_k x_k(f) \leq 1 - K\epsilon. \\ &x_k(f) \geq 0 \; \forall \; k \end{aligned} \tag{7.5.1.12}$$

The solution to this problem will be $x_k(f) = \begin{cases} 1 - K\epsilon & \text{at } k = \text{index of} \max(\tilde{\lambda}_k(f)) \\ 0 & \text{otherwise} \end{cases}$, and hence the maximum value of the problem is $\tilde{\lambda}_{\max}(f)(1 - K\epsilon) + \sum_k \epsilon \tilde{\lambda}_k(f)$, where $\tilde{\lambda}_{\max}(f) = \max(\tilde{\lambda}_1(f), \tilde{\lambda}_2(f), ...\tilde{\lambda}_K(f))$. This also implies $\boldsymbol{D}^H(f)\boldsymbol{D}$ is a diagonal matrix with first entry at the diagonal is $1 - K\epsilon + \epsilon$ and all other entries are zero.

Chapter 8

Conclusion and Future Work

8.1 Contributions and Impact

The main contributions of the dissertation are summarized below:

8.1.1 PCI based CS

CS has been used to recover the data at a lower sampling rate by exploiting the underlying structure of the analog signal. However, the conventionally linear combination of the data using Gaussian and Bernoulli matrices have been utilized for the compressive measurements. We propose to use PCI sensing matrix to obtain compressive measurements, which randomly picks the data instead of taking the linear combination of the data. Consequently, it reduces the complexity, latency, hardware cost and energy consumption. We have shown, if the data is sparse in the DCT or DFT domain, the PCI based CS improves the reconstruction performance as compared to the conventional methods.

It has been shown previously that WSN data is smoothly varying in both spatial and temporal domain, which results in sparsity in the DCT domain, and hence PCI-CS has been first exploited in WSN application. Further, in the presence of noise, the smoothness in the WSN data get affected, which impacts the level of sparsity, and hence the performance of PCI-CS. Therefore, a two-stage algorithm to de-noise the data has been proposed, which is the next contribution of this thesis, mentioned below.

8.1.2 A Two-stage algorithm: PCI-MF

The performance of PCI-CS method has been improved by introducing a two-stage algorithm, named as PCI-MF. This algorithm utilizes PCI-CS at the first stage to recover the sparsest solution and the rank of the data, which is used jointly in the second stage in a matrix factorization framework to recover the complete data.

It is observed that this framework resembles missing data recovery problems, as it can recover complete data with partial availability of the data. Therefore, this algorithm has been compared in the context of missing data recovery framework with the conventional and the recent state-of-the-art methods for WSN on the real data set of “Intel lab" and “data sensing lab". It has been observed that the proposed PCI-MF consistently outperforming the existing algorithms. Furthermore, at higher data loss of approximately 90%, an improvement of around 12dB has been observed, when compared to conventional missing data recovery methods for WSN application.

The robustness of PCI-MF has been further validated by utilizing it for estimating the mmWave massive MIMO communication channel from a few noisy channel coefficients. The performance of the method has been evaluated by calculating NMSE between the actual CSI and the recovered CSI. NMSE results show considerable improvement in performance with PCI-MF compared to the state-of-the-art methods. For further validating the PCI-MF, the NMSE is simulated with various parameters, such as different MIMO configurations, low and high values of SNR and MR, as well as different channel fading models. It is observed that PCI-MF consistently outperforms in different MIMO configurations such as 32×32, 64×64, for all values of SNR and also for all MR. The improvement in performance is observed with both ULA as well as UPA antenna configurations. The performance of PCI-MF is also shown by evaluating SER and ASE. It is observed that PCI-MF outperforms the existing methods and approaches the ASE values of perfect CSI. For instance, at 25 dB SNR, ASE of 16.49 bits/sec/Hz is obtained with perfect CSI for 32×32 MIMO configuration. Using PCI-MF, with only 30% availability of channel information, ASE of 16.09 bits/sec/Hz (close to perfect CSI) has been obtained. In order to validate the performance of PCI-MMF in realistic scenarios, another data set of New York City with real-world outdoor cellular propagation parameters has also been considered. It is observed that even in a practical scenario when transmitter and receiver are 100 m apart, PCI-MF obtains 5.45 dB and 16.933 dB improvement with 10% and 90% availability of channel information, respectively, as compared to the existing methods.

8.1.3 iDEG: Integrated data and energy gathering for WSN

It is to be noted that in WSN, sensor node senses some physical parameter and produces an analog signal, which is sampled and digitized for further processing and transmission. In this thesis, we have first proposed an iDEG protocol for WSN. In this protocol, we have allowed only a fraction of sensor nodes to transmit the signal to the FC, and the rest of the nodes are utilized to harvest energy from the received analog signal itself. The proposed PCI-MF algorithm has been utilized at FC to recover the entire data of the WSN, and hence the energy harvesting procedure didn't affect the data reconstruction accuracy.

Results show that the proposed iDEG protocol not only reduces the complexity, sensing time, latency and energy losses but also provides better data recovery at FC as compared to various conventional sensing and routing strategies. The iDEG protocol also provides a method for harvesting the energy from the unused sensor nodes. Further, the proposed method is self-sufficient in recovering missing entries of the original data set as demonstrated through simulation on real data set of Intel lab.

8.1.4 *e*Sampling: Re-thinking sampling process with energy harvesting

In this thesis, we proposed the *e*Sampling ADC architecture, which modifies the traditional sampling process of a S/H ADC to harvest energy from the discarded portion of the input signal. We analyzed the amount of energy which can be harvested from stationary signals and characterized the underlying fun-

damental tradeoff between energy harvested and reconstruction fidelity which arises from the joint acquisition and energy harvesting paradigm. Then, we presented a circuit-level design of an *e*Sampling ADC using CMOS 65 nm technology. Our numerical results demonstrate the potential of *e*Sampling in realizing ADCs operating with high resolution and near ideal reconstruction accuracy while harvesting the amount of energy which approaches and can even surpass that consumed in ADC operation. Similar results were observed in an experimental study dedicated to design *e*Sampling ADC circuit, indicating the potential of self-powered ADCs. We have numerically demonstrated that an *e*Sampling ADC with up to 12 bits can harvest more power than it consumes while sampling at Nyquist condition. The result has been validated on a circuit-level design of an *e*Sampling 8-bit ADC, which is shown to harvest more power than it consumes while allowing to recover the analog signal in a nearly perfect manner.

To validate the *e*Sampling in real-world environment, we have also designed a hardware setup to sample and harvest the energy from the real world continuous-time input signal for WSN application on two different input signal; one is generated from the environment temperature and another from the human palm. As a proof of concept demonstration and performance assessment, the reconstructed signal obtained from the proposed work has been compared with the traditional sampling process. From experiments, it has been concluded that even 10% of the sampling time is sufficient to sample the data, and the remaining time can be allocated for energy harvesting. Furthermore, in the EH circuit,

the received voltage has been boosted to the 5 V so that it can be used in future to drive some application or to self-sustain the sensor node itself. The relative efficiency of around 70% has been obtained in the designed setup.

8.1.5 iDEG using *e*Sampling for multiple correlated stochastic signals

In this work, we studied joint *e*sampling and reconstruction of multiple correlated stochastic analog signals, while improving data reconstruction accuracy and the amount of harvested energy. We characterized the achievable TNMSE, maximum energy harvested from the observed analog signals for a given sampling rate and the corresponding joint *e*sampling system. We analyzed the amount of energy which can be harvested from signals and characterized the underlying fundamental tradeoff between energy harvested and reconstruction fidelity which arises from the joint acquisition and energy harvesting paradigm. We showed that the joint *e*sampling system could operate at sub-Nyquist sampling frequency by preserving the most dominant spatial eigenmodes among all spectral components aliased to the same frequency and hence allows the system to operate at zero power by harvesting more energy from the observed analog signals. We have numerically demonstrated that the joint *e*Sampling and reconstruction framework with 16 bits can harvest as much energy as it consumes, while sampling minimizing reconstruction error and also the number of samples required.

8.2 Future directions

In this section, we have elaborated the possible future directions of this dissertation.

8.2.1 Extension for PCI-MF

A few possible extensions of PCI-MF have been discussed below:

- It has been observed that the real signals are generally smoothly varying, and hence have sparsity in DCT and DFT domains, and also have dependencies, which results in low-rankness. Hence, the proposed PCI-MF algorithm can be utilized for various other real-world applications, such as biomedical applications, channel estimation for Unmanned Aerial Vehicle (UAV) applications etc.
- In this thesis, we have considered PCI-MF method for homogeneous networks, where all the nodes are identical. However, the PCI-MF will be extended for inhomogeneous field. The inhomogeneous network can be considered as a collection of two or more homogeneous regions separated by boundaries, and hence it may represents in either a multi-dimensional sparse framework or a weighted sparse framework, such that the estimated joint sparsifying domain has less correlation with the PCI matrix.
- The PCI-MF used for channel estimation in mmWave MIMO system can be extended for the multi-user MIMO systems, where the PCI-MF based

channel estimation will ease out the process of beam sweeping from base station to multiple user equipment. Further, we have assumed that AoA and AoD lie on the discretized grids. In future, PCI-MF can be extended to overcome this assumption.

8.2.2 Sub-Nyquist *e*Sampling at RF: A new Generation Receiver

A wireless receiver architecture consists of an analog RF front end circuit, followed by an ADC and the demodulation circuit. The analog RF front end down-converts the input signal to the baseband frequency, and also provides signal amplification and filtering to amplify the weak received signal, while rejecting the surrounding. If the ADC is placed at the RF, the amplification, down-conversion, and filtering can all be done in the digital domain. This results in a true software radio architecture, where maximum utilization of digital programmability is achieved. However, the speed and power limitations of ADCS limit the practical realization of such receivers. Therefore, the development of high-speed ADCs circuit for computing the RF sampling is an active area of research. However, instead of the circuit designing approach, we would like to propose the signal processing approach to reduce the power consumption and speed of an RF ADC.

To accomplish above, a learning-based *e*Sampling ADC can be used at the RF for the wireless communication receiver. Since the required information in the received signal is the type of modulating symbol, the idea is to *e*sample the RF signal at lower sampling rate to estimate the symbol instead of the complete

signal. This will allow to harvest the energy from the received signal, and also reduces the sampling rate. In this work, we would also use ViterbiNet algorithm proposed in [159], which is a data-driven symbol detector that does not require CSI. ViterbiNet is obtained by integrating deep neural networks (DNNs) into the Viterbi algorithm.

8.2.3 *e*TEM: Energy harvesting with Time encoding machine

The conventional approach in sampling theory is to describe a signal using pairs of time and amplitude. However, time encoding machine (TEM) allows us to represent the signal by the sequence of time only. The TEM has the ability to reduce power usage. Due to the decreasing size of integrated circuits and the attendant low-voltage, high-precision quantizers is difficult to implement. Time Encoding circuits provide an increment in timing resolution, which means that time encoding can help us develop human-made devices by developing sampling equipment with higher precision. This also has the ability to reduce power usage.

Consider a TEM as shown in Fig.8.1. The input analog signal, $x(t)$ is bandlimited and bounded as $|x(t)| \leq c < b$. Therefore, the positive signal $(x(t)+b)$ will pass to an RC circuit, i,e., integrator. The voltage across the capacitor C, i.e, $V_c(t)$ is compared with a pre-defined threshold, say, δ The overall process of TEM can be divided into two phases, the *Phase-1*, during which the capacitor, C will charge to δ, as shown in Fig. 8.1a) and the *Phase-2*, the comparator resets the voltage across the capacitor by connecting it to ground as shown in

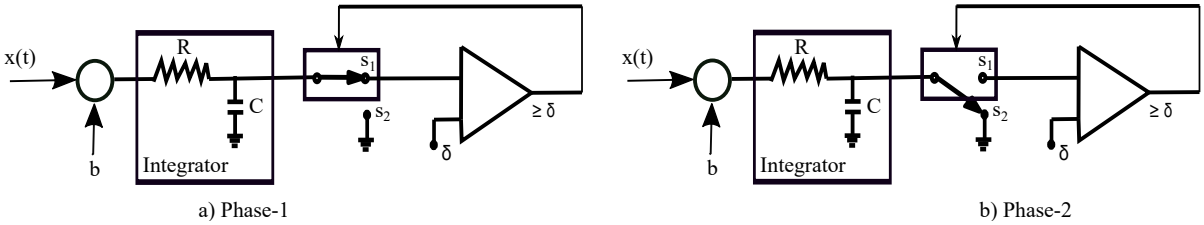

a) Phase-1 b) Phase-2

Figure 8.1: TEM

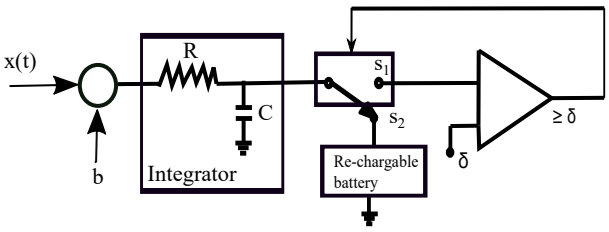

Figure 8.2: Modified Phase-2 for *e*TEM

Fig. 8.1b) for Δ amount of time, which is also known as refractory period. The output of TEM is sequence of strictly increasing time t_k, such that $V_c(t_k) = \delta$, where $k \in \mathbb{Z}$.

In future, we can develop an energy harvesting TEM, named as *e*TEM, which will harvest the un-utilized input signal energy in *Phase-2*, during the refractory period (Δ). In this period, the capacitor transfers the stored charge to the rechargeable battery as shown in Fig. 8.2.

References

[1] "Intel lab data," http://db.csail.mit.edu/labdata/labdata.html, 2004.

[2] M. R. Akdeniz, Y. Liu, M. K. Samimi, S. Sun, S. Rangan, T. S. Rappaport, and E. Erkip, "Millimeter wave channel modeling and cellular capacity evaluation," *IEEE Journal on Selected Areas in Communications*, vol. 32, no. 6, pp. 1164–1179, June 2014.

[3] I. A. Hemadeh, K. Satyanarayana, M. El-Hajjar, and L. Hanzo, "Millimeter-wave communications: physical channel models, design considerations, antenna constructions, and link-budget," *IEEE Communications Surveys & Tutorials*, vol. 20, no. 2, pp. 870–913.

[4] Q. Wu, G. Y. Li, W. Chen, D. W. K. Ng, and R. Schober, "An overview of sustainable green 5g networks," *IEEE Wireless Communications*, vol. 24, no. 4, pp. 72–80, 2017.

[5] M. Mishali and Y. C. Eldar, "Sub-nyquist sampling," *IEEE Signal Processing Magazine*, vol. 28, no. 6, pp. 98–124, 2011.

[6] Y. C. Eldar and G. Kutyniok, *Compressed sensing: theory and applications*. Cambridge university press, 2012.

[7] Y. C. Eldar, *Sampling theory: Beyond bandlimited systems*. Cambridge University Press, 2015.

[8] M. Mishali and Y. C. Eldar, "From theory to practice: Sub-nyquist sampling of sparse wideband analog signals," *IEEE Journal of Selected Topics in Signal Processing*, vol. 4, no. 2, pp. 375–391, 2010.

[9] J. A. Tropp, J. N. Laska, M. F. Duarte, J. K. Romberg, and R. G. Baraniuk, "Beyond nyquist: Efficient sampling of sparse bandlimited signals," *IEEE transactions on information theory*, vol. 56, no. 1, pp. 520–544, 2009.

[10] E. J. Candes and M. B. Wakin, "An introduction to compressive sampling," *IEEE Signal Processing Magazine*, vol. 25, no. 2, pp. 21–30, March 2008.

[11] S. Foucart and H. Rauhut, *A Mathematical Introduction to Compressive Sensing*. Birkhäuser Basel, 2013.

[12] J. Haupt, W. U. Bajwa, M. Rabbat, and R. Nowak, "Compressed sensing for networked data," *IEEE Signal Processing Magazine*, vol. 25, no. 2, pp. 92–101, March 2008.

[13] S. Li, D. Yang, G. Tang, and M. B. Wakin, "Atomic norm minimization for modal analysis from random and compressed samples," *IEEE Transactions on Signal Processing*, vol. 66, no. 7, pp. 1817–1831, 2018.

[14] W. Lu and N. Vaswani, "Regularized modified bpdn for noisy sparse reconstruction with partial erroneous support and signal value knowledge,"

IEEE Transactions on Signal Processing, vol. 60, no. 1, pp. 182–196, 2012.

[15] Y. Chen, Y. C. Eldar, and A. J. Goldsmith, "Shannon meets nyquist: Capacity of sampled gaussian channels," *IEEE Transactions on Information Theory*, vol. 59, no. 8, pp. 4889–4914, 2013.

[16] Y. Chen, A. J. Goldsmith, and Y. C. Eldar, "Channel capacity under sub-nyquist nonuniform sampling," *IEEE Transactions on Information Theory*, vol. 60, no. 8, pp. 4739–4756, 2014.

[17] Y. Chen, A. J. Goldsmith, and Y. C. Eldar, "On the minimax capacity loss under sub-nyquist universal sampling," *IEEE Transactions on Information Theory*, vol. 63, no. 6, pp. 3348–3367, 2017.

[18] A. Kipnis, A. J. Goldsmith, Y. C. Eldar, and T. Weissman, "Distortion rate function of sub-nyquist sampled gaussian sources," *IEEE Transactions on Information Theory*, vol. 62, no. 1, pp. 401–429, 2016.

[19] A. Kipnis, Y. C. Eldar, and A. J. Goldsmith, "Fundamental distortion limits of analog-to-digital compression," *IEEE Transactions on Information Theory*, vol. 64, no. 9, pp. 6013–6033, 2018.

[20] X. Li, J. Fang, H. Li, and P. Wang, "Millimeter wave channel estimation via exploiting joint sparse and low-rank structures," *IEEE Transactions on Wireless Communications*, vol. 17, no. 2, pp. 1123–1133, Feb 2018.

[21] E. Vlachos, G. C. Alexandropoulos, and J. Thompson, "Massive MIMO channel estimation for millimeter wave systems via matrix completion," *IEEE Signal Processing Letters*, vol. 25, no. 11, pp. 1675–1679, 2018.

[22] Z. He, T. Ogawa, and M. Haseyama, "The simplest measurement matrix for compressed sensing of natural images," in *2010 IEEE International Conference on Image Processing*, Sept 2010, pp. 4301–4304.

[23] N. Ansari and A. Gupta, "Image reconstruction using matched wavelet estimated from data sensed compressively using partial canonical identity matrix," *IEEE Transactions on Image Processing*, vol. 26, no. 8, pp. 3680–3695, Aug 2017.

[24] Y. Li and L. E. Parker, "A spatial-temporal imputation technique for classification with missing data in a wireless sensor network," in *2008 IEEE/RSJ International Conference on Intelligent Robots and Systems*, Sept 2008, pp. 3272–3279.

[25] L. Pan and J. Li, "K-nearest neighbor based missing data estimation algorithm in wireless sensor networks," *Wireless Sensor Network*, vol. 2, no. 02, p. 115, 2010.

[26] J.-F. Cai, E. J. Candès, and Z. Shen, "A singular value thresholding algorithm for matrix completion," *SIAM Journal on Optimization*, vol. 20, no. 4, pp. 1956–1982, 2010.

[27] Z. Li, Y. Zhu, H. Zhu, and M. Li, "Compressive sensing approach to urban traffic sensing," in *2011 31st International Conference on Distributed Computing Systems*, June 2011, pp. 889–898.

[28] L. Kong, M. Xia, X. Y. Liu, M. Y. Wu, and X. Liu, "Data loss and reconstruction in sensor networks," in *2013 Proceedings IEEE INFOCOM*, April 2013, pp. 1654–1662.

[29] T. S. Rappaport, J. N. Murdock, and F. Gutierrez, "State of the art in 60-ghz integrated circuits and systems for wireless communications," *Proceedings of the IEEE*, vol. 99, no. 8, pp. 1390–1436, 2011.

[30] S. Rangan, T. S. Rappaport, and E. Erkip, "Millimeter wave cellular wireless networks: Potentials and challenges," *arXiv preprint arXiv:1401.2560*, 2014.

[31] A. Alkhateeb, O. El Ayach, G. Leus, and R. W. Heath, "Channel estimation and hybrid precoding for millimeter wave cellular systems," *IEEE Journal of Selected Topics in Signal Processing*, vol. 8, no. 5, pp. 831–846, Oct 2014.

[32] D. Zhu, J. Choi, and R. W. Heath, "Auxiliary beam pair enabled aod and aoa estimation in closed-loop large-scale millimeter-wave mimo systems," *IEEE Transactions on Wireless Communications*, vol. 16, no. 7, pp. 4770–4785, July 2017.

[33] T. E. Bogale, L. B. Le, and X. Wang, "Hybrid analog-digital channel estimation and beamforming: Training-throughput tradeoff," *IEEE Transactions on Communications*, vol. 63, no. 12, pp. 5235–5249, Dec 2015.

[34] Z. Wen, W. Yin, and Y. Zhang, "Solving a low-rank factorization model for matrix completion by a nonlinear successive over-relaxation algorithm," *Mathematical Programming Computation*, vol. 4, no. 4, pp. 333–361, Dec 2012. [Online]. Available: https://doi.org/10.1007/s12532-012-0044-1

[35] M. J. Miller and N. H. Vaidya, "A mac protocol to reduce sensor network energy consumption using a wakeup radio," *IEEE Transactions on Mobile Computing*, vol. 4, no. 3, pp. 228–242, May 2005.

[36] S. Basagni, M. Y. Naderi, C. Petrioli, and D. Spenza, "Wireless sensor networks with energy harvesting," *Mobile Ad Hoc Networking: The Cutting Edge Directions*, pp. 701–736, 2013.

[37] S. Akbari, "Energy harvesting for wireless sensor networks review," in *2014 Federated Conference on Computer Science and Information Systems*, Sept 2014, pp. 987–992.

[38] V. W. Cheng and T. Y. Wang, "Performance analysis of distributed decision fusion using a censoring scheme in wireless sensor networks," *IEEE Transactions on Vehicular Technology*, vol. 59, no. 6, pp. 2845–2851, July 2010.

[39] I. F. Akyildiz, M. C. Vuran, and O. B. Akan, "On exploiting spatial and temporal correlation in wireless sensor networks," in *In Proceedings of WiOpt 2004: Modeling and Optimization in Mobile, Ad Hoc and Wireless Networks*, 2004, pp. 71–80.

[40] M. T. Nguyen, K. A. Teague, and N. Rahnavard, "Ccs: Energy-efficient data collection in clustered wireless sensor networks utilizing block-wise compressive sensing," *Computer Networks*, vol. 106, pp. 171–185, 2016.

[41] L. Xiang, J. Luo, and A. Vasilakos, "Compressed data aggregation for energy efficient wireless sensor networks," in *2011 8th Annual IEEE Communications Society Conference on Sensor, Mesh and Ad Hoc Communications and Networks*, June 2011, pp. 46–54.

[42] H. Zheng, F. Yang, X. Tian, X. Gan, X. Wang, and S. Xiao, "Data gathering with compressive sensing in wireless sensor networks: A random walk based approach," *IEEE Transactions on Parallel and Distributed Systems*, vol. 26, no. 1, pp. 35–44, Jan 2015.

[43] X. Y. Liu, Y. Zhu, L. Kong, C. Liu, Y. Gu, A. V. Vasilakos, and M. Y. Wu, "Cdc: Compressive data collection for wireless sensor networks," *IEEE Transactions on Parallel and Distributed Systems*, vol. 26, no. 8, pp. 2188–2197, Aug 2015.

[44] J. Wang, S. Tang, B. Yin, and X.-Y. Li, "Data gathering in wireless sensor networks through intelligent compressive sensing," in *2012 Proceedings IEEE INFOCOM*, March 2012, pp. 603–611.

[45] X. Wu, P. Yang, T. Jung, Y. Xiong, and X. Zheng, "Compressive sensing meets unreliable link: Sparsest random scheduling for compressive data gathering in lossy wsns," in *Proceedings of the 15th ACM international symposium on Mobile ad hoc networking and computing*. ACM, 2014, pp. 13–22.

[46] Y. Shen, W. Hu, R. Rana, and C. T. Chou, "Nonuniform compressive sensing for heterogeneous wireless sensor networks," *IEEE Sensors Journal*, vol. 13, no. 6, pp. 2120–2128, June 2013.

[47] G. Quer, R. Masiero, G. Pillonetto, M. Rossi, and M. Zorzi, "Sensing, compression, and recovery for wsns: Sparse signal modeling and monitoring framework," *IEEE Transactions on Wireless Communications*, vol. 11, no. 10, pp. 3447–3461, October 2012.

[48] S. Foucart and H. Rauhut, "An invitation to compressive sensing," in *A mathematical introduction to compressive sensing*. Springer, 2013, pp. 1–39.

[49] A. Gupta, S. Joshi, and P. Singh, "On the approximate discrete KLT of fractional brownian motion and its applications," *accepted to The Journal of Franklin Institute, Elsevier*, Aug 2018.

[50] A. Beck and M. Teboulle, "A fast iterative shrinkage-thresholding algorithm for linear inverse problems," *SIAM journal on imaging sciences*, vol. 2, no. 1, pp. 183–202, 2009.

[51] M. F. Duarte and R. G. Baraniuk, "Kronecker compressive sensing," *IEEE Transactions on Image Processing*, vol. 21, no. 2, pp. 494–504, 2012.

[52] W. Lu, T. Dai, and S.-T. Xia, "Binary matrices for compressed sensing," *IEEE Transactions on Signal Processing*, 2017.

[53] W. Wang, M. Garofalakis, and K. Ramchandran, "Distributed sparse random projections for refinable approximation," in *2007 6th International Symposium on Information Processing in Sensor Networks*, April 2007, pp. 331–339.

[54] Y. Li, C. Ai, W. P. Deshmukh, and Y. Wu, "Data estimation in sensor networks using physical and statistical methodologies," in *2008 The 28th International Conference on Distributed Computing Systems*, June 2008, pp. 538–545.

[55] T. Cover and P. Hart, "Nearest neighbor pattern classification," *IEEE transactions on information theory*, vol. 13, no. 1, pp. 21–27, 1967.

[56] L. Kong, D. Jiang, and M. Wu, "Optimizing the spatio-temporal distribution of cyber-physical systems for environment abstraction," in *2010 IEEE 30th International Conference on Distributed Computing Systems*, June 2010, pp. 179–188.

[57] V. P. Pauca, J. Piper, and R. J. Plemmons, "Nonnegative matrix factorization for spectral data analysis," *Linear algebra and its applications*, vol. 416, no. 1, pp. 29–47, 2006.

[58] E. J. Candès, X. Li, Y. Ma, and J. Wright, "Robust principal component analysis?" *J. ACM*, vol. 58, no. 3, pp. 11:1–11:37, Jun. 2011. [Online]. Available: http://doi.acm.org/10.1145/1970392.1970395

[59] X. Yi, D. Park, Y. Chen, and C. Caramanis, "Fast algorithms for robust pca via gradient descent," in *Advances in neural information processing systems*, 2016, pp. 4152–4160.

[60] Z. Lin, M. Chen, and Y. Ma, "The augmented lagrange multiplier method for exact recovery of corrupted low-rank matrices," *arXiv preprint arXiv:1009.5055*, 2010.

[61] I. Selesnick, "Sparse signal restoration," 10 2018.

[62] T. Oh, Y. Matsushita, Y. Tai, and I. S. Kweon, "Fast randomized singular value thresholding for low-rank optimization," *IEEE Transactions on Pattern Analysis and Machine Intelligence*, vol. 40, no. 2, pp. 376–391, Feb 2018.

[63] R. H. Keshavan, A. Montanari, and S. Oh, "Matrix completion from noisy entries," *Journal of Machine Learning Research*, vol. 11, no. Jul, pp. 2057–2078, 2010.

[64] "Data sensing lab," https://data-sensing-lab.appspot.com/, 2004.

[65] A. Gupta and R. K. Jha, "A survey of 5G network: Architecture and emerging technologies," *IEEE access*, vol. 3, pp. 1206–1232, 2015.

[66] R. Baldemair, E. Dahlman, G. Fodor, G. Mildh, S. Parkvall, Y. Selen, H. Tullberg, and K. Balachandran, "Evolving wireless communications: Addressing the challenges and expectations of the future," *IEEE Vehicular Technology Magazine*, vol. 8, no. 1, pp. 24–30, March 2013.

[67] J. G. Andrews, S. Buzzi, W. Choi, S. V. Hanly, A. Lozano, A. C. Soong, and J. C. Zhang, "What will 5G be?" *IEEE Journal on selected areas in communications*, vol. 32, no. 6, pp. 1065–1082, 2014.

[68] M. Agiwal, A. Roy, and N. Saxena, "Next generation 5G wireless networks: A comprehensive survey," *IEEE Communications Surveys & Tutorials*, vol. 18, no. 3, pp. 1617–1655, 2016.

[69] S. A. Busari, K. M. S. Huq, S. Mumtaz, L. Dai, and J. Rodriguez, "Millimeter-wave massive mimo communication for future wireless systems: A survey," *IEEE Communications Surveys Tutorials*, vol. 20, no. 2, pp. 836–869, Secondquarter 2018.

[70] J. Wang, Z. Lan, C.-W. Pyo, T. Baykas, C.-S. Sum, M. A. Rahman, R. Funada, F. Kojima, I. Lakkis, H. Harada *et al.*, "Beam codebook based beamforming protocol for multi-gbps millimeter-wave wpan systems," in *GLOBECOM 2009-2009 IEEE Global Telecommunications Conference*. IEEE, 2009, pp. 1–6.

[71] S. Hur, T. Kim, D. J. Love, J. V. Krogmeier, T. A. Thomas, and A. Ghosh, "Millimeter wave beamforming for wireless backhaul and access in small

cell networks," *IEEE Transactions on Communications*, vol. 61, no. 10, pp. 4391–4403, October 2013.

[72] A. F. Molisch, *Wireless communications*. John Wiley & Sons, 2012, vol. 34.

[73] A. Alkhateeb, G. Leus, and R. W. Heath, "Compressed sensing based multi-user millimeter wave systems: How many measurements are needed?" in *2015 IEEE International Conference on Acoustics, Speech and Signal Processing (ICASSP)*. IEEE, 2015, pp. 2909–2913.

[74] Z. Gao, L. Dai, Z. Wang, and S. Chen, "Spatially common sparsity based adaptive channel estimation and feedback for fdd massive mimo," *IEEE Transactions on Signal Processing*, vol. 63, no. 23, pp. 6169–6183, 2015.

[75] J. Lee, G. Gil, and Y. H. Lee, "Channel estimation via orthogonal matching pursuit for hybrid mimo systems in millimeter wave communications," *IEEE Transactions on Communications*, vol. 64, no. 6, pp. 2370–2386, June 2016.

[76] T. T. Cai and L. Wang, "Orthogonal matching pursuit for sparse signal recovery with noise." Institute of Electrical and Electronics Engineers, 2011.

[77] Z. Zhou, J. Fang, L. Yang, H. Li, Z. Chen, and R. S. Blum, "Low-rank tensor decomposition-aided channel estimation for millimeter wave mimo-ofdm systems," *IEEE Journal on Selected Areas in Communications*, vol. 35, no. 7, pp. 1524–1538, July 2017.

[78] Z. Zhou, J. Fang, L. Yang, H. Li, Z. Chen, and S. Li, "Channel estimation for millimeter-wave multiuser mimo systems via parafac decomposition," *IEEE Transactions on Wireless Communications*, vol. 15, no. 11, pp. 7501–7516, 2016.

[79] R. W. Heath, N. González-Prelcic, S. Rangan, W. Roh, and A. M. Sayeed, "An overview of signal processing techniques for millimeter wave mimo systems," *IEEE Journal of Selected Topics in Signal Processing*, vol. 10, no. 3, pp. 436–453, April 2016.

[80] R. Hu, J. Tong, J. Xi, Q. Guo, and Y. Yu, "Matrix completion-based channel estimation for mmwave communication systems with array-inherent impairments," *IEEE Access*, vol. 6, pp. 62 915–62 931, 2018.

[81] E. Vlachos, G. C. Alexandropoulos, and J. Thompson, "Wideband mimo channel estimation for hybrid beamforming millimeter wave systems via random spatial sampling," *IEEE Journal of Selected Topics in Signal Processing*, vol. 13, no. 5, pp. 1136–1150, 2019.

[82] I. Selesnick, "Sparse signal restoration," 10 2018.

[83] S. Boyd, N. Parikh, E. Chu, B. Peleato, J. Eckstein *et al.*, "Distributed optimization and statistical learning via the alternating direction method of multipliers," *Foundations and Trends® in Machine learning*, vol. 3, no. 1, pp. 1–122, 2011.

[84] J. G. Andrews, T. Bai, M. N. Kulkarni, A. Alkhateeb, A. K. Gupta, and R. W. Heath, "Modeling and analyzing millimeter wave cellular systems,"

IEEE Transactions on Communications, vol. 65, no. 1, pp. 403–430, Jan 2017.

[85] M. Polese and M. Zorzi, "Impact of channel models on the end-to-end performance of mmwave cellular networks," in *2018 IEEE 19th International Workshop on Signal Processing Advances in Wireless Communications (SPAWC)*. IEEE, 2018, pp. 1–5.

[86] T. S. Rappaport, S. Sun, R. Mayzus, H. Zhao, Y. Azar, K. Wang, G. N. Wong, J. K. Schulz, M. Samimi, and F. Gutierrez, "Millimeter wave mobile communications for 5G cellular: It will work!" *IEEE access*, vol. 1, pp. 335–349, 2013.

[87] Taesang Yoo and A. Goldsmith, "Capacity of fading mimo channels with channel estimation error," in *2004 IEEE International Conference on Communications (IEEE Cat. No.04CH37577)*, vol. 2, 2004, pp. 808–813 Vol.2.

[88] D. M. Tarique and M. T. Hasan, "Article: Impact of nakagami-m fading model on multi-hop mobile ad hoc network," *International Journal of Computer Applications*, vol. 26, no. 2, pp. 5–12, July 2011, full text available.

[89] N. Jain and V. A. Bohara, "Energy harvesting and spectrum sharing protocol for wireless sensor networks," *IEEE Wireless Communications Letters*, vol. 4, no. 6, pp. 697–700, 2015.

[90] J. Zhao, C. Qiao, R. S. Sudhaakar, and S. Yoon, "Improve efficiency and reliability in single-hop wsns with transmit-only nodes," *IEEE Transactions on Parallel and Distributed Systems*, vol. 24, no. 3, pp. 520–534, 2013.

[91] A. Al-Shaikhi and A. Masoud, "Efficient, single hop time synchronization protocol for randomly connected wsns," *IEEE Wireless Communications Letters*, vol. 6, no. 2, pp. 170–173, April 2017.

[92] Q. Wang, M. Hempstead, and W. Yang, "A realistic power consumption model for wireless sensor network devices," in *2006 3rd Annual IEEE Communications Society on Sensor and Ad Hoc Communications and Networks*, vol. 1, Sept 2006, pp. 286–295.

[93] H. Lee and C. G. Sodini, "Analog-to-digital converters: Digitizing the analog world," vol. 96, no. 2, pp. 323–334, Feb 2008.

[94] C. Shi, M. Ismail, and I. M. Mostafa, *Data converters for wireless standards*. Springer Science & Business Media, 2002, vol. 658.

[95] N. Jain, V. A. Bohara, and A. Gupta, "iDEG: Integrated data and energy gathering framework for practical wireless sensor networks using compressive sensing," vol. 19, no. 3, pp. 1040–1051, 2018.

[96] H. Tang, Z. C. Sun, K. W. R. Chew, and L. Siek, "A 1.33 μw 8.02-ENOB 100 kS/s successive approximation ADC with supply reduction technique for implantable retinal prosthesis," vol. 8, no. 6, pp. 844–856, Dec 2014.

[97] T. Michaeli and Y. C. Eldar, "Xampling at the rate of innovation," vol. 60, no. 3, pp. 1121–1133, 2011.

[98] D. Cohen, S. Tsiper, and Y. C. Eldar, "Analog-to-digital cognitive radio: Sampling, detection, and hardware," vol. 35, no. 1, pp. 137–166, 2018.

[99] D. Cohen and Y. C. Eldar, "Sub-Nyquist radar systems: temporal, spectral, and spatial compression," vol. 35, no. 6, pp. 35–58, 2018.

[100] N. Shlezinger, S. Salamatian, Y. C. Eldar, and M. Médard, "Joint sampling and recovery of correlated sources," in *Proc. IEEE ISIT*, 2019, pp. 385–389.

[101] N. Shlezinger, Y. C. Eldar, and M. R. Rodrigues, "Hardware-limited task-based quantization," vol. 67, no. 20, pp. 5223–5238, 2019.

[102] N. Shlezinger and Y. C. Eldar, "Deep task-based quantization," *arXiv preprint arXiv:1908.06845*, 2020.

[103] N. Shlezinger, R. J. G. van Sloun, I. A. M. Hujiben, G. Tsintsadze, and Y. C. Eldar, "Learning task-based analog-to-digital conversion for MIMO receivers," in *Proc. IEEE ICASSP*, 2020.

[104] N. Shlezinger and Y. C. Eldar, "Task-based quantization with application to MIMO receivers," *arXiv preprint arXiv:2002.04290*, 2020.

[105] R. Zhang and C. K. Ho, "Mimo broadcasting for simultaneous wireless information and power transfer," *IEEE Transactions on Wireless Communications*, vol. 12, no. 5, pp. 1989–2001, May 2013.

[106] X. Zhou, R. Zhang, and C. K. Ho, "Wireless information and power transfer: Architecture design and rate-energy tradeoff," in *Global Communications Conference (GLOBECOM), 2012 IEEE*, Dec 2012, pp. 3982–3987.

[107] L. Liu, R. Zhang, and K.-C. Chua, "Wireless information and power transfer: A dynamic power splitting approach," vol. 61, no. 9, pp. 3990–4001, 2013.

[108] X. Lu, P. Wang, D. Niyato, D. I. Kim, and Z. Han, "Wireless networks with RF energy harvesting: A contemporary survey," vol. 17, no. 2, pp. 757–789, 2014.

[109] N. S. Artan, X. Xu, W. Shi, and H. J. Chao, "Optimizing analog-to-digital converters for sampling extracellular potentials," in *Proc. IEEE EMBC*, 2012, pp. 1663–1666.

[110] S. Lee, A. P. Chandrakasan, and H. Lee, "A 1 GS/s 10b 18.9 mW time-interleaved SAR ADC with background timing skew calibration," vol. 49, no. 12, pp. 2846–2856, Dec 2014.

[111] Y. Zhou, B. Xu, and Y. Chiu, "A 12-b 1-GS/s 31.5-mW time-interleaved SAR ADC with analog HPF-assisted skew calibration and randomly sampling reference ADC," vol. 54, no. 8, pp. 2207–2218, Aug 2019.

[112] B. T. Reyes, L. Biolato, A. C. Galetto, L. Passetti, F. Solis, and M. R. Hueda, "An energy-efficient hierarchical architecture for time-interleaved SAR ADC," vol. 66, no. 6, pp. 2064–2076, June 2019.

[113] S. A. Zahrai, M. Zlochisti, N. Le Dortz, and M. Onabajo, "A low-power high-speed hybrid ADC with merged sample-and-hold and DAC functions for efficient subranging time-interleaved operation," vol. 25, no. 11, pp. 3193–3206, Nov 2017.

[114] B. Razavi, *Principles of data conversion system design*. Wiley, 1995.

[115] V. Hariprasath, J. Guerber, S.-H. Lee, and U.-K. Moon, "Merged capacitor switching based SAR ADC with highest switching energy-efficiency," *Electronics letters*, vol. 46, no. 9, pp. 620–621, 2010.

[116] C.-C. Liu, S.-J. Chang, G.-Y. Huang, and Y.-Z. Lin, "A 10-bit 50-MS/s SAR ADC with a monotonic capacitor switching procedure," vol. 45, no. 4, pp. 731–740, 2010.

[117] B. P. Ginsburg and A. P. Chandrakasan, "An energy-efficient charge recycling approach for a SAR converter with capacitive DAC," in *Proc. IEEE ISCAS*, May 2005, pp. 184–187.

[118] J. L. McCreary and P. R. Gray, "All-MOS charge redistribution analog-to-digital conversion techniques. I," vol. 10, no. 6, pp. 371–379, 1975.

[119] D. Zhang, C. Svensson, and A. Alvandpour, "Power consumption bounds for SAR ADCs," in *Proc. ECCTD*, Aug 2011, pp. 556–559.

[120] T. Soyata, L. Copeland, and W. Heinzelman, "RF energy harvesting for embedded systems: A survey of tradeoffs and methodology," vol. 16, no. 1, pp. 22–57, Firstquarter 2016.

[121] S. Zhao, H. Fu, K. Ma, and J. Ma, "A novel sensor for vibration frequency measurement with piezoelectric kinetic energy harvesting," *IEEE Sensors Journal*, vol. 18, no. 22, pp. 9286–9296, 2018.

[122] H. Cho, S. Jo, J. H. Yoon, T. Goh, B. G. Choi, and H. Yoo, "A batteryless chronic wound monitoring system with 13.56-MHz energy harvesting," *IEEE Sensors Journal*, vol. 19, no. 20, pp. 9431–9440, 2019.

[123] D. Alghisi, M. Ferrari, and V. Ferrari, "Battery-less non-contact temperature measurement system powered by energy harvesting from intentional human action," *IET Circuits, Devices Systems*, vol. 9, no. 2, pp. 96–104, 2015.

[124] M. Sarker, S. H. M. Ali, M. Othman, and S. Islam, "Designing a battery-less piezoelectric based energy harvesting interface circuit with 300 mV startup voltage," in *Journal of physics: conference series*, vol. 431, no. 1, 2013.

[125] T. Michaeli and Y. C. Eldar, "High-rate interpolation of random signals from nonideal samples," vol. 57, no. 3, pp. 977–992, 2008.

[126] A. Kipnis, Y. C. Eldar, and A. J. Goldsmith, "Fundamental distortion limits of analog-to-digital compression," vol. 64, no. 9, pp. 6013–6033, 2018.

[127] Y. Polyanskiy and Y. Wu, "Lecture notes on information theory," *Lecture Notes for ECE563 (UIUC)*, 2014.

[128] B. Razavi, "The bootstrapped switch [a circuit for all seasons]," *IEEE Solid-State Circuits Magazine*, vol. 7, no. 3, pp. 12–15, Summer 2015.

[129] M.-J. Chen, Y.-B. Gu, T. Wu, P.-C. Hsu, and T.-H. Liu, "Weak inversion charge injection in analog MOS switches," *IEEE journal of solid-state circuits*, vol. 30, no. 5, pp. 604–606, 1995.

[130] X. Yue, "Determining the reliable minimum unit capacitance for the DAC capacitor array of SAR ADCs," *Microelectronics Journal*, vol. 44, p. 473–478, 06 2013.

[131] L. Chen, J. Ma, and N. Sun, "Capacitor mismatch calibration for SAR ADCs based on comparator metastability detection," in *2014 IEEE International Symposium on Circuits and Systems (ISCAS)*. IEEE, 2014, pp. 2357–2360.

[132] P. Harpe, G. Dolmans, K. Philips, and H. de Groot, "A 0.7V 7-to-10bit 0-to-2MS/s flexible SAR ADC for ultra low-power wireless sensor nodes," in *2012 Proceedings of the ESSCIRC*, Sep. 2012, pp. 373–376.

[133] T. Sundstrom, B. Murmann, and C. Svensson, "Power dissipation bounds for high-speed Nyquist analog-to-digital converters," vol. 56, no. 3, pp. 509–518, March 2009.

[134] P. J. A. Harpe, C. Zhou, Y. Bi, N. P. van der Meijs, X. Wang, K. Philips, G. Dolmans, and H. de Groot, "A 26μw 8 bit 10 MS/s asynchronous SAR ADC for low energy radios," *IEEE Journal of Solid-State Circuits*, vol. 46, no. 7, pp. 1585–1595, July 2011.

[135] J. Craninckx and G. V. der Plas, "A 65fJ/conversion-step 0-to-50MS/s 0-to-0.7mW 9b charge-sharing SAR ADC in 90nm digital CMOS," in *Proc. IEEE ISSCC*, 2007, pp. 246–600.

[136] D. Kwon and G. A. Rincon-Mora, "A rectifier-free piezoelectric energy harvester circuit," in *2009 IEEE International Symposium on Circuits and Systems*, 2009, pp. 1085–1088.

[137] Y. K. Ramadass and A. P. Chandrakasan, "A battery-less thermoelectric energy harvesting interface circuit with 35 mv startup voltage," *IEEE Journal of Solid-State Circuits*, vol. 46, no. 1, pp. 333–341, 2011.

[138] M. Alhawari, B. Mohammad, H. Saleh, and M. Ismail, "An efficient polarity detection technique for thermoelectric harvester in l-based converters," *IEEE Transactions on Circuits and Systems I: Regular Papers*, vol. 64, no. 3, pp. 705–716, 2017.

[139] W. Kester and A. D. I. Engineeri, *Data conversion handbook*. Newnes, 2005.

[140] B. Haug, "Wireless sensor nodes can be powered by temperature gradients; no batteries needed: Harvesting energy from thermoelectric generators," *Ieee power electronics magazine*, vol. 4, no. 4, pp. 24–32, 2017.

[141] C. E. Shannon, "Communication in the presence of noise," *Proceedings of the IRE*, vol. 37, no. 1, pp. 10–21, 1949.

[142] J. Mo, A. Alkhateeb, S. Abu-Surra, and R. W. Heath, "Hybrid architectures with few-bit ADC receivers: Achievable rates and energy-rate tradeoffs," vol. 16, no. 4, pp. 2274–2287, April 2017.

[143] S. Rini, L. Barletta, Y. C. Eldar, and E. Erkip, "A general framework for mimo receivers with low-resolution quantization," in *2017 IEEE Information Theory Workshop (ITW)*. IEEE, 2017, pp. 599–603.

[144] M. S. Stein, S. Bar, J. A. Nossek, and J. Tabrikian, "Performance analysis for channel estimation with 1-bit adc and unknown quantization threshold," *IEEE Transactions on Signal Processing*, vol. 66, no. 10, pp. 2557–2571, 2018.

[145] J. Zhang, L. Dai, Z. He, S. Jin, and X. Li, "Performance analysis of mixed-adc massive mimo systems over rician fading channels," *IEEE Journal on Selected Areas in Communications*, vol. 35, no. 6, pp. 1327–1338, 2017.

[146] Y. Chi and H. Fu, "Subspace learning from bits," *IEEE Transactions on Signal Processing*, vol. 65, no. 17, pp. 4429–4442, 2017.

[147] R. M. Corey and A. C. Singer, "Wideband source localization using one-bit quantized arrays," in *2017 IEEE 7th International Workshop on Computational Advances in Multi-Sensor Adaptive Processing (CAMSAP)*. IEEE, 2017, pp. 1–5.

[148] K. Yu, Y. D. Zhang, M. Bao, Y.-H. Hu, and Z. Wang, "Doa estimation from one-bit compressed array data via joint sparse representation," *IEEE Signal Processing Letters*, vol. 23, no. 9, pp. 1279–1283, 2016.

[149] C.-L. Liu and P. Vaidyanathan, "One-bit sparse array doa estimation," in *2017 IEEE International Conference on Acoustics, Speech and Signal Processing (ICASSP)*. IEEE, 2017, pp. 3126–3130.

[150] N. Jain, V. A. Bohara, and A. Gupta, "PCI-MF: Partial canonical identity and matrix factorization framework for channel estimation in mmwave massive mimo systems," *IEEE Open Journal of Signal Processing*, 2020.

[151] A. Ahmed and J. K. Romberg, "Compressive sampling of ensembles of correlated signals," *CoRR*, vol. abs/1501.06654, 2015. [Online]. Available: http://arxiv.org/abs/1501.06654

[152] R. M. Mersereau and A. V. Oppenheim, "Digital reconstruction of multidimensional signals from their projections," *Proceedings of the IEEE*, vol. 62, no. 10, pp. 1319–1338, 1974.

[153] M. B. Matthews, "On the linear minimum-mean-squared-error estimation of an undersampled wide-sense stationary random process," *IEEE Transactions on Signal Processing*, vol. 48, no. 1, pp. 272–275, 2000.

[154] A. Ahmed, "Compressive acquisition and least-squares reconstruction of correlated signals," *IEEE Signal Processing Letters*, vol. 24, no. 7, pp. 933–937, 2017.

[155] N. Jain, N. Shlezinger, B. Tiwari, Y. C. Eldar, A. Gupta, V. A. Bohara, and P. G. Bahubalindruni, "esampling: Energy harvesting adcs," *arXiv preprint arXiv:2007.08275*, 2020.

[156] D. Seidner and M. Feder, "Vector sampling expansion," *IEEE Transactions on Signal Processing*, vol. 48, no. 5, pp. 1401–1416, 2000.

[157] A. Kipnis, A. J. Goldsmith, and Y. C. Eldar, "The distortion rate function of cyclostationary gaussian processes," *IEEE Transactions on Information Theory*, vol. 64, no. 5, pp. 3810–3824, 2018.

[158] J. B. Lasserre, "A trace inequality for matrix product," *IEEE Transactions on Automatic Control*, vol. 40, no. 8, pp. 1500–1501, 1995.

[159] N. Shlezinger, N. Farsad, Y. C. Eldar, and A. J. Goldsmith, "Viterbinet: A deep learning based viterbi algorithm for symbol detection," *CoRR*, vol. abs/1905.10750, 2019. [Online]. Available: http://arxiv.org/abs/1905.10750